Exciton-phonon coupling and phonon-assisted luminescence in hexagonal Boron Nitride nanostructures

Pierre Lechifflart

To cite this version:

Pierre Lechifflart. Exciton-phonon coupling and phonon-assisted luminescence in hexagonal Boron Nitride nanostructures. Physics [physics]. Aix Marseille Université, 2023. English. NNT : 2023AIXM0350 . tel-04266805

HAL Id: tel-04266805

https://hal.science/tel-04266805

Submitted on 31 Oct 2023

Aix-Marseille université
Socialement engagée

NNT/NL : 2020AIXM0001/001ED000

THÈSE DE DOCTORAT

Soutenue à Aix-Marseille Université
le 27 Octobre 2023

Pierre LECHIFFLART

Exciton-phonon coupling and phonon-assisted luminescence in hexagonal Boron Nitride nanostructures

Discipline
Physique et Sciences de la Matière

Spécialité
Matière Condensée et Nanosciences

École doctorale
352 PHYSIQUE ET SCIENCES DE LA MATIERE

Laboratoire/Partenaires de recherche
CINaM - Centre Interdisciplinaire de Nanosciences de Marseille / UMR 7325

Composition du jury

Olivia PULCI Université de Rome Tor Vergata	Rapporteuse
Sylvain LATIL CEA Saclay	Rapporteur
Valerio OLEVANO Institut Néel, Grenoble	Examinateur
Aurélien MANCHON Aix-Marseille Université, CINaM	Président du jury
Claudio ATTACCALITE CNRS-CINaM, Marseille	Directeur de thèse

CINaM

Affidavit

I, undersigned, Pierre Lechifflart, hereby declare that the work presented in this manuscript is my own work, carried out under the scientific direction of Dr. Claudio Attaccalite, in accordance with the principles of honesty, integrity and responsibility inherent to the research mission. The research work and the writing of this manuscript have been carried out in compliance with both the french national charter for Research Integrity and the Aix-Marseille University charter on the fight against plagiarism.

This work has not been submitted previously either in this country or in another country in the same or in a similar version to any other examination body.

Marseille, 28 August 2023

Pierre Lechifflart

Liste de publications et participation aux conférences

Liste des publications réalisées dans le cadre du projet de thèse :

1. Pierre Lechifflart, Fulvio Paleari and Claudio Attaccalite. “Excitons under strain : light absorption and emission in strained hexagonal boron nitride”. In : SciPost Physics 12 (May 2022), p. 145.
2. Pierre Lechifflart, Fulvio Paleari, Davide Sangalli and Claudio Attaccalite. “First-principles study of luminescence in hexagonal boron nitride single layer : Exciton-phonon coupling and the role of substrate”. In : Physical Review Materials 7.2 (Feb. 2023).
3. Michele Re Fiorentin, Pierre Lechifflart and Fulvio Paleari, "Electronic structure and luminescence of Bernal Boron Nitride", *en péparation*.

Participation aux conférences et écoles d’été au cours de la période de thèse :

1. Virtual school on electronic excitations in solids and nanostructures using the Yambo code, Avril 2021, en ligne
2. 17th ETSF Young Researchers Meeting, Septembre 2021, Cagliari
3. 12th Meeting on NanoScience Advances, Septembre 2021, Porquerolles
4. School : ab initio Many-body methods and simulations with the yambo code, Avril 2022, Trieste
5. 25th ETSF Workshop, Juin 2022, Leuven
6. 18th ETSF Young Researchers Meeting, Septembre 2022, Marseille
7. Green’s function methods : the next generation Workshop, Novembre 2022, Toulouse
8. GDR HOWDI annual meeting, Mai 2023, Porquerolles
9. International BN Workshop, Mai 2023, Montpellier

Résumé

La présente thèse de doctorat explore l'interaction complexe entre les excitons et les phonons dans les nanostructures de nitrure de bore hexagonal (hBN) à l'aide de méthodes de calcul avancées. La thèse commence par une introduction au hBN, mettant en lumière ses propriétés uniques et son importance dans la physique de la matière condensée.

Le chapitre 2 donne un aperçu complet du cadre théorique de pointe utilisé tout au long de la recherche, englobant la théorie de la fonctionnelle de la densité (DFT), la théorie des perturbations de la fonctionnelle de la densité (DFPT) pour les propriétés des phonons, et la théorie des perturbations à N-corps (MBPT) à travers l'approximation GW et l'équation de Bethe-Salpeter pour prendre en compte les effets collectifs électroniques et excitoniques.

Dans le chapitre 3, l'accent est mis sur le hBN massif soumis à une déformation uniaxiale, où le couplage exciton-phonon est étudié à l'aide d'une méthode de dérivation par différences finies. Cette approche reproduit approximativement les changements d'intensité de la luminescence observés lorsqu'une contrainte est appliquée au cristal. Les résultats de ce chapitre donnent des indications précieuses sur les propriétés électroniques, phononiques et excitoniques, ainsi que sur les interactions exciton-phonon dans les systèmes hBN massifs soumis à une déformation uniaxiale.

Le chapitre 4 se penche sur l'étude du hBN monocouche, en utilisant une méthode ab initio fondée sur une dérivation théorique rigoureuse des éléments de matrice du couplage exciton-phonon. En incorporant les pics directs et indirects dans les spectres de luminescence, cette méthode donne des intensités relatives détaillées, permettant une interprétation précise des mesures expérimentales publiées par différents groupes de recherche. Notamment, cette étude élimine la possibilité d'observer des répliques de phonons dans les spectres du hBN monocouche, apportant une nouvelle clarté à des interprétations auparavant ambiguës.

En outre, la thèse présente des résultats préliminaires pour le BN Bernal, un polytype de hBN avec un empilement de couches différent, présentant des gaps d'énergie directs et indirects très proches les uns des autres. Ce matériau intrigant a le potentiel d'afficher simultanément des pics directs et indirects dans les spectres de luminescence. Dans le cadre des recherches en cours qui incluent une étude numérique poussée, ce chapitre ouvre la voie à une compréhension plus approfondie des interactions exciton-phonon dans la phase Bernal du BN.

Dans l'ensemble, cette thèse de doctorat contribue de manière significative au domaine de la physique computationnelle de la matière condensée en clarifiant les phénomènes complexes de couplage exciton-phonon dans diverses nanostructures hBN. Les connaissances acquises grâce à cette étude peuvent faire progresser la compréhension et la conception de nouveaux dispositifs optoélectroniques basés sur des matériaux hBN.

Mots-clés : luminescence, phonons, excitons, couplage exciton-phonon

Abstract

The present PhD thesis explores the intricate interplay between excitons and phonons in hexagonal Boron Nitride (hBN) nanostructures through advanced computational methods. The thesis commences with an introduction to hBN, shedding light on its unique properties and relevance in condensed matter physics.

Chapter 2 provides a comprehensive overview of the state-of-the-art theoretical framework employed throughout the research, encompassing Density Functional Theory (DFT), Density Functional Perturbation Theory (DFPT) for phonon properties, and Many-Body Perturbation Theory (MBPT) through the GW approximation and the Bethe-Salpeter equation to account for collective electronic and excitonic effects.

In Chapter 3, the focus lies on uniaxially strained bulk hBN, where the exciton-phonon coupling is studied using a finite-difference derivative method. This approach approximately reproduces the changes in luminescence intensity observed when strain is applied to the crystal. The outcomes of this chapter offer valuable insights into the electronic, phononic and excitonic properties, as well as exciton-phonon interactions in bulk hBN systems under uniaxial strain.

Chapter 4 delves into the investigation of monolayer hBN, employing an ab initio method grounded on a rigorous theoretical derivation of the exciton-phonon coupling matrix elements. By incorporating both direct and indirect peaks in the luminescence spectra, this method yields detailed relative intensities, enabling an accurate interpretation of experimental measurements published by different research groups. Notably, this study eliminates the possibility of observing phonon replicas in the spectra of monolayer hBN, providing new clarity to previously ambiguous interpretations.

Furthermore, the thesis offers preliminary results for Bernal BN, a polytype of hBN with a different layer stacking, featuring closely situated direct and indirect energy gaps. This intriguing material holds potential for displaying simultaneously both direct and indirect peaks in luminescence spectra. As part of ongoing research that includes deep numerical studies, this chapter paves the way for a deeper understanding of exciton-phonon interactions in Bernal BN structures.

Overall, this PhD thesis contributes significantly to the field of computational condensed matter physics by unraveling the complex exciton-phonon coupling phenomena in various hBN nanostructures. The insights gained from this study have the potential to advance the understanding and design of novel optoelectronic devices based on hBN materials.

Keywords: luminescence, excitons, phonons, exciton-phonon coupling

Résumé étendu

Le matériau central de cette thèse est le nitrure de bore hexagonal. Depuis sa première synthèse en 1842 par William H. Balmain, le nitrure de bore existe sous différentes formes, cristallines ou amorphes. Il est utilisé dans l'industrie comme lubrifiant, ou bien dans des composants soumis à de fortes températures, du fait de sa grande stabilité thermique et chimique.

Sa forme hexagonale (hBN) attire beaucoup l'attention des chercheurs en physique de la matière condensée depuis les vingt dernières années, depuis la synthèse de cristaux à haute pureté par Taniguchi et Watanabe en 2004. Cette forme a un réseau cristallin hexagonal, constitué de feuillets empilés les uns sur les autres, ou les atomes de bore et d'azote sont alternés aux sommets des hexagones et sont liés par des liaisons hybrides sp^2. Ce cristal est très similaire au graphite. Le polytype le plus stable a un empilement dit AA', c'est-à-dire qu'un atome de bore est superposé à un atome d'azote du feuillet du dessous. C'est principalement ce polytype qui sera étudié dans cette thèse notamment dans le Chapitre 3. Il existe d'autres polytypes en fonction de l'empilement. Nous pouvons mentionner la forme dite Bernal (bBN) qui a un empilement AB, c'est-à-dire qu'un atome de bore est au-dessus du centre d'un hexagone du feuillet inférieur. Ce polytype sera étudié à la fin du Chapitre 4. Les polytypes hBN et bBN sont des isolants avec des gaps d'énergie indirects autour de 6 eV. Cependant, la première caractérisation optique du hBN à haute pureté par Taniguchi et Watanabe a révélé que l'intensité de luminescence du hBN est bien plus haute que d'autres matériaux à gaps indirects comme le diamant, et comparable à celle de matériaux à gaps directs comme l'oxide de zinc. Ceci a conduit à un débat dans la communauté scientifique sur la nature directe ou indirecte du hBN massif. Aujourd'hui grâce à l'évolution technologique des appareils de mesure et grâce à des simulations *ab initio*, il est acquis que ce matériau possède un gap indirect. Sa forte luminescence est due à un fort couplage entre les excitons et les vibrations du réseau cristallin, ce qui permet aux excitons noirs de se recombiner de façon radiative, en amplifiant l'intensité de luminescence.

Tout comme le graphite, il est possible d'exfolier mécaniquement un ou plusieurs feuillets afin d'obtenir un crystal d'une épaisseur finie, allant jusqu'à une couche mono-atomique. La monocouche de nitrure de bore hexagonal (mBN) a un paramètre de maille extrêmement proche de celui du graphène, qui fait l'objet d'énormément de recherches dues à ses propriétés remarquables. Il est ainsi un candidat de choix comme substrat ou matériau d'encapsulation sans contrainte pour le graphène, qui joue en plus le rôle de barrière de passivation. Il a été montré qu'il pouvait décupler la mobilité des électrons dans le graphène. Du fait de son caractère isolant ainsi que sa transparence dans le domaine visible, le mBN peut également améliorer les propriétés optiques des dichalcogénures de métaux de transitions, sans altérer leurs propriétés électroniques, ou bien agir comme isolant diélectriques entre deux matériaux pour contrôler leur couplage électrique. En combinant différents matériaux en deux dimensions, avec ou sans contrainte, avec ou sans rotation entre les feuillets, les possibilités d'hétérostructures sont infinies et les propriétés optiques et électroniques peuvent être ajustées presque à volonté. Pour toutes ces raisons, le mBN est un matériau de choix dans l'élaboration de composants opto-électroniques.

Pour mesurer les propriétés optiques d'un feuillet monoatomique, il faut descendre à température cryogénique et avoir des appareils avec des résolutions très fines. C'est pourquoi les mesures précises de luminescence de mBN sont apparues dans la littérature scientifique seulement récemment. De plus, ces mesures contiennent des structures différentes d'un spectre à l'autre et leurs interprétations ne sont pas unanimes.

Après cette introduction générale, le Chapitre 2 contient la présentation du socle théorique nécessaire à nos calculs, qui commence par l'explication du problème à N-corps, essentiel dans tous les domaines de la physique de la matière condensée. D'un point de vue théorique, l'Hamiltonien qui décrit le système d'électrons et d'ions qui constitue les solides ou les molécules peut s'écrire en une somme de six termes. Ce qui peut sembler assez simple est pourtant insolvable dès que le nombre d'électrons et d'ions considérés dépasse une dizaine. En effet, bien que certains termes ne posent pas de problème particulier à calculer comme les énergies cinétiques totales des électrons ou des ions, les autres termes peuvent être immensément plus compliqués, comme l'interaction électron-électron, qui est une interaction à deux corps. La complexité de ce terme fait que l'on doit recourir à des simplifications et des approximations pour réussir à calculer les propriétés des solides qui nous intéressent. Bien qu'il soit possible de recourir à des modèles et de décrire certaines propriétés par des paramètres, l'approche choisie dans cette thèse est dite *ab initio*, c'est-à-dire que les seules données initiales sont les numéros atomiques des atomes composant le crystal ainsi que leurs positions. Dans cette approche, il faut s'assurer que les approximations faites ne soient pas trop restrictives et que toute la physique des phénomènes que nous tentons de reproduire soit incluse. Cela peut mener à une complexité à la fois dans la formulation théorique, mais aussi dans l'implémentation numérique dans les codes de simulation. En général, les temps de calculs *ab initio* sont plus longs que ceux des modèles. Toutefois du point de vue de l'utilisateur des codes de simulation, la tâche est simplifiée car il suffit seulement de préciser en entrée le type de cristal à étudier et de lire les sorties produites par les codes.

La première approximation est celle de Born-Oppenheimer, qui consiste à découpler le mouvement des ions et celui des électrons. On considère que les électrons sont toujours dans l'état fondamental lorsqu'on calcule le mouvement des ions, et les positions ioniques sont un paramètre dans l'Hamiltonien des électrons.

La première théorie décrite ici est celle de la fonctionnelle de la densité (DFT), élaborée dans les années 1960 par Hohenberg, Kohn et Sham. Celle ci a pour but de calculer la densité électronique dans l'état fondamental du système. On peut montrer que l'énergie totale du système dépend de la densité électronique. L'idée pour calculer la densité est de construire un système auxiliaire qui aurait la même densité dans l'état fondamental que le système réel qui nous intéresse, mais dont les électrons sont indépendants les uns des autres. Leur interaction est remplacée par un champ moyen qui contient les effets électrostatiques classiques ainsi que les effets quantiques d'échange et de corrélation. Ce champ moyen est le potentiel de Kohn-Sham. Il est présent dans une équation de Schrödinger, appelée l'équation de Kohn-Sham, pour chaque particule indépendante du système auxiliaire. Cependant l'expression analytique de ce potentiel dépend de la densité électronique, comme montré par Kohn et Sham. A son tour, la densité peut être calculée en sommant les modules carrés des fonctions d'ondes solutions des équations de Kohn-Sham. Nous voyons ici que pour obtenir la densité électronique, il faut résoudre les équations de Kohn-Sham de façon autocohérente, en partant d'une densité hypothétique et en convergeant à chaque itération vers la bonne densité. Une fois que la densité ne varie pas plus qu'un seuil arbitraire à chaque itération, le calcul s'arrête et nous pouvons obtenir l'énergie totale de l'état fondamental du système.

Cette théorie est en principe exacte, mais le potentiel d'échange-correlation n'a pas d'expression analytique et est impossible à calculer avec précision. Pour cette raison, il faut l'approximer afin de rendre sa dépendance en la densité calculable. Différentes approximations existent telles que l'approximation de la densité locale (LDA) ou l'approximation du gradient généralisé (GGA). Chaque approximation a ses avantages et ses inconvénients, et se rapprochent toutes plus ou moins du vrai potentiel d'échange-corrélation. De plus le potentiel ionique dans lequel évoluent les particules indépendantes, qui contient une divergence autour de la position des ions, est lui aussi approximé par des pseudopotentiels pour supprimer cette divergence et accélérer les calculs. Ces potentiels approximés sont appelés pseudopotentiels.

Afin de pouvoir diagonaliser l'Hamiltonien et résoudre les équation de Kohn-Sham, il faut choisir une base dans laquelle exprimer les fonctions d'ondes. La base que nous utilisons dans cette thèse est la base des ondes planes. Celle-ci a la particularité de bien s'accorder avec le théorème de Bloch qui décrit les électrons dans des cristaux périodiques. Ici les électrons de Bloch sont décrits par une combinaison linéaire d'ondes planes, et possèdent donc un moment et un vecteur d'onde.

Il faut toutefois insister sur le fait que les valeurs propres des équations de Kohn-Sham ne sont pas les états d'énergie des vrais électrons du système. Ce sont les niveaux d'énergie du système auxiliaire, qui n'ont pas de réelle signification physique. Toutefois, si les approximations sont suffisamment précises et que le calcul de densité est suffisamment convergé, les valeurs propres de Kohn-Sham peuvent donner un bonne approximation des niveaux d'énergies du vrai système, mais seulement pour les plus hauts états de valence. Le gap des semi-conducteurs et des isolants n'est jamais précis en DFT et il faut recourir à des théories plus précises pour décrire le gap et les états d'énergies excités du système.

Ceci est réalisé grâce à la théorie des perturbations à N-corps (MBPT). Cette théorie est basée sur la fonction de Green du système à N électrons. Cet object mathématique a le sens physique du propagateur à N particules, c'est à dire la probabilité qu'un électron introduit à l'instant t_1, à la position r_1 et avec le spin σ_1 se propage jusqu'à la position r_2 et avec le spin σ_2 au temps t_2. Dans cette thèse, la dépendance en spin n'est pas considérée donc elle est toujours implicite. Mathématiquement, la fonction de Green est la solution d'une équation différentielle dont le terme de source est un delta de Dirac. Dans notre cas, c'est la solution de l'équation de Schrödinger contenant l'Hamiltonien électronique. La fonction de Green complète du système est une matrice multidimensionnelle, dont les deux premiers éléments de matrice sont la fonction de Green à une particule et la fonction de Green à deux particules. Beaucoup de quantités physiques intéressantes peuvent être extraites de ces fonctions, comme par exemple l'énergie totale du système d'électron corrélés. Plus intéressant dans notre cas, les pôles de la fonction de Green à une particule donnent les énergies d'excitation du système à N électron interagissant. On peut faire l'analogie entre les pôles de la fonction de Green à une particule et les spectres de photoémission ou de photoémission inversée. En effet, ces mesures consistent à mesurer l'énergie cinétique d'un électron arraché ou ajouté au système à N électrons, afin de déterminer les niveaux d'énergie existants. De façon équivalente, les pôles de la fonction de Green à N-1 électrons donnent les niveaux de valence du système, et ceux de la fonction de Green à N+1 électrons donnent les niveaux de conduction.

La fonction de Green à une ou deux particules est calculée en prenant en compte l'interaction avec tous les électrons. Les dérivations sont esquissées dans la partie 2.3 de la thèse. L'idée est d'ajouter une perturbation au système et de calculer les variations des différents potentiels grâce à la dérivée fonctionnelle par rapport à la perturbation. De cette façon et si l'on définit des nouvelles quantités physiques telles que la polarisabilité, la matrice diélectrique, la self-énergie ou encore l'interaction écrantée, on peut obtenir un système d'équations intégro-différentielles qui relient toutes ces quantités. Ce sont les équations d'Hedin, qui sont en principe exactes mais impossible à résoudre de façon analytique pour des systèmes réels. Pour simplifier la résolution, une des approximations les plus répandues consiste à négliger l'interaction électron-trou dans le vertex. De cette façon, la self-énergie se réduit au produit matriciel de la fonction de Green électronique G et de l'interaction écrantée W, ce qui donne le nom d'approximation GW. Avec cette approximation, les équations d'Hedin peuvent être reformulées en terme de *quasiparticules*, c'est-à-dire que les électrons ne sont plus considérés indépendants mais "habillés" par l'interaction avec les autres. Les énergies de ces quasiparticules sont données par les pôles de la fonction de Green électronique. Cela permet d'obtenir la structure de bandes électronique du système en meilleur accord avec l'expérience par rapport à la DFT. Un lien peut également être établi entre les pôles de la fonction de Green et les énergies d'ionisation et l'affinité électronique du système. Ainsi on peut simuler les expériences consistant à ajouter ou à arracher un électron du système. Ces variations de charge sont appelées excitations neutres, qui sont ainsi bien décrites par l'approximation GW.

En revanche, les excitations neutres, c'est-à-dire qu'un électron du système est promu à une bande de conduction mais ne quitte pas le cristal, nécessitent de considérer l'interaction électron-trou, négligée plus haut. A cette fin, nous considérons une équation de Dyson pour la fonction de Green à deux particules. Elle est appelée l'équation de Bethe-Salpeter (BSE) et décrit la propagation de paires électron-trou liés par l'interaction de Coulomb. Une telle paire liée est un nouveau type de quasiparticule appelée *exciton*. Moyennant quelques approximations décrites dans le Chapitre 2, la BSE peut être reformulée en un Hamiltonien à deux particules écrit dans la base des excitons. Ses valeurs propres sont les énergies des excitons et les coefficients du changement de base sont les vecteurs propres des excitons.

La description des excitons est essentielle afin de reproduire correctement les spectres optiques obtenus expérimentalement. Il est possible d'écrire les fonctions de réponse du système dans la base des excitons, ainsi que la fonction diélectrique microscopique. Ensuite, on peut obtenir la partie imaginaire de la fonction diélectrique macroscopique, qui est directement proportionnelle à l'observable mesuré dans les mesures d'absorption optique. L'inclusion des effets excitoniques permet de simuler des spectres très ressemblants avec l'expérience.

Pour simuler des spectres de luminescence en revanche, une formulation *ab initio* nécessiterait la description de phénomènes hors équilibre concernant l'interaction d'excitons, phonons et photons. Bien que certaines approchent aillent dans ce sens, cela est hors de la portée de cette thèse. En revanche, nous supposons que les systèmes que nous simulons sont dans une situation de quasi-équilibre, et que l'absorption et l'émission de lumière sont en équilibre dans un régime permanent. Cette approximation nous permet d'utiliser la relation de van Roosbroeck–Shockley qui permet de calculer le taux d'émission spontanée à partir du taux d'absorption. Le seul inconvénient est qu'il faut introduire un paramètre pour décrire le quasi-équilibre et le fait que les particules excitées ne sont pas décrite par la même température que le réseau. Dans cette thèse nous avons fait le choix de la fonction de Boltzmann qui donne de bons résultats pour une faible densité d'excitons. Il nous a donc fallu introduire une température excitonique que nous avons fitté sur des mesures expérimentales. C'est le seul paramètre parmi tous nos calculs *ab initio*.

Nous présentons ensuite comment décrire les vibrations du réseau cristallin. Nous considérons que les atomes vibrent autour de leur position d'équilibre comme des oscillateurs harmoniques quantiques. Un quantum de vibration est appelé un *phonon*, c'est une excitation collective avec une fréquence et un vecteur d'onde donnés. Nous présentons dans la section 2.5 une théorie basée sur un perturbation de la DFT, appelée théorie de la perturbation de la fonctionnelle de la densité (DFPT). Elle permet de calculer les fréquences et vecteurs propres de phonons dans une cellule unité. Les fréquences dépendent des vecteurs d'onde ou de façon équivalente du moment, et on peut obtenir les courbes de dispersion de chaque mode de phonon.

Ensuite, le problème des vibrations des atomes et le problème électronique sont regroupés de nouveau pour obtenir le couplage électron-phonon. Nous pouvons le formuler en seconde quantification. Ce sera un élément clé dans la construction du couplage exciton-phonon étudié dans cette thèse.

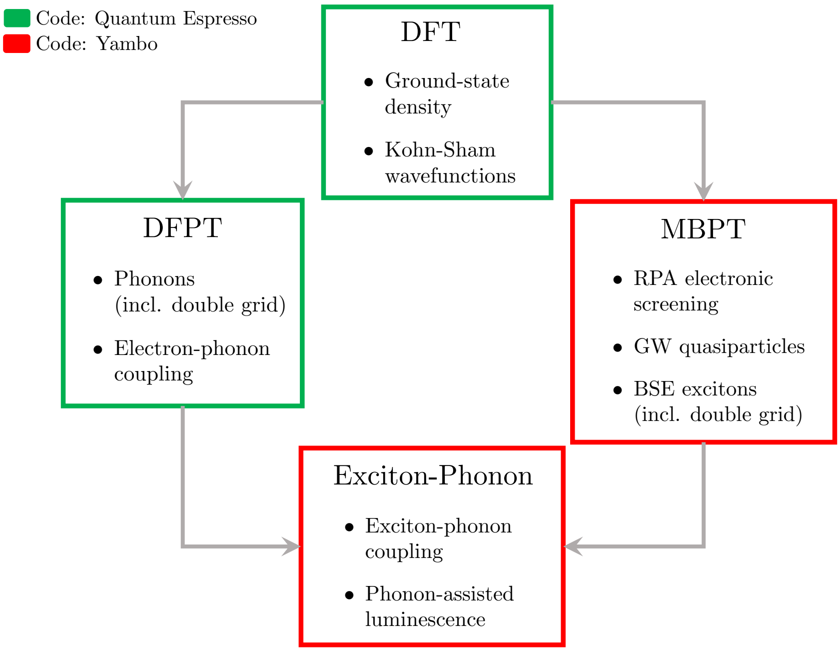

FIGURE 0.1. – Schéma du processus de calcul du couplage exciton-phonon et de la luminescence assistée par les phonons. Les cadres verts et rouges indiquent l'utilisation de QUANTUM ESPRESSO et `yambo` comme codes de simulation, respectivement.

Un schéma du processus de calcul est présenté dans la Fig. 0.1, qui contient également le nom des codes de simulation utilisés.

Après avoir présenté l'état de l'art théorique, nous passons aux résultats de cette thèse. Dans le Chapitre 3 nous reportons nos résultats obtenus sur le hBN massif soumis à une déformation uniaxiale. Nous commençons par présenter les motivations expérimentales. Nous avons tenté de reproduire la variation d'intensité relative des différents pics dans les spectres de cathodoluminescence d'un feuillet de hBN déposé sur un substrat nanostructuré qui induit une déformation de l'échantillon. A différents endroits du cristal, les pics correspondants à des transitions assistées par des phonons acoustiques voient leur intensité augmenter par rapport aux pics des phonons optiques, en corrélation avec la déformation de l'échantillon. Pour simuler ces conditions, nous appliquons une déformation uniaxiale à un cristal de hBN massif. Nous avons étudié l'effet sur les propriétés électroniques, phononiques et excitoniques pour des valeurs allant d'une compression de 2.5% à un étirement de 2.5% de la longueur à l'équilibre. Nous observons que la déformation induit une brisure de symétrie et que la zone de Brillouin n'est plus un hexagone parfait. Les fréquences de phonons sont augmentées ou diminuées, suivant les modes considérés et la valeur de déformation appliquée. Il en va de même pour les bandes électroniques. Nous proposons une interprétation en terme d'interaction inter-feuillets, qui dépend fortement de la distance entre les feuillets superposés et qui et modifiée avec la déformation. Nous constatons que la brisure de symétrie lève la dégénérescence dans les orbitales à extrémités des bandes de valence et conduction. Ceci les points de haute symétrie dans l'espace réciproque K et M non-équivalents aux points K' et M'. Il y a donc quatre transitions non-équivalentes extrêmement proches en énergie.

La levée de dégénérescence a également un effet sur les énergies des excitons. Nous observons que les deux excitons directs avec les plus basses énergies, qui sont doublement dégénérés à l'équilibre, se séparent et donnent quatre niveaux distincts. L'énergie des excitons directs décroissent pour des étirements et croissent pour des compressions. Pour les excitons indirects, qui ne sont pas dégénérés, la tendance n'est pas la même et leur énergie décroît pour toutes les valeurs de déformation. L'effet de la séparation des niveaux d'énergie est clairement visible sur le spectre d'absorption où l'on voit apparaître un deuxième pic, provenant de la séparation de l'exciton blanc en deux états. L'effet est également visible sur la fonction d'onde de ces deux nouveaux états : en effet les deux ne sont pas orientés suivant la même direction cristallographique.

Dans la section 3.5, nous présentons l'approche utilisée pour calculer l'effet des phonons sur les excitons. Le couplage est obtenu par une dérivée aux différences finies de la fonction de réponse ou des dipoles excitoniques, de façon équivalente. Cette dérivée permet de calculer le couplage des excitons à moments finis avec les modes de phonons ayant les mêmes moments. Il est donc nécessaire de construire des supercellules pour pouvoir capturer la périodicité des modes de phonons aux moments choisis. Dans notre cas et comme évoqué plus haut, il nous faut considérer toutes les transitions non-équivalentes donnant des excitons indirects à très proche énergie. Tout ceci nous conduit à présenter les spectres de luminescence à différente valeur de déformation dans la Fig. 0.2.

Ces résultats montrent un élargissement des répliques de phonon à faible valeur de déformation, ainsi qu'une faible augmentation de l'intensité des pics à haute énergie. Ceci est causé par l'inclusion des quatre transitions non-équivalentes proches en énergie. Nous voyons que ces pics se séparent de plus en plus avec l'augmentation de la compression, jusqu'à ce qu'un seul pic subsiste à -2.5%, une compression relativement importante. Ces résultats vont dans le sens des mesures expérimentales mais l'accord n'est pas total. L'utilisation d'un nombre restreint de moments de phonons et d'excitons est une limitation. Il se peut aussi que des facteurs expérimentaux aient été négligés par notre méthode, comme le fait que la déformation ne soit pas nécessairement uniaxiale.

Dans le Chapitre 4, nous présentons un approche pour calculer le couplage exciton-phonon qui permet de surpasser la méthode par différences finies. Nous utilisons la théorie des perturbations pour inclure de façon dynamique l'interaction électron-phonon à l'intérieur d'un Hamiltonien. Celui-ci contient les éléments de couplage exciton-phonon, qui sont construits à partir de quantités calculées *ab initio* d'une part avec la BSE et en DFPT d'autre part. Ensuite, nous reformulons le problème pour obtenir une self-énergie décrivant l'interaction exciton-exciton médiée par des phonons. De cette façon nous pouvons écrire une fonction de réponse du système contenant une correction dynamique due à l'interaction avec les phonons. Cette correction dynamique est une avancée du point de vue théorique car elle permet d'obtenir les satellites de phonons dans les spectres

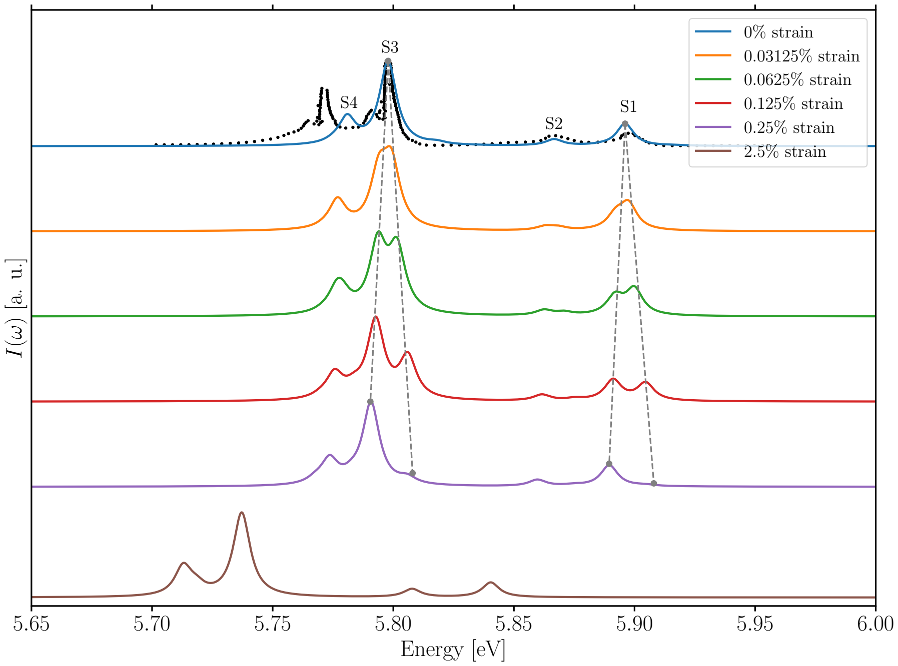

Figure 0.2. – Spectres de luminescence en fonction de la déformation, pour des valeurs choisies de compression. Les courbes sont déplacées verticalement par souci de clarté. Les données expérimentales sont reportés par les points noirs de la courbe du haut. Les spectres sont décalés en énergie pour correspondre à l'expérience. Les lignes pointillées sont un guide visuel.

optiques et surtout la renormalisation qu'ils causent à l'intensité des pics directs. De cette façon nous pouvons comparons l'intensité relative des processus directs et des transitions indirectes assistées par les phonons. Ceci s'accompagne d'une avancée sur le plan numérique étant donné que notre formulation comprend le couplage de tous les excitons avec tous les modes de phonons, sur toute l'étendue de la zone de Brillouin.

Nous avons implémenté cette approche dans le code `yambo`, et nous l'avons testée sur le hBN massif pour lequel nous pouvons nous comparer à une littérature expérimentale et théorique abondante. Notre spectre obtenu est en plutôt bon accord avec l'expérience pour la position des pics et l'intensité du doublet LA/TA. En revanche, l'intensité du doublet LO/TO est inversée par rapport à l'expérience. De plus nous constatons l'apparition d'un satellite causé par les phonons ZA/ZO, qui ne devrait pas être visible car interdit par symétrie. Nous attribuons ces problèmes à la façon dont nous construisons les éléments de matrice de couplage exciton-phonon. En effet, ceux-ci sont obtenus par le produit d'une quantité phononique et un quantité excitonique qui ne sont pas calculées avec la même phase de Kohn-Sham de départ. Ce problème peut être réglé en désactivant l'utilisation des symétries de la zone de Brillouin et en écrivant une interface avec un troisième code de simulation, comme l'a été montré après la publication de nos résultats par un collaborateur. Cependant, appliquer cette solution augmente considérablement le temps de calcul et surtout l'espace disque nécessaire pour obtenir le couplage exciton-phonon sans le problème des phases. Etant donné que les ordres de grandeur des intensités sont corrects, nous avons décidé de continuer et d'appliquer cette méthode au feuillet monoatomique de hBN (mBN).

Nous avons étudié les propriétés excitoniques du mBN en détail. La dispersion d'excitons contient un minimum global au point K, donnant un caractère indirect à ce matériau, en contradiction avec les mesures expérimentales. Cet exciton provient des transitions électroniques entre la bande de valence et les états quasi-libres à $Gamma$ dans l'approximation GW. Cette vallée excitonique pourrait être la plus peuplée et causer l'extinction du signal de luminescence. Après une étude de la fonction d'onde et du couplage exciton-phonon de cet état, nous avons décidé de ne pas utiliser l'approximation GW et de rester au niveau DFT+BSE, où ce problème est non-existant. L'étude des éléments de couplage exciton-phonon résolue en moment nous montre que le couplage est maximal dans une petite région autour de Γ et quasiment nulle aux bords de la zone de Brillouin.

Nous avons finalement calculé le spectre de luminescence du mBN libre. Nous l'avons comparé à trois spectres expérimentaux publiés récemment. Les structures apparaissant dans les trois spectres ne sont pas les mêmes et les interprétations sur leur origine diffèrent. Nous reportons nos résultats et leur comparaison aux spectres expérimentaux dans la Fig. 0.3

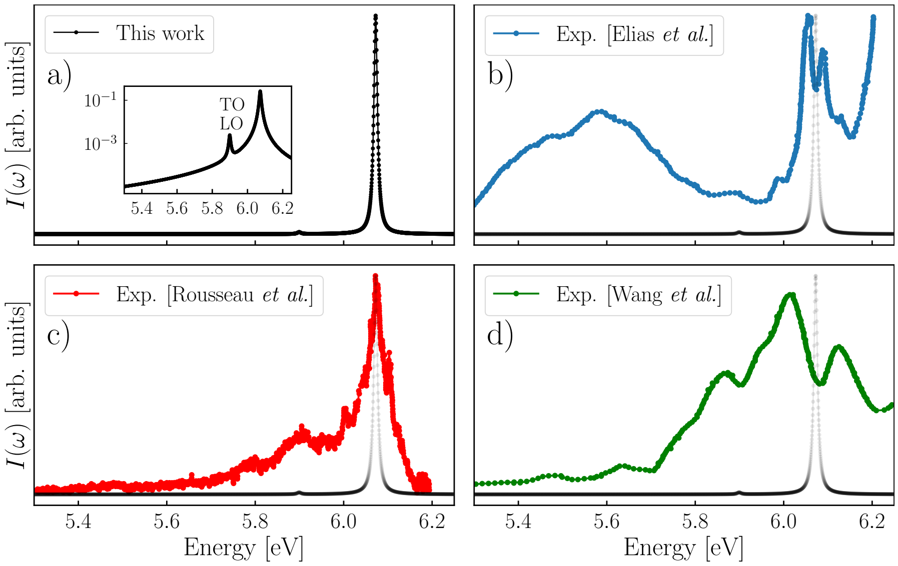

FIGURE 0.3. – Spectre de luminescence calculé pour la monocouche de hBN (a) comparé aux résultats expérimentaux dans les Ref. [1](b), Ref. [2](c) et Ref. [3](d). Les spectres calculés ont été décalés en énergie pour s'accorder avec le pic principal du panel (c). Par souci de clarté, nous avons tracé le spectre calculé sur chaque panel. Dans l'encadré du panel (a) nous montrons la même courbe en échelle semi-logarithmique, qui révèle le satellite à moindre intensité.

Grâce à notre méthode, nous pouvons comparer l'intensité relative du pic direct et des satellites de phonons, interprétés comme visibles dans certains des spectres. Nos résultats montrent un pic direct très intense. Nous voyons également un satellite issu du couplage entre l'exciton direct et des phonons optiques, mais dont l'intensité est inférieure à celle du pic direct de deux ordres de grandeur. Concernant des satellites issus du couplage de phonons avec un exciton indirect, nous n'en voyons pas apparaître. Nous pouvons donc éliminer l'hypothèse selon laquelle les structures expérimentales seraient des satellites de phonons.

Nous avons étudié l'influence du substrat graphitique présent dans deux des trois expériences. Premièrement, l'influence du substrat augmente l'énergie de l'exciton problématique à K, ce qui valide notre choix de ne pas le considérer. Ensuite, nous avons modélisé l'effet de l'écrantage du substrat sur le spectre de luminescence avec un modèle. Nous en avons conclu que l'influence du substrat n'est probablement pas assez forte pour révéler les satellites de phonon. Cependant la complexité de nos calculs ne nous permet pas d'utiliser un modèle élaboré voire un calcul direct d'une épaisseur finie de substrat en plus du mBN.

Enfin nous présentons dans la section 4.7 nos résultats préliminaires sur une autre phase de hBN, la phase Bernal qui correspond à un empilement AB des feuillets. Ce matériau a des gaps directs et indirects proches en énergie, ce qui pourrait révéler les signatures des excitons directs et des satellites de phonons de le même spectre de luminescence, à des intensités comparables. Nos premiers résultats tendent vers une luminescence directe, mais ceci fera l'objet d'une étude numérique plus poussée.

En conclusion cette thèse présente des spectres de luminescence calculés à partir de premiers principes. Deux méthodes différentes de calcul du couplage exciton-phonon ont été présentées et permettent d'obtenir une compréhension des processus donnant naissance aux structures dans les spectres. Les résultats présentés ouvrent des perspectives d'amélioration à la fois théoriques et numériques dont certaines sont activement explorées. Finalement, nous espérons que ces travaux peuvent avoir un impact et contribuer à l'élaboration de composants opto-électroniques ou photovoltaïques.

Acknowledgments / Remerciements

First I would like to thank the board of Doctoral School 352 that granted me this PhD funding, Andrea Marini for hosting me one week in Rome, funded by the Cost Action TUMIEE, Daniele Varsano and HPC Europa3 for allowing me a 2-month visit in Modena.

I would like to thank my supervisor Claudio for his constant support, his availability, for giving me the freedom to study the things I wanted and for his wise decisions that helped me to become a scientist. Un ringraziamento speciale per il tempo che hai dedicato alla revisione di questo manoscritto.

I thank Fulvio for the time he dedicated to train me on different topics and for his hospitality in Roma and Modena.

I would like to thank Khaoula Boukari and Andres Saul for the management and maintenance of the computer cluster *Rosa* which was an undeniable advantage for this PhD work.

I thank the TSN department as a whole for scientific discussions and at large, everyone who I discussed about science with and who sated my hunger for understanding, Davide Sangalli, Elena Cannuccia, Adrien Rousseau, Thibaut Sohier, Pedro Melo, Martino Silvetti, Matteo Zanfrognini, Riccardo Reho.

I thank the people I met in CINaM and who became my friends : Anna, Petr, Clémence, Céline, Alex, Julien, Diego, Ilan, Rajarshi, Guillem, Djouher, Mathilde, Kostis, Tarik, Gaëlle, Giorgia, Luigi, Mohit, Vyshnav. You contributed to brighten the sometimes gloomy days.

I thank Vitaly, Laura, Miguel and Kalyani for their help in the organization of YRM 2022 which was quite an experience, Véronique, Régine, Lydia, Cindy, Sabina for the precious administrative help, and Christophe for the budgetary rescue.

I thank Marine Baujon for helping me manage things that felt bigger than me at times.

I thank everyone for good times in Marseille and elsewhere Sam, Yann, Jonathan, Pavlo, Vasile, Thaïs, Simon, Inès.

Merci à mes proches qui donnent un sens à tout ceci. Jules, Pieric, Valentin, Yann, merci de votre soutien indéfectible, vous êtes des amis formidables.

Un simple merci ne suffirait pas pour exprimer ma gratitude envers mes parents et ma famille. Merci Maman et Papa pour m'avoir toujours soutenu et exprimé votre fierté. Merci Baptiste et Maxime d'être des frères admirables. Merci Côme et Thaïs de bien vouloir jouer avec moi.

Table des matières

Table des figures

Liste des tableaux

List of acronyms

MBPT
Many-Body Perturbation Theory. 32–34, 42, 71, 88, 95, 117

PES
photoemission spectroscopy. 52, 96

RPA
Random Phase Approximation. 50, 51

UV
ultraviolet. 31

1. Introduction

Modern society faces a wide range of challenges that require complex and multifaceted solutions. The challenges posed by climate change and the necessity for clean energy in order to reduce greenhouse gas emissions intersect with the goals of economic growth and the global exchange of information, goods and people. Unprecedented issues are emerging from this increasingly technologically advanced and interconnected civilization.

This PhD work was initiated amidst the most impactful public health crisis of our time, the COVID-19 pandemic. Despite all the negative facets of this pandemic, it unexpectedly gave a boost to a specific market : the emerging technology of deep ultraviolet violet light-emitting diodes (UVC LEDs), and the market is predicted to grow five-fold.[4] Indeed the deep UV light, *i.e.* with wavelengths ranging from 100 to 280 nm, has been demonstrated to inactivate the coronavirus accountable for the disease, thus making it harmless.[5] Besides surface disinfection, UVC LEDs have many applications in water and air depolution, agriculture, printing and more.[6] The material studied in this thesis, hexagonal Boron Nitride, is a candidate of choice for the elaboration of UVC LEDs due to its bright light emission in the deep ultraviolet.

This is a recent example of how technological innovations resulting from scientific research in materials science can provide a means to address the challenges of modern society. The European Union supports such research, in particular through the Flagship projects, which are large-scale research initiatives with an emphasis on technology transfer to industry. Three out of the four Flagship projects are closely related to materials science: Batteries30+ for the development of efficient and compact energy storage,[7] Quantum Technologies[8] for the quantum computers and algorithms and Graphene,[9] which focuses on two-dimensional materials. All of these are research projects that could provide means to produce clean energy and store it. In all of these scientific areas, theory and numerical simulations are essential to support the experimental discovery of materials and guide the engineering of new devices. This is particularly relevant in Condensed Matter Physics which is the subject of this thesis. Since the discovery of Graphene and its extraordinary properties by Novoselov and Geim in 2004,[10] the two-dimensional materials such as Graphene, black Phosphorus, transition metal dicalchogenides (TMDs) and hexagonal Boron Nitride (hBN) have attracted a great deal of attention. Indeed, they exhibit a range of electronic and optical properties that allow the design of devices for different applications, especially when different layers are stacked to form the so-called van der Waals heterostructures.[11] The resulting devices are then very compact and fit very well into the technological trend of device miniaturization.

With the variety of optical and electronic properties offered by all the existing monolayers, and the ability to engineer them with factors such as stacking of different layers,[12] twisting angle between them,[13, 14] and straining[15] as well as their interaction with substrates, the possibilities for devices are almost limitless. In this ecosystem, hexagonal Boron Nitride is a candidate of choice for its structural, electronic and optical properties.

The process of luminescence

Optical measurements are an efficient way to characterize materials and reveal the microscopic, quantum, interplay between electronic wavefunctions and electromagnetic field of light, and collective quantum effects in the crystal.[16] In particular, spontaneous emission of light after an excitation, known as *luminescence*, is the key property for the elaboration of light-emitting diodes.[17]

For spontaneous light emission to happen in a semiconductor or insulator, there needs to be a population of excited electrons in the conduction band. The excitation can have different forms. It can be done with the electromagnetic field of external light, then the process is called photoluminescence. If the electrons are excited by an external beam of electrons colliding with the crystal, it is called cathodoluminescence. If they are excited by an external electric field, it is called electroluminescence, *et cetera*. When the electrons are promoted to the higher-energy conduction bands, they leave an empty state in the valence band. This empty state can be thought of as a *hole* in the Fermi sea of the valence states. It propagates with the opposite of the electron's momentum and has a negative effective mass. For light to be emitted, the excited electrons need to de-excite and go back to the empty states. We speak of radiative recombination of an electron-hole pair. When the hole and the electron have the same momentum (and the same spin and symmetry) the radiative recombination can happen because the emitted light carries an almost null momentum, hence respecting momentum conservation. The energy difference between the electron and the hole corresponds to the frequency of emitted light, multiplied by $\hbar$. However when the bottom of the conduction band is not at the same momentum than the top of the valence band, the light emission cannot happen directly because of momentum conservation. There needs to be a second-order process to exchange momentum. For instance, the excited electron can transfer its momentum to another one in the conduction band and then recombine with the hole. This process is known as Auger-Meitner recombination.[18] Otherwise, the momentum exchange can come from the absorption or emission of a phonon, hence gaining or losing energy and momentum and finally leading to a radiative recombination. This is known as a phonon-assisted transition and it is the process that is studied in this thesis.

Luminescence is often thought of as the reverse process of light absorption. Indeed in absorption, light with a frequency higher than the gap can excite electrons and promote them to the conduction band, with almost zero transfer of momentum. In the case of phonon-assisted transitions, the electron can be promoted to the conduction band at another momentum, thanks to the absorption or emission of a phonon.

Because of this similarity, the spectra of absorption and of luminescence are quasi symmetrical for direct transitions. The slight asymmetry come from the phonon broadening of the electron density of states, known as the Stokes shift. However when considering phonon-assisted transitions, the asymmetry will be more pronounced because the interplay between direct and indirect processes will lead to quite different features in the two spectra.

In this thesis, we study the properties of different forms of hBN and develop theoretical and numerical methods with the aim of reproducing and predicting their luminescence spectra from *ab initio* calculations.

The peculiar properties of hexagonal Boron Nitride

The first reported synthesis of Boron Nitride dates back from 1842.[19] It is now available commercially under the form of a white powder and finds applications as lubricant or for its high thermal resistivity. It can be found under the form of a layered material composed of atomically thin layers arranged in a honeycomb lattice. High-purity crystals are synthesized under high-pressure and high-temperature conditions.[20] Different stacking of the layers lead to different stable or metastable polytypes. In this thesis we will be mainly concerned with the AA' and the AB stackings, that are illustrated in Fig. 1.1. We will refer to the AA' polytype as hBN and to the AB polytype (or Bernal phase) as bBN. The atoms within a layer are bond by hybrid sp^2 bonds, while the interlayer interactions are of van der Waals type. hBN is stable at ambient pressure and room temperature. It is an insulator with a gap of about 6 eV. Due to its low lattice mismatch with Graphene and its insulating character, it is a substrate of choice and

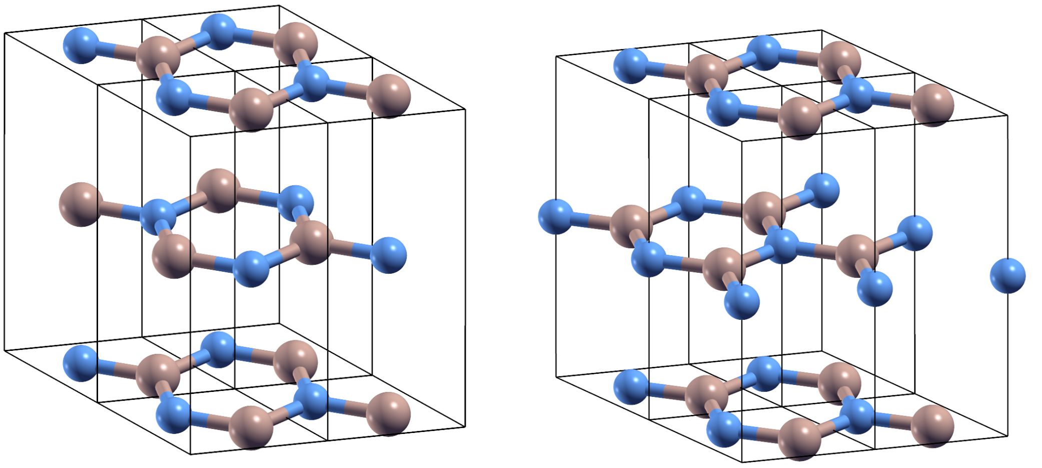
(a) AA' stacking

(b) AB stacking

Figure 1.1. – Two polytypes of hexagonal Boron Nitride where four hexagonal unit cells are shown. Boron atoms are represented with brown spheres, Nitrogen with blue ones. We will refer to the AA' polytype as hBN and to the AB polytype (or Bernal phase) as bBN.

a good encapsulation layer for Graphene-based applications.[21] It also has a variety of defect-related physics that can find applications for quantum computing,[22] single photon emission[23] or bright color center emission.[24] However the property of interest for this thesis is the bright light emission in the deep UV domain and the rich features appearing in the luminescence spectra. hBN was shown to have a very high internal quantum yield, comparable to that of a direct gap material such as Zinc Oxide.[25] This is due to the strong exciton-phonon coupling enhanced by the anisotropy of this layered material and to the large density of transitions due to flat bands in the electronic dispersion.[26] Experimental luminescence spectra for the bulk material are abundant in literature, see for instance Refs. [25, 27]. These spectra exhibit a fine structure due to the scattering with different phonon modes as was reproduced by first-principle calculations in Refs. [28, 29] However, obtaining the optical absorption spectrum experimentally requires more advanced equipment because hBN absorbs in the UV range. In Ref. [30] it was obtained using synchrotron radiation for a large range of frequencies. In general the absorption (or a quantity proportional to it such as the photoluminescence excitation [1]) and the luminescence spectra have a strong asymmetry, as can be seen in Fig. 1.2, because the state dominating the absorption is different from the one dominating the luminescence, which is at lower energy. Moreover the coupling with different phonon modes gives rise to multiple peaks in the luminescence spectrum, only visible in absorption with a very fine resolution because the direct peak overlaps with them. This will be explained in details in the body of this thesis.

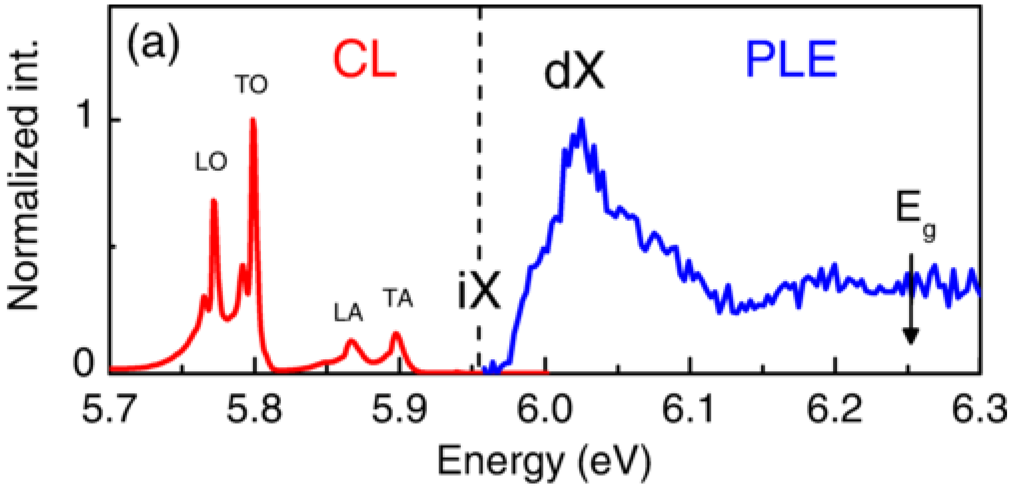

Figure 1.2. – Comparison between the cathodoluminescence (red) and the photoluminescence excitation (blue), which is proportional to absorption of bulk hBN. iX and dX refer to indirect and direct exciton energy, respectively. E_g indicates the gap energy. Extracted from Ref. [25].

---

[1] Photoluminescence excitation (PLE) is the measure of the luminescence intensity as a function of the energy of the laser that excites the system. The PLE signal is the highest where the system absorbs the most light.

As for the Bernal phase (bBN), it was recently synthesized and characterized with optical measurements. Its photoluminescence spectrum was reported in Refs. [31, 32]. It seems to exhibit direct and indirect gaps very close in energy, as theoretically predicted in Ref.[12], giving rise to direct peak and phonon satellites with comparable intensities. This case is addressed at the end of Chapter 4.

For a single layer, measuring the luminescence intensity is much harder because the signal is faint due to the low thickness of the material. To have a good resolution, one needs to be at cryogenic temperature in ultra-high vacuum, and have an extremely pure sample. Cathodoluminescence measurements were performed for sheet thicknesses down to six layers,[33] but the signal-to-noise ratio becomes too low for smaller thicknesses. [2] Photoluminescence measurements are equally difficult to obtain, but some results were published recently for monolayers grown by epitaxy on a Graphite substrate,[1, 3] or mechanically exfoliated and deposited on an SiO_2 substrate.[2] These three spectra exhibit features that are quite different, and their interpretation is not unanimous. We address this question in Chapter 4.

On the theoretical point of view, absorption spectra are relatively easy to obtain from state-of-the-art *ab initio* calculation, but luminescence is more difficult since it is an out-of-equilibrium process. Moreover, a general formulation of luminescence that includes both direct and phonon-assisted transitions on the same footing from first-principles is still lacking. This thesis contributes towards this goal.

Scope of the thesis

The state-of-the-art theoretical framework in which our calculations are contained starts from the widely used Density Functional Theory (DFT).[35] In this theory the electrons are treated as independent particles evolving in a mean-field created by the other electrons and the ions are treated as classical particles interacting *via* this mean-field. It allows to compute the ground state electronic density of the crystal and to obtain the equilibrium geometries, with a certain set of approximations. From there we extract the Kohn-Sham eigenvalues and wavefunctions. These eigenvalues give an approximation to the band structure and are the starting point of the more involved Many-Body Perturbation Theory (MBPT).

MBPT is based on Green's functions and treats the many-body interactions as a perturbation of the independent-particle system. The electrons become *quasiparticles*, whose evolution in time and space is easier to describe than the full many-electrons system.[36, 37] With this we are able to obtain a more accurate band structure and simulate experiments that involve charged excitations – *i.e.* addition or removal of an electron of the system.

However the neutral excitations of the many-electron system – *i.e.* an electron being excited but staying in the system – are not well described at this point. To this end we

---

[2] We mention for exhaustiveness Ref. [34] where cathodoluminescence was reported for a single layer of BN, however the signal-to-noise ratio is very small and this article has not been peer-reviewed yet.

need the two-particle response functions within MBPT, that are calculated starting from the quasiparticle band structures including correlation effects that take into account the electron-hole interaction. We can formulate the problem in terms of electron-hole pairs bound by the Coulomb interaction that are called *excitons*. They play a significant role in the optical spectra of hBN and including their effects gives a much better agreement with experiments compared to independent-particle or quasiparticle levels of theory. A link can be made between microscopic excitonic quantities and macroscopic observables measured experimentally.[38]

Finally, we use a perturbative method based on DFT to obtain the vibrational properties of the crystal in the harmonic approximation, meaning that each atom is represented as an harmonic oscillator vibrating around its equilibrium position. It is called Density Functional Perturbation Theory (DFPT).[39] In second quantization, it gives a description of the vibrational modes of the lattice in terms of quanta of vibration called *phonons*. They are another type of quasiparticle, that is a collective excitation, with a definite frequency and wave vector, analogous to the crystal momentum of electrons. We can now reintroduce the coupling between nuclear and electronic motions and formulate the electron-phonon coupling in second quantization. Since we are interested in the role of phonons in the optical response, we have to consider the coupling between excitons and phonons.

In condensed matter, this problem and the resulting phonon-assisted luminescence is an old topic. The first studies date back to the 1960s by Toyozawa *et al.*[40, 41] and the first dynamical solution of the BSE, the so-called Shindo solution, was proposed precisely to study the exciton-phonon problem.[42] For model semiconductor quantum wells, the time-evolution of correlation functions, that includes simultaneous exciton-phonon and exciton-photon scattering, was studied in Ref. [43]. However this approach requires material-dependent parameters and is computationally expansive for real materials.

With the increase in computing capabilities, computationally heavy theories such as MBPT became in reach and further developed to study more challenging materials. We can cite a few works on this regard such as the theory of Hallen-Bardeen-Blatt for phonon-assisted absorption of indirect semiconductors, [44] applied using first-principles for Silicon.[45] Later, Perebeinos *et al.* introduced the coupling with excitons, absent from the previously mentioned theory, to study the optical absorption of carbon nanotubes with a combined tight-binding and *ab initio* approach.[46]

Zacharias *et al.* derived a formalism based on Williams-Lax theory[47, 48] to treat phonon-assisted transitions on the same footing as vibrational renormalization of the electronic band structures, but only for independent particles.[49] They further included excitonic effects in the optical absorption from finite differences [50] in monolayer Germanium Selenide. This methodology is based on a finite-difference derivative scheme to compute the exciton-phonon coupling. This goes beyond previous approaches developed independently by Paleari *et al.* in Ref. [29] and Cannuccia *et al.* in Ref. [28] in the sense that in the two latter references, the renormalization of the exciton energies due to the coupling with phonon is neglected. This approximation is well suited for the study of large indirect gap semiconductors and insulators and indeed they applied the methodology to the calculation of phonon-assisted luminescence of bulk hBN, which were the first times such spectra were obtained from first principles. Moreover, Paleari *et al.* and Cannuccia *et al.* included dynamical effects not present in the work of Zacharias *et al.* This is the approach we will present in detail in Chapter 3 and that we applied to the study of luminescence of strained hBN.

Other formulations of the exciton-phonon problem beyond the perturbative approach are present in the literature, such as the polaron transformation in Ref. [51], the use of the density matrix in Ref. [52], the formulation in terms of two-particle Green's functions from Ref. [53] or the more general real-time approach from Ref. [54] as well as the cumulant *ansatz* to include scattering of excitons with multiple phonons from Ref. [55]

In order to simulate materials that present both direct exciton peaks and phonon-assisted replicas in their luminescence spectrum one needs an approach that takes into account the dynamical renormalization of the direct emission peaks due to the interaction with phonons. Many of the approaches presented above do not consider this effect, that is one of the main developments of this thesis. This development is presented in Chapter 4, where we compute the exciton-phonon matrix elements by treating the interaction of excitons and phonons with second-order perturbation theory. This allows to obtain an exciton-phonon interaction Hamiltonian. We can reformulate the Hamiltonian problem in the form of a response function including a dynamical correction due to scattering with phonons. This correction gives rise to the appearance of phonon-assisted peaks in the optical spectra, and it yields their renormalization of the direct excitonic peaks. The main advantage of this *ab initio* approach is that we can compare the direct and indirect phonon-assisted processes in the luminescence spectra, while doing all the necessary calculations in the unit cell.

A sketch of the workflow we used to obtain the exciton-phonon coupling and phonon-assisted luminescence is drawn in Fig. 1.3. The simulation code we used for DFT and DFPT is the QUANTUM ESPRESSO suite.[56, 57] For the MBPT calculations, we used existing features of the `yambo` code,[58] and we implemented new features for the exciton-phonon coupling and phonon-assisted luminescence.

Structure

This thesis is structured as follows. In Chapter 2, we summarize the theoretical background necessary to our exciton-phonon calculations and phonon-assisted luminescence. We start by briefly introducing DFT, then we sketch a derivation of the Hedin's equations and obtain the GW Approximation (GWA). We proceed by deriving the Bethe-Salpeter Equation (BSE) and introducing the concept of *excitons*. We present the link between the obtained many-body, microscopic quantities and the macroscopic observables measured in experiments. In the last part of this Chapter, we present DFPT, the theory we use to compute *phonons* and electron-phonon coupling from first-principles.

Chapter 3 is devoted to bulk hBN under strain. We present our results concerning the effect of uniaxial strain on the electronic, phononic and excitonic properties of hBN. Then,

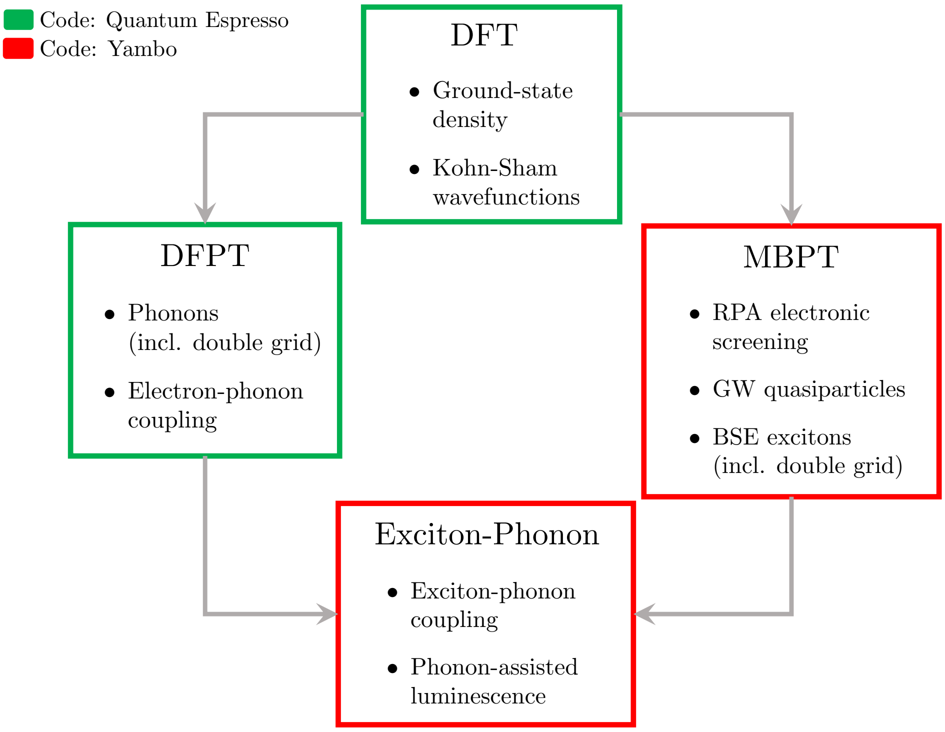

Figure 1.3. – Workflow of the calculations to compute exciton-phonon coupling and phonon-assisted luminescence. The green and red boxes indicate that we used Quantum ESPRESSO and `yambo` as simulation codes, respectively.

we explain the finite-difference method we used to compute the exciton-phonon coupling in a static way, using displaced atoms in supercells. Finally, we show our luminescence results for the strained crystals and discuss their agreement with available experimental results.

In Chapter 4, we present the derivation of the exciton-phonon coupling *ab initio*, from first-order perturbation theory. From this we are able to obtain a response function containing a dynamical correction due to the coupling of excitons and phonons. We apply this approach to compute the luminescence spectrum of monolayer hexagonal Boron Nitride (mBN) and address contradictory experimental interpretations of the structures therein. We also show preliminary results of the calculated luminescence of Bernal Boron Nitride (bBN), which might exhibit both direct peak and phonon satellites with comparable intensities.

At the end of each chapter is a summary box with a summary of the chapter's key concepts and methods.

At the very end of this document, five appendices complement the main text and provide additional information on the materials and computational details.

2. State of the art theory

Contents

2.1. Introduction to the many-body problem

In this thesis, most of the computed quantities are not based on any parameter. The only input required is the chemical composition of the system, *i.e.* the atomic numbers of the atoms constituting the crystal. This way of calculation is called *ab initio*. It is a powerful framework since it does not require to fit any parameter to experiments and it can include all the physical phenomena one wants to consider. One of the shortcomings is that we often need to resort to approximations for the problems to be solvable numerically. To perform such calculations, we need to consider all nuclei and all electrons in the crystal, as well as all the interactions between them. The system of interacting electrons and nuclei in a material can be described by the following Hamiltonian :

$$\begin{aligned}\hat{H} = &-\sum_{I} \frac{\hbar^2}{2M_I}\nabla_I^2 + \frac{1}{2}\sum_{I\neq J}\frac{Z_I Z_J e^2}{|\mathbf{R}_I - \mathbf{R}_J|} \\ &-\frac{\hbar^2}{2m_e}\sum_i \nabla_i^2 + \frac{1}{2}\sum_{i\neq j}\frac{e^2}{|\mathbf{r}_i - \mathbf{r}_j|} - \sum_{i,I}\frac{Z_I e^2}{|\mathbf{r}_i - \mathbf{R}_I|}\end{aligned} \tag{2.1}$$

where capital indices refer to nuclei and lowercase indices refer to electrons. Z_I, M_I and $\mathbf{R}_I$ are the atomic number, the mass and the position in real space of nucleus I, and m_e, $\mathbf{r}_i$ are the electron mass and position in real space. In this thesis, unless explicitly specified, we will use the atomic units, that is $\hbar = m_e = e = \pi/\varepsilon_0 = 1$. The terms on the first line are the kinetic energy of the ions and the ion-ion interaction, respectively. On the second line we have the kinetic energy of electrons, that we will later denote T_{ee}, the electron-electron interaction V_{ee} and finally the electron-nucleus interaction, which we will refer to as the external potential felt by electrons in equilibrium, V_{ext}. This Hamiltonian is difficult to solve for a system containing two nuclei and two electrons, and is untractable for a larger number of particles. The kinetic terms and the interaction terms can be solved separately, but their combination is a formidable problem. To greatly simplify this Hamiltonian, we use the so-called Born-Oppenheimer approximation. It consists in considering that the nuclei move in a much longer time-scale than the electrons, because their masses are much greater than those of the electrons. Every time we compute the electronic part, we consider that the nuclei do not have time to move from their equilibrium position. [59] We can then split the Hamiltonian into a nuclear term and an electronic term, and the nuclear part is just an additive constant. The electronic Hamiltonian then reads :

$$\hat{H}_e = \hat{T}_e + \hat{V}_{ee} + \hat{V}_{ext} \tag{2.2}$$

The first and second term are universal for all systems.The peculiarities of any systems are included in the last term in the above equation.

2.2. Density Functional Theory

Density Functional Theory (DFT) is vastly used in solid-state physics and quantum chemistry. In this thesis, it will be the starting tool to compute structural and electronic properties of our systems. The idea behind DFT is to replace the real system of interacting electrons by an auxiliary system of non-interacting particles evolving in an effective potential. DFT is an exact theory in principle and allows one to compute the ground state of the many-electron system.

DFT is based on the work of Hohenberg and Kohn who stated and proved two fundamental theorems. [60] The first one ensures there is a one-to-one correspondence between the electronic density and the external potential acting on the system. The second theorem states that the total energy of the system is a functional of the electronic density. The total energy of a system of interacting electrons is written as :

$$E = \langle\Psi|\hat{H}|\Psi\rangle = \langle\Psi|\hat{T} + \hat{V}_{ee}|\Psi\rangle + \int d\mathbf{r} v_{ext}(\mathbf{r})n(\mathbf{r}) \tag{2.3}$$

By virtue of the Hohenberg and Kohn theorems, the total energy is a functional of the density and can be written as :

$$E_{HK}[n] = F_{HK}[n] + \int d\mathbf{r} v_{ext}(\mathbf{r})n(\mathbf{r}) \tag{2.4}$$

where $F_{HK}[n] = \langle\hat{T}\rangle + \langle\hat{V}_{ee}\rangle$ is a universal functional of the density, *i.e.* the dependence on n of the functional is the same for all systems. The ground-state energy $E = E_0$ is the minimum of the energy functional at the ground-state density $n = n_0$. To be able to compute these quantities, Kohn and Sham reformulated the problem into an auxiliary system of non-interacting particles, that has the same density as the real system.[61] Its energy is :

$$E_{ip}[n] = T_{ip}[n] + \int d\mathbf{r} v_{\text{eff}}(\mathbf{r})n(\mathbf{r}) \tag{2.5}$$

The total wavefunction of the system is expressed as a Slater determinant of single-particle wavefunctions : $|\Psi\rangle = |\psi_1\psi_2\ldots\psi_{N_e}\rangle$. This reformulation is particularly helpful because it allows the kinetic energy term to be calculated analytically :

$$T_{ip} = \sum_{i}^{N_e} \langle\psi_i| - \frac{\nabla_i}{2}|\psi_i\rangle \tag{2.6}$$

The expression for the total energy functional in Eq. (2.4) can be rewritten as :

$$E_{KS}[n] = T_{ip}[n] + \int d\mathbf{r} v_{ext}(\mathbf{r})n(\mathbf{r}) + E_H[n] + E_{xc}[n] \tag{2.7}$$

where T_{ip} is the kinetic energy of the independent particles with density n, E_H is the Hartree energy, which is the classical electrostatic interaction :

$$E_H[n] = \int d\mathbf{r}d\mathbf{r}' \frac{n(\mathbf{r}')n(\mathbf{r})}{|\mathbf{r} - \mathbf{r}'|} \tag{2.8}$$

and E_{xc} is the exchange-correlation energy functional defined as :

$$E_{xc}[n] = \langle\hat{T}\rangle - T_{ip}[n] + \langle\hat{V}_{ee}\rangle - E_H[n]. \tag{2.9}$$

It is the difference between the exact kinetic energy and the independent particle one, T_{ip}, plus the difference between the exact electron-electron interaction and the Hartree energy functional. Hence it contains the quantum effects of exchange and correlation of fermions.

Since the auxiliary system is an ensemble of independent particles, one can write the so-called Kohn-Sham equations for each individual particle i :

$$\left(-\frac{\nabla^2}{2}+v_{\text{eff}}(\mathbf{r})\right)\psi_i(\mathbf{r})=\epsilon_i\psi_i(\mathbf{r}). \tag{2.10}$$

They are analogous to Schrödinger equation for a particle evolving in a local effective potential v_{eff}, that we have yet to determine. Their solutions are the auxiliary system's eigenvalues ϵ_i and eigenvectors ψ_i. Using these eigenfunctions we can construct the electronic density as :

$$n(\mathbf{r})=\sum_i f_i\left|\psi_i\right|^2 \tag{2.11}$$

where f_i is the occupation number of state i. Applying the variational principle to E_{ip} and E_{KS} we get

$$\left.\frac{\delta E_{ip}[n]}{\delta n}\right|_{n_0}=0\implies\left.\frac{\delta T_{ip}[n]}{\delta n}\right|_{n_0}=-v_{\text{eff}}(\mathbf{r}) \tag{2.12}$$

$$\left.\frac{\delta E_{KS}[n]}{\delta n}\right|_{n_0}=0\implies\left.\frac{\delta T_{ip}[n]}{\delta n}\right|_{n_0}=-v_H(\mathbf{r})-\left.\frac{\delta E_{xc}[n]}{\delta n}\right|_{n_0}-v_{ext}(\mathbf{r}) \tag{2.13}$$

Using the fact that the total kinetic energy is independent of the density at fixed number of particles, we get :

$$\begin{aligned}v_{\text{eff}}(\mathbf{r})&=v_{ext}(\mathbf{r})+\frac{\delta E_H[n]}{\delta n(\mathbf{r})}+\frac{\delta E_{xc}[n]}{\delta n(\mathbf{r})}\\&\equiv v_{ext}(\mathbf{r})+v_H([n],\mathbf{r})+v_{xc}([n],\mathbf{r}).\end{aligned} \tag{2.14}$$

At this point, we see that we have to solve the many-electron problem self-consistently. Indeed, the density is obtained by solving the Kohn-Sham equations which contain the effective potential. In turn, this potential depends on the density. In practice, one starts from a guess density and iterate over the self-consistent cycle until the quantities of interest vary less than an arbitrary threshold.

Density Functional Theory is often used as a reference for bandgaps and electronic dispersion calculations. One has to be careful when interpreting Kohn-Sham eigenvalues, because they do not bear any physical meaning. First, there is no guarantee that one can find an auxiliary system of non-interacting particles for any real system. Then, the excited states and bandgaps are not the physical ones.[62] This is why we will use a more refined theory presented in the next section.

Up to now, DFT is in principle an exact theory, as long as one can define an auxiliary system with the same density as the real system. However, there exists no analytical form of the exchange-correlation potential. Hence we will then have to resort to approximations to compute the density in practice.

Exchange-correlation functional approximations

The **Local Density Approximation (LDA)** is the first one that we present, and that we used for most of the results in this thesis. It was proposed by Kohn and Sham.[61] It consists in replacing the exchange-correlation energy density by the one of the homogeneous electron gas, which is local in the density :

$$E_{XC}^{LDA}[n] = \int d\mathbf{r}\ \epsilon_{xc}^{HEG}(n(\mathbf{r})) \tag{2.15}$$

The exchange energy density of the homogeneous electron gas is known : $\epsilon_X^{HEG}(n) = -\frac{3}{4}(\frac{3}{\pi}n)^{(1/3)}$, and the correlation energy density is obtained from interpolation of an accurate quantum Monte Carlo simulation for various values of densities.[63] The LDA is relatively simple and computationally inexpensive. It gives a satisfactory description of system with slowly-varying density, but also surprisingly good results for a larger range of materials. For instance, for layered materials such as hBN, the interlayer binding energies are rather accurate, due to the tendency of overbinding of the LDA which cancels the error induced by the lack of van der Waals interactions.

In the **Generalized Gradient Approximation (GGA)** the exchange-correlation energy density contains an additional dependence in the gradient of the density :

$$E_{XC}^{GGA}[n] = \int d\mathbf{r}\ \epsilon_{xc}^{GGA}(n(\mathbf{r}), \nabla n(\mathbf{r})). \tag{2.16}$$

This type of functional is obtained by setting some parameters to satisfy exact constraints. The structural and bonding properties are often improved with respect to the LDA. There are many more approximations going beyond LDA and GGA functionals that we will not detail here,[59] as we did not use them for the DFT calculations in this thesis.

Pseudopotentials

For our purposes, it is not necessary to describe every single electron in the crystal. In fact, for the range of energies we are interested in, the electrons that can be optically excited are those that occupy the highest valence shells. The core electrons of the first s and p shells are bound too strongly to the nuclei to be excited by a few electron-Volts incoming light. Hence, to simplify the system, we use pseudopotentials to avoid describing the core electrons. Pseudopotentials also solve the problem of the divergence of the Coulomb potential as $\mathbf{r} \to 0$, which leads to rapid oscillations in the wave functions of the occupied orbitals.[59] Beyond a given cutoff radius r_c, pseudopotentials are constrained to be exactly equal to the true potential. Below this radius, the pseudopotential does not diverge and assumes a finite value at $r = 0$, as can be seen in Fig. 2.1 This generates a pseudo-wave function which is smooth and does not oscillate below the cutoff radius. With this method, the Kohn-Sham eigenvalues of the higher valence states remain unchanged,

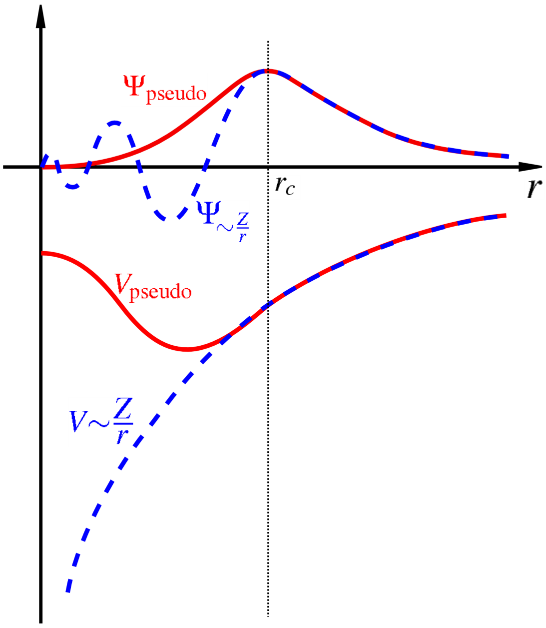

Figure 2.1. – Sketch of the pseudopotential compared to the real potential and the wavefunctions they generate.

and the computationally demanding task of representing the oscillating wave function is eliminated. The fact that fewer electrons have to be taken into account also helps to speed up the calculations.

Basis set

For real systems, the wave function of the crystal is an immensely complicated object whose analytical expression is out of reach. For computational purposes, one needs to represent it in a complete basis of the Hilbert space. Depending on the characteristics of the system, the choice of the basis functions is different.

In this thesis we study infinite, periodic crystals. A suitable basis for this case is the plane waves. It originates naturally from the Bloch theorem, which states that the wave function of an electron can be written as a product of a plane wave times a periodic function :

$$\phi_{j,\mathbf{k}}(\mathbf{r}) = u_j(\mathbf{r})e^{i\mathbf{k}\cdot\mathbf{r}} \tag{2.17}$$

The u_j functions have the same periodicity as the lattice. The Bloch wave has a wavevector $\mathbf{k}$. For infinite periodic crystals, this is a continuous variable belonging in the first Brillouin Zone (BZ). The quantity $\hbar\mathbf{k}$ is called the quasi-momentum of the electron, or *crystal momentum*. For brevity, we will call it momentum of the electron. We decompose the periodic functions u_j in plane waves as such :

$$u_j(\mathbf{r}) = \sum_{\mathbf{G}} c_{j,\mathbf{G}} e^{i\mathbf{G}\cdot\mathbf{r}} \tag{2.18}$$

where $c_{j,\mathbf{G}}$ are the coefficients of the plane waves basis, and the $\mathbf{G}$ are the reciprocal lattice vectors. The plane wave expansion of the band j follows :

$$\phi_{j,\mathbf{k}}(\mathbf{r}) = \sum_{\mathbf{G}} c_{j,\mathbf{k}+\mathbf{G}} e^{i(\mathbf{k}+\mathbf{G})\cdot\mathbf{r}} \tag{2.19}$$

In principle all complete bases of the Hilbert space yield equal representation of the wave function. As it is impossible to numerically sample a Hilbert space with infinite dimension, one has to truncate the representation. Thus, one has to make sure enough basis functions are included in the expansion to have an accurate wave function. In our case, we choose an energy cutoff E_{cut} such that :

$$\frac{1}{2}\left|\mathbf{k}+\mathbf{G}\right|^2 \leq E_{cut} \tag{2.20}$$

One has to verify that the cutoff is high enough so that the results are accurate, but setting it too high would mean including more plane waves which would slow down the calculations. Since the plane waves are orthonormal, adding extra ones to the basis by increasing E_{cut} does not add redundant physical information.[59] All the potentials entering the Kohn-Sham equations can be expressed in the plane waves basis, as well as the equations themselves.

2.3. Many-Body Perturbation Theory

As mentioned above, DFT is not well suited to simulate optics experiments of semiconductors or insulators. Optical excitations are neutral excitations, in the sense that the excited electron does not leave the system and can therefore interact with the hole it left behind in the valence band. This interaction between a hole in a valence band and an excited electron in the conduction bands is not accurately accounted for in DFT, as it is designed to calculate the total energy and the electronic density of the *groundstate*. For this reason, we resort to a more refined theoretical framework to treat the electronic correlations and study the excited states.

In this section I will present the basics of Many-Body Perturbation Theory (MBPT). In this theory, the many-body interactions are treated as a perturbation to the system of non-interacting electrons. I will detail the effects on the electronic structure and also the inclusion of the electron-hole interaction, to deal with optical excitations.

Including the many-body interaction in an Hamiltonian formulation would lead to computing immensely complicated wavefunctions for the system of N electrons, and this is not tractable. Instead, if we are more interested in observables such as optical spectra, we can reformulate the problem in terms of Green's functions. It is a mathematical object which is the solution of the equation of motion for the N interacting electrons, when the source term is a Dirac distribution. The link between the two formulation writes :

$$\begin{aligned}\left[i\partial_t - \hat{H}_e\right] \mathcal{G}(\mathbf{r},t;\mathbf{r}',t') &= \delta(\mathbf{r}-\mathbf{r}')\delta(t-t') \\ \mathcal{G}(\mathbf{r},\mathbf{r}',\omega) &= \left[\omega - \hat{H}_e\right]^{-1}\end{aligned} \tag{2.21}$$

The first line is the time-dependent Schrödinger equation for N interacting electrons. The second line gives the N-body Green's function in terms of the Hamiltonian, where we took the Fourier transform $t - t' \to \omega$. The one-body and two-body Green's functions are the first two matrix elements of $\mathcal{G}$. We will see in this section how to obtain many useful quantities from them, such as the electronic density, the total energy, the charged and neutral excitation energies and much more. The derivations in this section are adapted from textbooks,[38, 64] review articles [65, 37, 66] and lecture notes.[67]

2.3.1. Hedin's equations

We consider a system of N interacting electrons. We will consider the effect of nuclei motion in a later section. We start from the Hamiltonian for interacting electrons in second quantization:

$$\begin{aligned}\hat{H}_e = &\int dx_1\, \hat{\psi}^\dagger(x_1)h(\mathbf{r}_1)\hat{\psi}(x_1) + \frac{1}{2}\iint dx_1\, dx_2\, \hat{\psi}^\dagger(x_1)\hat{\psi}^\dagger(x_2)v(\mathbf{r}_1,\mathbf{r}_2)\hat{\psi}(x_2)\hat{\psi}(x_1) \\ &= \hat{H}_0 + \hat{H}_{int}.\end{aligned} \tag{2.22}$$

where $\hat{\psi}(x)$ is a field operator in Schrödinger representation, h is the single-particle Hamiltonian for non-interacting particles evolving in an external potential V_{ext} and $v(\mathbf{r}_1,\mathbf{r}_2) = e^2(4\pi\,|\mathbf{r}_1-\mathbf{r}_2|)^{-1}$ is the Coulomb interaction. In the above equation, x is the combined space and spin variables $x = (\mathbf{r},\sigma)$. For the most part of this thesis, the spin dependence of most quantities will be implicit.

For the following derivation, we introduce an external potential $\Phi(x,x';t)$ which is local in time but nonlocal in space. We write it in the form of an interaction Hamiltonian :

$$\hat{H}'(t) = \int dxdx'\hat{\psi}^\dagger(x)\Phi(x,x';t)\hat{\psi}(x') \tag{2.23}$$

In our case, this external perturbation will be set to 0 at the end of the calculation. It is a formal tool to derive the useful equations for the time-evolution of Green's functions. With this Hamiltonian, it is especially relevant to introduce the *interaction picture*, in which both the operators and the wavefunctions have a time dependence.[38] For the field operators we have :

$$\hat{\psi}(1) \equiv \hat{\psi}(x_1,t_1) = e^{i\hat{H}t_1}\hat{\psi}(x_1)e^{-i\hat{H}t_1} \tag{2.24}$$

where we introduce the notation $1 \equiv (x_1, t_1)$. For the interaction Hamiltonian we have :

$$\hat{H}_I'(t) = e^{i\hat{H}t}\hat{H}'(t)e^{-i\hat{H}t} = \int dxdx'\hat{\psi}^\dagger(x,t^+)\Phi(x,x';t)\hat{\psi}(x',t) \tag{2.25}$$

where we use the notation t^+ for $t+\delta$ with $\delta \rightarrow 0^+$. We define a time-evolution operator in terms of this interaction Hamiltonian :

$$\hat{S} = \exp\left\{-i\int_{-\infty}^{+\infty} dt\hat{H}_I'(t)\right\} \tag{2.26}$$

We now write the definitions of single- and two-particle Green's functions that include the dependence in Φ :

$$G(1,2) = -i\frac{\langle N|\,\hat{T}\left[\hat{S}\hat{\psi}(1)\hat{\psi}^\dagger(2)\right]|N\rangle}{\langle N|\,T[\hat{S}]\,|N\rangle} \tag{2.27}$$

and

$$G_2(1,2:1',2') = (-i)^2\frac{\langle N|\,\hat{T}\left[\hat{S}\hat{\psi}(1)\hat{\psi}(2)\hat{\psi}^\dagger(2')\hat{\psi}^\dagger(1')\right]|N\rangle}{\langle N|\,T[\hat{S}]\,|N\rangle} \tag{2.28}$$

where $|N\rangle$ is the exact ground state of the N-electron system and T is a time-ordering operator. It ensures that the time variable increases from right to left. It gives $\hat{T}\left[\hat{\psi}(\mathbf{r}_1t_1)\hat{\psi}^\dagger(\mathbf{r}_2t_2)\right]$ $= \theta(t_1-t_2)\hat{\psi}(\mathbf{r}_1t_1)\hat{\psi}^\dagger(\mathbf{r}_2t_2) - \theta(t_2-t_1)\hat{\psi}^\dagger(\mathbf{r}_2t_2)\hat{\psi}(\mathbf{r}_1t_1)$, where θ is the Heaviside function.[68] The physical meaning of the one-body Green's function is the probability amplitude that an electron added in the system at time t_2 and position $\mathbf{r}_2$ propagates to position $\mathbf{r}_1$ and time t_1. In the time-ordered formalism that we are using, it is also the probability amplitude that a hole created at time t_1 and position $\mathbf{r}_1$ propagates to $(\mathbf{r}_2, t_2)$, depending on how the two time variables are ordered. The two-particle Green's function G_2 describes the propagation of two correlated particles. Depending on the time ordering, it can describe a propagation electron-electron pair, a hole-hole pair or an electron-hole pair. It will become useful in a following section.

We will now sketch a derivation for the equations of motion of the single-particle Green's function. To do this, we will make explicit the time dependence of each term in Eq. (2.27). We start with the time evolution of the quantity $\hat{T}[\hat{S}]$ appearing in the denominator of Eq. (2.27). For this we define the time evolution operator from Eq. (2.26) in the interaction picture, from time t_a to t_b :

$$\hat{S}(t_a,t_b) = \exp\left\{-i\int_{t_a}^{t_b} dt\hat{H}_I'(t)\right\} \tag{2.29}$$

Now the time derivatives of $\hat{T}[\hat{S}]$ are:

$$\begin{aligned}\frac{\partial}{\partial t_a}T[\hat{S}(t_a,t_b)] &= -i\hat{H}_I'(t_a)T[\hat{S}(t_a,t_b)]\\ \frac{\partial}{\partial t_b}T[\hat{S}(t_a,t_b)] &= iT[\hat{S}(t_a,t_b)]\hat{H}_I'(t_b)\end{aligned} \tag{2.30}$$

For the field operators, the derivation of the equations of motions can be found in Appendix A. They read :

$$\begin{aligned}\frac{\partial}{\partial t_1}\hat{\psi}(1) &= -i\left[h(1)+\int d3 v(1,3)\hat{\psi}^\dagger(3)\hat{\psi}(3)\right]\hat{\psi}(1)\\ \frac{\partial}{\partial t_2}\hat{\psi}^\dagger(2) &= i\left[\hat{\psi}^\dagger(2)h(2)+\hat{\psi}^\dagger(2)\int d3 v(2,3)\hat{\psi}^\dagger(3)\hat{\psi}(3)\right]\end{aligned} \tag{2.31}$$

where we introduced $v(1,2) = v(\mathbf{r}_1,\mathbf{r}_1)\delta(t_1-t_2)$ and $h(1) = h(\mathbf{r}_1)$. Knowing that the derivative of the Heaviside function is a Dirac delta, we can write the equations of motion for the single-particle Green's functions :

$$\begin{aligned}&\left[i\frac{\partial}{\partial t_1}-h(1)\right]G_1(1,2)-\int d3\Phi(1,3)G_1(3,2)+i\int d3 v(1,3)G_2(1,3^+;2,3^{++}) = \delta(1,2)\\ &\left[-i\frac{\partial}{\partial t_2}-h(2)\right]G_1(1,2)-\int d3G_1(1,3)\Phi(3,2)+i\int d3 v(2,3)G_2(1,3^{--};2,3^-) = \delta(1,2)\end{aligned} \tag{2.32}$$

with the notations :

$$\Phi(1,2) = \Phi(x_1,x_2;t_1)\delta(t_1-t_2). \tag{2.33}$$

and

$$1^+ = (r_1,t_1^+) \text{ where } t_1^+ = \lim_{\eta\to 0} t_1+\eta, \qquad \eta > 0 \tag{2.34}$$

and equivalently for 1^{++}. 1^- and 1^{--} follow from a change of sign. Here we notice that the equations for the single-particle Green's function depend on the two-particle Green's function. The latter could be expressed in terms of the three-body Green's function, and so on. Instead of using a hierarchy of higher-order Green's function, we will eliminate the two-particle Green's function from the equation and write a set of coupled integro-differential equations containing the self-energy and other useful quantities.

We use the functional derivative identity, derived for example in Ref. [65] :

$$G_2(1,3;2,3^+) = G(1,2)G(3,3^+)-\frac{\delta G(1,2)}{\delta\Phi(3)} \tag{2.35}$$

where we consider the external potential to be local in space $\Phi(x_1,x_2;t_1) = \Phi(x_1,t_1)\delta(x_1,x_2)$. This restriction is enough to generate the equations of motion for the single-particle Green's function. For the two-particle ones instead, one needs to consider the more general form of the external potential, non-local in space. The equations of motion become :

$$\left[i\frac{\partial}{\partial t_1} - h(1) - \Phi(1) + i\int d3 v(1,3)G(3,3^+)\right] G(1,2) - i\int d3 v(1^+,3)\frac{\delta G(1,2)}{\delta\Phi(3)} = \delta(1,2) \quad (2.36)$$

and

$$\left[i\frac{\partial}{\partial t_2} - h(2) - \Phi(2) + i\int d3 v(2,3)G(3^-,3)\right] G(1,2) - i\int d3 v(2^-,3)\frac{\delta G(1,2)}{\delta\Phi(3)} = \delta(1,2) \quad (2.37)$$

We cannot take the limit $\Phi \to 0$ yet because it would require the knowledge of the functional dependence of G on Φ. However Hedin proposed a way to rewrite the equations of motion (or at least one of them and the other would undergo the same process) by introducing new physical quantities, coupled in nonlinear self-consistent equations.[36]

The first of these quantities is the **total classical potential** V :

$$V_{\text{tot}}(1) \equiv \int d2 v(12)\langle\hat{n}(2)\rangle + \Phi(1) \quad (2.38)$$

where $\hat{n}$ is the density operator. It is the total potential felt by the electrons. It is local as is it the sum of the external perturbation and the Hartree potential. The equation of motion for the Green's function is then :

$$\left[i\frac{\partial}{\partial t_1} + \frac{1}{2}\nabla^2(1) - V_{\text{tot}}(1) - i\int d3 v(1^+,3)\frac{\delta}{\delta\Phi(3)}\right] G(1,2) = \delta(1,2) \quad (2.39)$$

To get rid of the functional derivative with respect to the external perturbation, we make use of the definition of the inverse Green's function and of the functional differentiation of a product:

$$\frac{\delta G(1,2)}{\delta\Phi(3)} = -\int d45 G(1,4)\frac{\delta G^{-1}(4,5)}{\delta\Phi(3)}G(5,2) \quad (2.40)$$

where the inverse single-particle Green's function is defined as :

$$\int d3 G^{-1}(1,3)G(3,2) = \int d3 G(1,3)G^{-1}(3,2) = \delta(1,2) \quad (2.41)$$

We now use the chain rule for functional differentiation :

$$\frac{\delta G^{-1}(4,5)}{\delta\Phi(3)} = \int d6 \frac{\delta G^{-1}(4,5)}{\delta V_{\text{tot}}(6)}\frac{\delta V_{\text{tot}}(6)}{\delta\Phi(3)} \quad (2.42)$$

We introduce the **scalar vertex function**, a three-point quantity defined as :

$$\Gamma(1,2;3) \equiv -\frac{\delta G^{-1}(1,2)}{\delta V_{\text{tot}}(3)} \tag{2.43}$$

We introduce the **inverse dielectric matrix** ε^{-1} :

$$\varepsilon^{-1}(1,2) = \frac{\delta V_{\text{tot}}(1)}{\delta \Phi(2)}. \tag{2.44}$$

It is the many-body formulation of the classical (inverse) dielectric matrix. We introduce the **dynamically screened interaction** W or screened Coulomb interaction, defined as :

$$W(1,2) \equiv \int d3 \varepsilon^{-1}(1,3) v(3,2) \equiv \int d3 v(1,3) \varepsilon^{-1}(2,3) \tag{2.45}$$

Note that the screened interaction is symmetric under the exchange of indices $W(1,2) = W(2,1)$. Finally, we introduce the **electron self-energy**, defined as :

$$\Sigma(1,2) = i \int d34 G(1,3) \Gamma(3,2;4) W(4,1^+) \tag{2.46}$$

With these quantities, we can rewrite the equation of motion for the single-particle Green's function :

$$\left[i\frac{\partial}{\partial t_1} + \frac{1}{2}\nabla^2(1) - V_{\text{tot}}(1) \right] G(1,2) - \int d3 \Sigma(1,3) G(3,2) = \delta(1,2) \tag{2.47}$$

We can see here that the self-energy Σ has the meaning of a non-local and energy-dependent effective single-particle potential.

Using Eqs. (2.43) and (2.47), we can express the vertex function in terms of the above quantities.

$$\Gamma(1,2;3) = \delta(1,2)\delta(1,3) + \int d4567 \frac{\delta \Sigma(1,2)}{\delta G(4,5)} G(4,6) G(7,5) \Gamma(6,7;3). \tag{2.48}$$

More details about these quantities and their derivations can be found for example in Strinati's review. [65] The previous quantities form a set of coupled integro-differential equations. In order to close the loop and build a self-consistent set, we need to write the relations between W and the other quantities. By combining V_{tot}, ε^{-1} and W, we get :

$$W(1,2) = v(1,2) + \int d34 v(1,3) \frac{\delta \langle \hat{n}(3) \rangle}{\delta V_{\text{tot}}(4)} W(4,2) \tag{2.49}$$

We define the **irreducible polarizability** to be :

$$\tilde{\chi}(1,2) \equiv \frac{\delta\langle\hat{n}(1)\rangle}{\delta V_{\text{tot}}(2)}. \tag{2.50}$$

It is the response of the density under the action of the total classical potential. This term is often called P in the GW literature. The reducible polarizability is instead the derivative of the density with respect to the perturbation Φ :

$$\begin{aligned}\chi(1,2) &\equiv \frac{\delta\langle\hat{n}(1)\rangle}{\delta\Phi(2)}\\ &= \int d3 \frac{\delta n(1)}{\delta V_{\text{tot}}(3)}\frac{\delta V_{\text{tot}}(3)}{\delta\Phi(2)} = \int d3\tilde{\chi}(1,3)\varepsilon^{-1}(3,2) = \tilde{\chi}(1,2) + \int d34\tilde{\chi}(1,3)v(3,4)\chi(4,2)\end{aligned} \tag{2.51}$$

With the following relation

$$n(1) = \langle\hat{n}(1)\rangle = -iG(1,1+), \tag{2.52}$$

and using properties of the inverse Green's function and the chain rule, one can write :

$$\begin{aligned}\tilde{\chi}(1,2) &= -i\frac{\delta G(1,1+)}{\delta V_{\text{tot}}(2)} = i\int d34G(1,3)\frac{\delta G^{-1}(3,4)}{\delta V_{\text{tot}}(2)}G(4,1^+)\\ &= -i\int d34G(1,3)G(4,1^+)\Gamma(3,4;2)\end{aligned} \tag{2.53}$$

Then we can write the screened interaction in term of $\tilde{\chi}$:

$$W(1,2) = v(1,2) + \int d34v(1,3)\tilde{\chi}(3,4)W(4,2) \tag{2.54}$$

as well as the dielectric matrix :

$$\epsilon(1,2) = \delta(1,2) - \int d3v(1,3)\tilde{\chi}(3,2) \tag{2.55}$$

Note that we can also express the *inverse* dielectric matrix in terms of the reducible polarizability from Eq. (2.51) :

$$\epsilon^{-1}(1,2) = \delta(1,2) + \int d3v(1,3)\chi(3,2) \tag{2.56}$$

where both quantities satisfy :

$$\int d3\epsilon^{-1}(1,3)\epsilon(3,2) = \int d3\epsilon(1,3)\epsilon^{-1}(3,2) = \delta(1,2). \tag{2.57}$$

We now have a set of coupled self-consistent equations, where the limit $\Phi \to 0$ can be taken.

2.3.2. Dyson equation

In order to be able to compute the Green's function and the related useful quantities, we need to reformulate the problem using the non-interacting Green's function G_0. We start by separating the part which comes only from the one-particle operators in the equation of motion Eq. (2.47) :

$$\left[i\frac{\partial}{\partial t_1} - h(1)\right] G_0(1,2) = \delta(1,2) \tag{2.58}$$

This is the definition of the non-interacting Green's function G_0. Using its inverse G_0^{-1}, which obeys the same relation as the full single-particle Green's function in Eq. (2.41), we can rewrite the interacting Green's function as :

$$G(1,2) = \int d34 G_0(1,4) G_0^{-1}(4,3) G(3,2) \tag{2.59}$$

Inserting the above equation in Eq. (2.47), we get :

$$\int d3 \left[G_0^{-1}(1,3) - \Sigma(1,3)\right] G(3,2) = \delta(1,2). \tag{2.60}$$

After multiplying from the left by $\int d1 G_0(4,1)$ we obtain :

$$G(1,2) = G_0(1,2) + \int d34 G_0(1,3)\Sigma(3,4)G(4,2) \tag{2.61}$$

or equivalently,

$$G^{-1}(1,2) = G_0^{-1}(1,2) - \Sigma(1,2) \tag{2.62}$$

Equation (2.61) is called the *Dyson equation* for the single-particle Green's function. Knowing G_0, which is numerically simple to compute, and approximating the self-energy Σ, which we will discuss later, allows one to compute the Green's function G. At this point it is useful to rewrite the self-energy as a sum of two terms $\Sigma = v_H + \Sigma_{xc}$, which are the Hartree potential and the exchange-correlation self-energy, repectively. Formally, it writes :

$$\Sigma(1,2) = v_H(1,2) - i \int d34 v(1,4) G(1,3) \left[\frac{\delta G^{-1}(3,2)}{\delta \Phi(4^+)}\right]. \tag{2.63}$$

With the Dyson equation for the Green's function, we can now complete the set of self-consistent, coupled equations that are called the *Hedin's equations* [36]:

$$\boxed{\begin{aligned}
&\Sigma(1,2) = i\int d34G(1,3)\Gamma(3,2;4)W(4,1^+)\\
&G(1,2) = G_0(1,2) + \int d34G_0(1,3)\Sigma(3,4)G(4,2)\\
&\Gamma(1,2;3) = \delta(1,2)\delta(1,3) + \int d4567\frac{\delta\Sigma(1,2)}{\delta G(4,5)}G(4,6)G(7,5)\Gamma(6,7;3)\\
&\tilde{\chi}(1,2) = -i\int d34G(1,3)G(4,1^+)\Gamma(3,4;2)\\
&W(1,2) = v(1,2) + \int d34v(1,3)\tilde{\chi}(3,4)W(4,2)
\end{aligned}}$$

Γ and W also satisfy Dyson equations, just as G. This is an exact set of coupled equations, that is solved self-consistently. The complexity to solve this set of equation comes from the vertex function Γ, which is a function of three points. Approximating Γ in the polarizability yields the Random Phase Approximation (RPA). Approximating it in the self-energy gives the GW Approximation (GWA). We present these two in the following.

2.3.3. The Random Phase Approximation

The RPA consists in neglecting the vertex corrections in the formula of the reducible polarizability Eq. (2.53). The vertex function reduces to

$$\Gamma(1,2;3) \approx \delta(1,2)\delta(1,3). \tag{2.64}$$

Then the irreducible polarizability writes :

$$\tilde{\chi}(1,2) \approx \tilde{\chi}_0(1,2) \equiv -iG(1,2^+)G(2,1^+) \tag{2.65}$$

Working out the above expression, one can see that it is made of non-interacting electron-hole pairs. The full polarizability follows from Eq. (2.51) :

$$\chi(1,2) = \tilde{\chi}_0(1,2) + \int d34\tilde{\chi}_0(1,3)v(3,4)\chi(4,2) = \int d3\tilde{\chi}_0(1,3)\left[1 - v\tilde{\chi}_0\right]^{-1}(3,2) \tag{2.66}$$

When we calculate $\tilde{\chi}_0$ from the single-particle Green's function as in Eq. (2.65), the derivative with respect to the perturbation is neglected. In this regard, $\tilde{\chi}_0$ is not an RPA response function. We call it the independent particle response function while $\tilde{\chi}$ is called the RPA response function, for historical reasons. However, $\tilde{\chi}_0$ will be useful when dealing with optical properties. Overall, the RPA gives a simplified means to compute the response functions and screening of the system.

2.3.4. The GW approximation

To calculate properties of the correlated N-electron system, the Hedin's equations are a great tool but are unsolvable in practice. One has to chose a starting approximation for the self-energy, which contains the summation to all orders in the interaction expansion of G. One way to approximate the self-energy is to consider $\frac{\delta\Sigma(12)}{\delta G(4,5)} = 0$ so that $\Gamma = \delta(1,2)\delta(1,3)$, just as for the RPA, and we obtain :

$$\Sigma_{xc}(1,2) = iG(1,2)W(1,2). \tag{2.67}$$

This is the so-called GW approximation, which gives good results for weakly-correlated materials.[37] It is the first-order in the expansion of the self-energy in terms of the interaction W. All higher order terms that are involved in electronic correlations are neglected. Part of those can be included by recomputing G self-consistently with the Hedin's equations. However in practice, it is not guaranteed that it leads to better results. The GW method is commonly used as a one-shot calculation starting from the DFT Kohn-Sham eigenvalues and wave functions. This is referred to as the $\mathrm{G_0W_0}$ approximation. Instead one can iterate the Hedin's cycle in the GWA but calculating only the change in the poles of G. This is referred to as the self-consistent eigenvalue GW, or evGW. We will use both in the body of this thesis.

Eq. (2.67) resembles the Hartree-Fock approximation, where the exchange part of the self-energy is written as $\Sigma_x^{HF}(1,2) = iG(1,2^+)v(1,2)$. The difference in this case is that we used the dynamically screened interaction instead of the bare Coulomb one.

2.3.5. Quasiparticle equations

Once the limit $\Phi \to 0$ is taken, there is no time-dependent potential acting on the system of N electrons. Hence, the system is invariant under time translation and the Green's function depends only on the time difference $\tau = t_1 - t_2$. One can do the Fourier transform from time τ to frequency ω, and we can write the Green's function in the so-called Lehmann representation :

$$G(x_1, x_2; \omega) = \sum_a \frac{f_a(x_1) f_a^*(x_2)}{\omega - \epsilon_a + i\eta} + \sum_i \frac{f_i(x_1) f_i^*(x_2)}{\omega - \epsilon_i + i\eta} \tag{2.68}$$

where a, i denote electron states, $f_a(x) = \langle N | \hat{\psi}(x) | N+1, a \rangle$ and $f_i(x) = \langle N-1, i | \hat{\psi}(x) | N \rangle$ are the Lehmann amplitudes (also called Dyson orbitals). They are defined with the N-electron ground state $|N\rangle$ whose total energy is E_N, the electron state number a of the $(N+1)$-electron system $|N+1, a\rangle$ with total energy $E_{N+1,a}$ and the electron-state number i of the $(N-1)$-electron system $|N-1, i\rangle$ with total energy $E_{N-1,i}$. The Lehmann representation of the Green's function also contains the quasiparticle energies, which are defined as $\epsilon_a = E_{N+1,a} - E_N = -A_a$ and $\epsilon_i = E_N - E_{N-1,i} = -I_i$. A_a and I_i are the electron affinities and ionization energies. This highlights the link between the poles of the Green's function from many-body

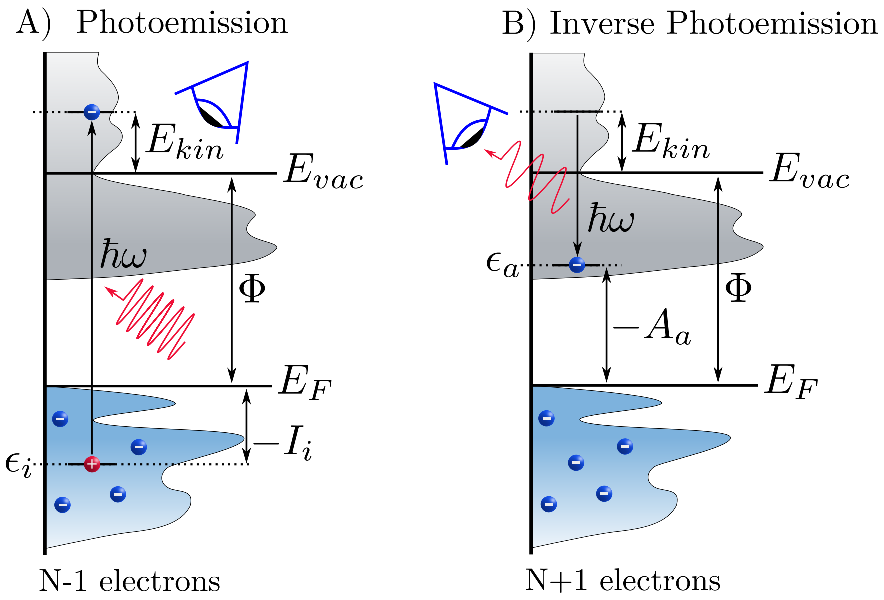

Figure 2.2. – Sketches of A) the photoemission spectroscopy , where the kinetic energy of the extracted electron is measured, B) Inverse photoemission spectroscopy, where the emitted light coming from the de-excitation of the added electron is measured. E_F is the Fermi level, E_{vac} is the vacuum level, E_{kin} is the kinetic energy of the added or removed electron, Φ is the extraction energy.

perturbation theory and the photoemission spectroscopy (PES) and inverse photoemission spectroscopy (IPES), and is illustrated in Fig. 2.2. In PES, the ionization energy writes $I_i = -\epsilon_i = \hbar\omega - E_{kin} - \Phi$ for $\epsilon_i < E_F$ where Φ is the extraction energy to send an electron above the vacuum energy E_{vac} with a kinetic energy E_{kin}, thanks to an irradiation of energy $\hbar\omega$. In IPES, the electronic affinity writes $-A_a = \epsilon_a = E_{kin} - \hbar\omega + \Phi$, for $\epsilon_a \geq E_F$, with E_F being the Fermi level.

With this form of the Green's function we can reformulate the Dyson equation from Eq. (2.61). Just as the Green's function, the self-energy depends only on the time difference $\tau = t_1 - t_2$. We can then take the Fourier transform of Eq. (2.47) :

$$[\omega - h(\mathbf{r}_1)]\, G(x_1, x_2; \omega) - \int dx_3 \Sigma(x_1, x_2; \omega) G(x_3, x_2; \omega) = \delta(x_1, x_2) \qquad (2.69)$$

Inserting the Lehmann representation of $G(x_1, x_2; \omega)$, one can select the term corresponding to a given pole ϵ_n by multiplying the equation by $\omega - \epsilon_n$ and taking the limit $\omega \to \epsilon_n$, giving :

$$[\epsilon_n - h(\mathbf{r}_1)]\, f_n(x_1) f_n^*(x_2) - \int dx_3 \Sigma(x_1, x_3; \epsilon_n) f_n(x_3) = \epsilon_n f_n(x_1) \qquad (2.70)$$

and we obtain an eigenvalue equation :

$$h(\mathbf{r}_1)f_n(x_1) + \int dx_3\Sigma(x_1, x_3; \epsilon_n)f_n(x_3) = \epsilon_n f_n(x_1) \tag{2.71}$$

These are the *quasiparticle equations*. They give the quasiparticle energies and the Lehmann amplitudes, or also called the Dyson orbitals. The quasiparticle energies are in general complex, and the Lehmann amplitudes, which act as the quasiparticles wavefunctions, are not orthogonal because Σ is energy-dependent and non Hermitian. The physical meaning of the poles of G is therefore the exact excitation energies of the $N \pm 1$ electrons. In an infinite, periodic system, the poles form a branch cut, and we can interpret the excitation spectrum in terms of quasiparticles with energies $\operatorname{Re}\epsilon_n$ and life-times $1/\operatorname{Im}\epsilon_n$ Here it is again made apparent that Σ is a non-local, energy-dependent single-particle effective potential. One thing to notice is also the fact that the quasiparticle energy is made out of the bare, independent single particle, and another term coming from the interaction with surrounding particle. The quasiparticle is the bare particle "dressed" with the interaction. This is a formulation in the Green's functions formalism of the quasiparticle concept, which was first introduced by Landau in the theory of Fermi liquids.[69] Since Σ is frequency-dependent, so are the quasiparticle energies. To solve this in practice, we linearize the self-energy around the independent particle energies computed in DFT and get :

$$\epsilon_n = \epsilon_n^{KS} + Z_n \operatorname{Re}\Sigma(\epsilon_n^{KS}) \tag{2.72}$$

where ϵ_n^{KS} are Kohn-Sham eigenvalues and the renormalization factor Z is defined as :

$$Z_n \equiv \left[1 - \left.\frac{\partial\Sigma(\omega)}{\partial\omega}\right|_{\omega=\epsilon_n}\right]^{-1} \tag{2.73}$$

It is a measure of the single-particle character of the system. If $Z = 1$, there is no correlation effects and the electron addition or removal spectra (given by $\operatorname{Im}G$) shows a single peak at the quasiparticle energy. The life-time of the single-particle state is infinite. For weakly correlated system, we have typically $Z \lesssim 1$. In this case, the intensity of the quasiparticle peak is renormalized by Z, and the amount missing is transferred to secondary peaks called satellites. In the GW approximation, only one satellite is present and its maximum is usually not at the correct position when compared with experiments.[70] This is due to the approximations done in the derivation of the GW self-energy. Finally if $Z \ll 1$, it means that the material is not well described by a single-particle scheme, for example because of strong correlations. In this case, Many Body Perturbation Theory is not well suited to describe such materials and a non-perturbative approach is required.

2.3.6. The Bethe-Salpeter equation

The GW approximation allows us to compute the quasiparticle energies *via* the addition or removal of one particle. These excitations are called charged. Instead, optical excitations in semiconductors are called neutral excitations, where an electron is promoted to a conduction band but stays in the crystal, leaving a hole in a valence band. In order to have a good description of these phenomena, we need to consider the interaction between the excited electron and the hole. In principle, this interaction is included in the vertex function Γ from Eq. (2.48). However, we have neglected it in the GW approximation. In this section, we will see how to include the electron-hole interaction from the two-particle Green's function. Doing this will include the electron-hole interaction only in the response function, where it is known to have very important contributions, and not in the single particle Green's function where its contribution is less important. [71] We will also see how we can change the formulation of the problem from particles in bands to a new type of quasiparticle : the *exciton*, which is a bound electron-hole pair.

Dyson equation for the two-particle propagator L

We start by writing a Dyson equation for the two-particle Green's function, defined in Eq. (2.28). We define the two-particle correlation function or propagator L :

$$L(1,2,1',2') = -G_2(1,2,1',2') + G(1,1')G(2,2') \tag{2.74}$$

It contains the correlated propagation of a particle and a hole which is the first term, and the second term removes the uncorrelated propagation of the two. Depending on the time-ordering of the field operators in the definitions of G and G_2, one can have different combinations for the two particles, for instance hole-hole, electron-electron *etc*. By using the identity in Eq. (2.35), with a fully non-local external potential $\Phi(2',2)$, we can also write :

$$L(1,2,1',2') = \frac{\delta G(1,1')}{\delta \Phi(2',2)} = -\int d33' G(1,3)\frac{\delta G^{-1}(3,3')}{\delta \Phi(2',2)}G(3',1') \tag{2.75}$$

After computing the functional derivative of the inverse Green's function, we get :

$$L(1,2,1',2') = G(1,2')G(2,1') + \int d33' G(1,3)\frac{\delta \Sigma(3,3')}{\delta \Phi(2',2)}G(3',1') \tag{2.76}$$

with $\Sigma = v_H + \Sigma_{xc}$. One can take the limit $\Phi \to 0$ in the above equation to obtain the equilibrium solution. The first term in Eq. (2.76) is defined as the propagator for two independent particles :

$$L_0(1,2,1',2') = G(1,2')G(2,1') \tag{2.77}$$

We can use the chain rule for the functional derivative of Σ to express it with respect to G. Now if we define the two-particle interaction Ξ as :

$$\Xi(3,2,3',2') \equiv -i\delta(3,3')\delta(2'^{+},2)v(3^{+},2) + \frac{\delta\Sigma_{xc}(3,3')}{\delta G(2',2)} \tag{2.78}$$

we see that it is made out of two terms. When G changes under the action of Φ, the variation of the Hartree potential v_H gives the first term, and the second term comes from the variation of Σ_{xc}. This two-particle interaction is a measure of how the internal potentials (both local and non-local) of the system vary under the action of the external non-local perturbation Φ. Finally we obtain the **Bethe-Salpeter equation** (BSE):

$$L(1,2,1',2') = L_0(1,2,1',2') + \int d3'3d44' L_0(1,3',1',3)\Xi(3,4,3',4')L(4',2,4,2') \tag{2.79}$$

which is a Dyson equation for the two-particle propagator L. The two-particle interaction quantity Ξ is called the *kernel*. It contains two terms we can separate and hence break the BSE into the so-called irreducible contribution, that does not contain the derivative of the Hartree potential v_H :

$$\tilde{L}(1,2,1',2') = L_0(1,2,1',2') + \int d33'd44' L_0(1,3',1',3)\frac{\delta\Sigma_{xc}(3,3')}{\delta G(2',2)}L(4',2,4,2') \tag{2.80}$$

and

$$L(1,2,1',2') = \tilde{L}(1,2,1',2') - i\int d34\tilde{L}(1,3,1',3)v(3^{+},4)L(4,2,4^{+},2') \tag{2.81}$$

Now, from the first identity in Eq. (2.74), we have that L is the variation of G under the action of a non-local potential Φ. If we define $v_H(2',2) \equiv \delta(2',2)v_H(2)$, then we can extend the total classical potential V_{tot} from Eq. (2.38) to be non-local, and we can express the irreducible two-particle propagator as :

$$\tilde{L}(1,2,1',2') = \frac{\delta G(1,1')}{\delta V_{\text{tot}}(2',2)} \tag{2.82}$$

With this equation, we can notice the similarity with Eq. (2.50), where the density is replaced by the Green's function and the total classical potential is non-local. In fact, the irreducible two-particle propagator $\tilde{L}$ is a generalization of the irreducible polarizability to four points. We have the relation :

$$-i\tilde{L}(1,2,1^{+},2^{+}) = \tilde{\chi}(1,2) \tag{2.83}$$

The same relation exists for the full or reducible polarizability, which we call χ, and the reducible two-particle propagator :

$$\chi(1,2) = \frac{\delta n(1)}{\delta \Phi(2)} = -iL(1,2,1^+,2^+) \tag{2.84}$$

In the two above equations, the time-ordering is chosen so that the two-particle propagator (reducible or irreducible) describes the propagation of an electron-hole pair.

The Bethe-Salpeter equation in the GW approximation

In the same way we needed an approximation to compute the electron self-energy Σ, we need an approximation to be able to compute the kernel Ξ and hence the Dyson equation for L. The main difficulty in solving the BSE is that the kernel is a four-points quantity. In principle, the arguments are in spin-space-time coordinates. In the following, we will omit the spin dependence. The two-particle propagators depend on four times or three time differences, in the absence of a time-dependent Hamiltonian. We can do the Fourier transform of the BSE, which will therefore depend on three frequencies. If we consider only the simultaneous propagation of an electron and a hole, we obtain :

$$L(\omega_1,\omega_2) = L_0(\omega_1,\omega_2) + \int d\omega_3 d\omega_4 \frac{L_0(\omega_1,\omega_2,\omega_3)}{(2\pi)^2} \Xi(\omega_1,\omega_3,\omega_4) L(\omega_1,\omega_4) \tag{2.85}$$

For more details about this derivation and the relation between the Green's functions in frequency space, please refer to section 4 of Chapter 14 of Ref. [38]. We set ourselves in the GW approximation, which will simplify the calculation of the kernel Ξ. The exchange-correlation part reads :

$$\Xi_{xc}^{GWA}(1,2,3,4) = i\delta(1,4)\delta(2,3)W(1,2) + iG(1,3)\frac{\delta W(1,3)}{\delta G(4,2)} \tag{2.86}$$

The first term is at first order in W. The second term is the change in the screening when the system is perturbed, and contains higher orders in W. In accordance with the GW approximation, we also neglect here the second term in the above equation. In frequency space, we are left with :

$$\Xi_{xc}^{GWA}(\omega_1,\omega_2,\omega_3) \approx iW(\omega_2 - \omega_3) \tag{2.87}$$

Here we see that the coupling between two particles, which comes from the screened interaction, is frequency-dependent. It originates from the fact that the system needs time to adapt to the perturbation, which is the creation of the electron-hole pair. Another important approximation that we introduce here is that we consider the screened interaction to be static, *i.e.* frequency-independent : $W(\omega) \to W(0)$. In practice, we obtain L_0 with the single-particle Green's functions in the quasiparticle approximation in the dynamic GWA, and we use a static screening only for the kernel of the BSE. Reintroducing the space and (implicit) spin dependence, we finally obtain :

$$\begin{aligned} L(x_1, x_2, x_{1'}, x_{2'}; \omega) = & L_0(x_1, x_2, x_{1'}, x_{2'}; \omega) \\ & - i \int dx_3 dx_4 L_0(x_1, x_3, x_{1'}, x_3; \omega) v(x_3, x_4) L(x_4, x_2, x_4, x_{2'}; \omega) \\ & - L_0(x_1, x_4, x_{1'}, x_3; \omega) W(x_3, x_4) L(x_3, x_2, x_4, x_{2'}; \omega) \end{aligned} \tag{2.88}$$

The static screening approximation is necessary to obtain a two-particle propagator that depends only on one frequency. Hence we will be able to invert the BSE and to rewrite the problem into an excitonic Hamiltonian, as it is done in the paragraph below. However, previous works attempted to solve the BSE with a dynamic kernel, such as Refs. [42, 72]. Part of the results presented later in this thesis are obtained by adding a dynamical correction to the static BSE kernel.

Reformulation in a two-particle Schrödinger equation

The BSE derived in the previous section, Eq. (2.88), can be reformulated into a Schrödinger equation for two particles, which is easier to solve and will highlight the physics of the problem and make the *excitons* appear as emerging quasiparticles. In this section, we omit the dependence in the momenta for simplicity, but the generalization to finite momenta is possible.[73] Here we consider an independent-particle basis in which the non-interacting two-particle propagator L_0 is diagonal, and we assumed that we obtained the quasiparticle eigenvalues from the GWA. At $T = 0$, we can write :

$$L_{0\ n_1 n_2 n_3 n_4}(\omega) = L_{0\ n_1 n_3}^{n_4 n_2} = 2i \frac{(f_{n_1} - f_{n_2}) \delta_{n_1 n_4} \delta_{n_2 n_3}}{\omega - (\epsilon_1 - \epsilon_2) \pm i\eta} \tag{2.89}$$

where the n_i indices denote for the quasiparticle state with occupation number f_i and the factor 2 in the right-hand side stems from the summation on spin indices. The plus or minus sign in the denominator depends on the sign of the difference of the occupation factors f_i. In this basis, the BSE becomes :

$$L_{n_1 n_3}^{n_4 n_2} = \left[L_0^{-1} + \frac{i}{2} \Xi \right]_{n_1 n_3}^{-1\ n_4 n_2} = 2i \left[H^{2p} - \mathbb{I}(\omega \pm i\eta) \right]_{n_1 n_3}^{-1\ n_4 n_2} (f_{n_2} - f_{n_4}), \tag{2.90}$$

where $\mathbb{I}$ is the identity matrix and H^{2p} is the two-particle Hamiltonian

$$H^{2p\ n_4 n_2}_{n_1 n_3} = (\epsilon_{n_2} - \epsilon_{n_1}) \delta_{n_1 n_4} \delta_{n_2 n_3} + (f_{n_1} - f_{n_3}) \Xi_{n_1 n_3}^{n_4 n_2}. \tag{2.91}$$

The matrix elements of the kernel are :

$$\Xi_{n_1 n_3}^{n_4 n_2} = 2 v_{n_1 n_4}^{n_3 n_2} - W_{n_1 n_3}^{n_4 n_2} \tag{2.92}$$

In our derivation we consider a semiconductor or an insulator with well-separated valence and conduction bands. Therefore the difference of the occupation factors, at $T = 0$, in the above equations guarantees that only pairs of an occupied and an empty state are contributing in the interaction. We can use the indices v, c for valence and conduction states, respectively. Then

$$\Xi_{vc}^{v'c'} = 2v_{vv'}^{cc'} - W_{vc}^{v'c'} \tag{2.93}$$

The first term above is often referred to as electron-hole exchange and is repulsive. The second term is called the direct electron-hole interaction, and it is an attractive interaction between the electron and the hole that binds them in a pair. We can decompose the Hamiltonian into four blocks :

$$H^{2p} = \begin{pmatrix} H^{res} & H^{\text{coupl}} \\ -[H^{\text{coupl}}]^* & H^{ares} \end{pmatrix} \tag{2.94}$$

where the resonant part is

$$H^{res} \equiv H_{vc}^{2p\ v'c'} = (\epsilon_c - \epsilon_v)\delta_{vv'}\delta_{cc'} + \Xi_{vc}^{v'c'} \tag{2.95}$$

This subpart is hermitian and corresponds to transitions from the valence to the conduction band, with positive frequencies. The coupling part is :

$$H^{\text{coupl}} \equiv H_{vc}^{2p\ c'v'} = \Xi_{vc}^{c'v'} = [\Xi_{cv}^{v'c'}]^* \tag{2.96}$$

which is symmetric. The antiresonant part is :

$$H^{ares} \equiv H_{vc}^{2p\ c'v'} = (\epsilon_v - \epsilon_c)\delta_{vv'}\delta_{cc'} - \Xi_{cv}^{c'v'} = -[H^{res}]^* \tag{2.97}$$

The whole Hamiltonian H^{2p} is pseudo-hermitian, which means that its eigenvalues are always real. For the calculations in this thesis, we used the Tamm-Dancoff approximation, which consists in neglecting the coupling part of the Hamiltonian. It works best with bulk semiconductors and insulators, where the energy of the transitions is large compared to the interaction matrix elements in H^{coupl}. [74] With this approximation, we only consider transitions with positive energies for the resonant term, and the full Hamiltonian becomes hermitian. It also simplifies the solution of the BSE since we can calculate only the resonant term, and the antiresonant follows by taking its complex conjugate. In the Tamm-Dancoff approximation, we can build a two-particle Schrödinger equation :

$$\sum_{n_3 n_4} H_{n_1 n_2}^{2p\ n_3 n_4} A_\lambda^{n_3 n_4} = E_\lambda A_\lambda^{n_1 n_2} \tag{2.98}$$

where E_λ is the eigenenergy of the exciton λ. We change from the quasiparticle basis $\{n\}$ to the exciton basis $\{\lambda\}$ where we can write the exciton wave function as :

$$\Psi_\lambda(r_1, r_2) = \sum_{n_1 n_2} A_\lambda^{n_1 n_2} \psi_{n_1}^*(r_1)\psi_{n_2}(r_2) \tag{2.99}$$

where A_λ are the coefficients of the expansion in the exciton basis. We will see later that they are also related to the oscillator strength of the transitions. Finally we can write the two-particle propagator using these quantities :

$$L^{n_3 n_4}_{n_1 n_2}(\omega) = 2i \sum_{\lambda\lambda'} \frac{A^{n_1 n_2}_{\lambda}\, A^{*n_3 n_4}_{\lambda'}}{\omega - E_\lambda + i\eta} (f_{n_4} - f_{n_3}) \tag{2.100}$$

Each couple (nn') corresponds to a pair (vc) or (cv) of an occupied and an empty state. We remark that the exciton energies replaced the difference of quasiparticle energies $\epsilon_c - \epsilon_v$ in the denominator, which are the quasiparticle transition energies. The screened interaction contributes to the attraction between the electron and the hole, lowering the transition energy below the gap. The Coulomb interaction includes the local field effects, which have a significant contribution for inhomogeneous systems. Overall, the exciton energy will lie below the minimal quasiparticle transition energy, which is the energy of the gap. The difference between the transition energy and the quasiparticle gap is called the *exciton binding energy*. Excitonic effects can be extremely important in the optical properties of semiconductors, as we will see in the next section.

2.4. Optics

Optics experiments involve an external field interacting with the electronic density of the material. In the regime of low intensity field where we can describe it as a perturbation, the formalism presented above is a perfectly suited simulation tool. The key quantity to reproduce the results of these experiments is the electronic screening of the material, which is linked to the dielectric matrix and to the response function or polarizability χ. Pertubatively, the response of the electronic density with respect to an external field can be described in terms of the neutral excitations of the system, *i.e.* by the formation and propagation of electron-hole pairs. In optics experiments, the external fields have wavelength that are far larger than the characteristic length of the unit cells of the crystals we simulate. Typically, the wavelengths are in the visible or ultraviolet range, from 180 nm to 1200 nm, while the crystal unit cells are of the order of a few nm. In order to obtain optical spectra that are comparable to those measured experimentally, we need to average the microscopic variations in the response functions and related quantities we introduced so far. Hence we can obtain macroscopic quantities, which are the ones accessible in experiments.

To make the distinction between short-range, microscopic variations and long-range, macroscopic variations of the quantities of interest in a periodic and infinite crystal, it is easier to make use of the space Fourier transform and to work in reciprocal space. For a function f of two space variables and one frequency (or one time difference), its space

Fourier transform is :

$$f(\mathbf{r},\mathbf{r}';\omega)=\frac{1}{\Omega}\sum_{\mathbf{k}}^{BZ}\sum_{\mathbf{GG}'}\exp\{i(\mathbf{k}+\mathbf{G})\cdot\mathbf{r}\}f(\mathbf{k}+\mathbf{G},\mathbf{k}'+\mathbf{G}';\omega)\exp\{-i(\mathbf{k}+\mathbf{G}')\cdot\mathbf{r}'\} \tag{2.101}$$

where Ω is the volume of the crystal (more precisely of the Born-von Karmann supercell in the case of an infinite crystal), $\mathbf{k}$ is a Bloch wavevector confined to the first BZ and $\mathbf{G},\mathbf{G}'$ are reciprocal lattice vectors. With this definition, we can write the inverse dielectric matrix in reciprocal space :

$$\varepsilon^{-1}_{\mathbf{GG}'}(\mathbf{q};\omega)=\delta_{\mathbf{GG}'}+v(\mathbf{q}+\mathbf{G})\chi_{\mathbf{GG}'}(\mathbf{q};\omega) \tag{2.102}$$

where $\mathbf{q}$ is a vector in the first BZ. The Fourier transform of the Coulomb potential is $v(\mathbf{q}+\mathbf{G})=\frac{4\pi}{|\mathbf{q}+\mathbf{G}|^2}$. The matrix elements of the screened interaction W in reciprocal space are

$$W_{\mathbf{GG}'}(\mathbf{q};\omega)=\varepsilon^{-1}_{\mathbf{GG}'}(\mathbf{q};\omega)v(\mathbf{q}+\mathbf{G}')=v(\mathbf{q}+\mathbf{G})+v(\mathbf{q}+\mathbf{G})\chi_{\mathbf{GG}'}(\mathbf{q};\omega)v(\mathbf{q}+\mathbf{G}') \tag{2.103}$$

It is useful to make the separation between long-range and short-range terms in the Coulomb potential $v=v_0+\bar{v}$, where v_0 is the long-range component with $\mathbf{G}=0$ and $\bar{v}$ contains all the $G\neq 0$ components. We have

$$\begin{aligned}\bar{v}(\mathbf{G})&=0 &&\text{for } \mathbf{G}=0\\ \bar{v}(\mathbf{G})&=v(\mathbf{G}) &&\text{for } \mathbf{G}\neq 0,\end{aligned} \tag{2.104}$$

and we can define the corresponding polarizability, called the *proper* response function :

$$\bar{\chi}_{\mathbf{GG}'}(\mathbf{q},\omega)=\chi_{\mathbf{GG}'}(\mathbf{q},\omega)-\chi_{\mathbf{GG}'}(\mathbf{q},\omega)\bar{v}(\mathbf{q}+\mathbf{G})\bar{\chi}_{\mathbf{GG}'}(\mathbf{q},\omega) \tag{2.105}$$

Now if we use $\bar{v}$ instead of v in the Bethe-Salpeter kernel Ξ, we can compute the two-particle propagator without the long-range component of the Coulomb interaction, and we have the usual relationship :

$$\bar{\chi}(1,2)=-i\bar{L}(1,2,1^+,2^+) \tag{2.106}$$

$\bar{L}$ is the most commonly computed quantity for the calculation of optical spectra in the context of the BSE.[75]

The response function enters both reciprocal space expressions in Eqs. (2.102) and (2.103). Depending on which level of theory the electron-hole interaction is treated, its expression will be different and will lead to different spectra. Before writing its expression we need to define the matrix elements of pairs of orbitals, that we call generalized dipoles :

$$\rho_{v\mathbf{k}c\mathbf{k}+\mathbf{q}}(\mathbf{G})=\langle c\mathbf{k}+\mathbf{q}|\,e^{i(\mathbf{q}+\mathbf{G})\cdot\mathbf{r}}\,|v\mathbf{k}\rangle \tag{2.107}$$

where v,c denote for valence and conduction states. These matrix elements describe the transition from a valence state at $\mathbf{k}$ to a conduction state at $\mathbf{k}+\mathbf{q}$ mediated by an electric field with momentum $\mathbf{q}$. At this point we note that, for momentum conservation, the vector $\mathbf{q}$ which lies in the first BZ has to be equal to the difference of two crystal momenta $\mathbf{k}$.

For independent particles, the response function has the form $\chi^0 = -iG_0G_0$, where G_0 are non-interacting Green's functions. The first matrix element of this response function can be written :

$$\chi^0_{00}(\mathbf{q}\to 0,\omega) = 2\lim_{\mathbf{q}\to 0}\sum_{v c\mathbf{k}} \frac{\left|\rho_{v\mathbf{k}c\mathbf{k}+\mathbf{q}}\right|^2}{\omega - (\epsilon_{c\mathbf{k}+\mathbf{q}} - \epsilon_{v\mathbf{k}}) + i\eta} \tag{2.108}$$

This response function will give a spectrum with peaks at the independent-particle transition energies. Due to momentum conservation, only transitions with momentum transfer $\mathbf{q}$ between the hole in state $v\mathbf{k}$ and the electron in state $c\mathbf{k}+\mathbf{q}$ contribute.

To account properly for the electron-hole interaction, which is crucial to accurately simulate optical spectra, we can compute the response function at the BSE level The diagonalization of the two-particle Hamiltonian H^{2p} in Eq. (2.91) with $\bar{v}$ gives the excitonic eigenvectors $\bar{A}_\lambda$ (in the following, we will omit the bar for simplicity). Using this, the head of the response function matrix is :

$$\bar{\chi}_{00}(\mathbf{q}\to 0,\omega) = 2\lim_{\mathbf{q}\to 0}\sum_{\lambda} \frac{\left|\sum_{vc\mathbf{k}} \bar{A}_\lambda^{v\mathbf{k}c\mathbf{k}+\mathbf{q}}\rho_{v\mathbf{k}c\mathbf{k}+\mathbf{q}}\right|^2}{\omega - E_\lambda + i\eta} \tag{2.109}$$

Compared to Eq. (2.108), the transition energies are replaced by the excitonic energies, meaning the positions of the peaks will be changed with respect to independent-particle calculations. Also, the A_λ coefficients participate in the mixing of the dipole matrix elements,[75] which will give rise to different structures in the spectra.

2.4.1. Optical absorption

As mentioned at the start of this section, we need to relate the many-body quantities we compute with the ones measured experimentally. To this end, we first write the relation between the microscopic inverse dielectric function and the proper response function :

$$\frac{1}{\varepsilon^{-1}_{00}(\mathbf{q},\omega)} = 1 - v_0(\mathbf{q})\bar{\chi}_{00}(\mathbf{q},\omega) \tag{2.110}$$

where it should be understood that the 00 indices mean that we take the first component of the inverse, and not the inverse of the first component. We now define the *macroscopic* dielectric function as :

$$\varepsilon_M(\omega) \equiv \lim_{\mathbf{q}\to 0}\frac{1}{\varepsilon^{-1}_{00}(\mathbf{q},\omega)} \tag{2.111}$$

and using the relation from Eq. (2.110) :

$$\varepsilon_M(\omega) = 1 - \lim_{q\to 0} \frac{4\pi}{q^2}\bar{\chi}_{00}(\mathbf{q},\omega) \tag{2.112}$$

Taking the optical limit $\mathbf{q} \to 0$ is justified because the longitudinal external field carries a very small momentum with respect to the extent of the Brillouin Zone. This equation is well-behaved at the small-q limit because $\bar{\chi}_{00}$ has a q^2 dependence. Here we see the advantage of using the proper response function $\bar{\chi}$ because it gives us direct access to the macroscopic dielectric function without the need to average or to invert the microscopic one. The macroscopic dielectric function is a complex function $\varepsilon_M(\omega) = \varepsilon_1(\omega) + i\varepsilon_2(\omega)$ and the absorption spectrum will be given by its imaginary part. Let us express it in a computable way.

In the optical limit, we can expand the generalized dipoles from Eq. (2.107) to first order in $\mathbf{q}$, and the first non-zeo term is $\propto |i\mathbf{q}\cdot\langle c|\,\mathbf{r}-\mathbf{r}'\,|v\rangle|^2 = q^2\,|\hat{\mathbf{n}}\cdot\langle c|\,\mathbf{r}\,|v\rangle|^2$ where $\hat{\mathbf{n}}$ is the versor pointing in the direction of $\mathbf{q}$. We then define the *dipole matrix elements* as :

$$d_{cv\mathbf{k}} = \hat{\mathbf{n}}\cdot\langle c\mathbf{k}|\,\mathbf{r}\,|v\mathbf{k}\rangle \tag{2.113}$$

Now by making use of Eqs. (2.112) and (2.108), we can write the imaginary part of the macroscopic dielectric function in terms of the dipoles. For independent particles, it writes :

$$\varepsilon_2(\omega) = \frac{8\pi^2}{V}\sum_{cv\mathbf{k}} |d_{cv\mathbf{k}}|^2\,\delta(\omega - (\epsilon_{c\mathbf{k}} - \epsilon_{v\mathbf{k}})) \tag{2.114}$$

At the BSE level, the dipole matrix elements are replaced by their linear combination with exciton eigenvectors. Using Eq. (2.109), it gives :

$$\varepsilon_2(\omega) = \frac{8\pi^2}{V}\sum_{\lambda}\left|\sum_{cv\mathbf{k}} A_\lambda^{cv\mathbf{k}} d_{cv\mathbf{k}}\right|^2 \delta(\omega - E_\lambda) \tag{2.115}$$

As one can see in the delta functions of the two versions, the peaks are not given by the same excitations. Hence the spectra will exhibit different features, whether we consider independent particles or we include the electron-hole interaction with the BSE. This is illustrated in Fig. 2.3.

We now have access to another relevant quantity which is the *absorption coefficient* $\alpha(\omega)$:

$$\alpha(\omega) = \frac{\omega}{c}\frac{\varepsilon_2(\omega)}{n_1(\omega)} \tag{2.116}$$

It is the ratio of the imaginary part of the dielectric function and the real part of the refractive index which writes $n(\omega) = n_1(\omega) + in_2(\omega)$. The refractive index is obtained with $\varepsilon_M(\omega) = n^2(\omega)$ The absorption coefficient is completely determined by $\varepsilon_2(\omega)$ and it is the quantity that yields the absorption spectra that we compare to experiments.[16]

Moreover, we see that the absorption is proportional to the quantity $T^\lambda = \sum_{cv\mathbf{k}} A_\lambda^{cv\mathbf{k}} d_{cv\mathbf{k}}$

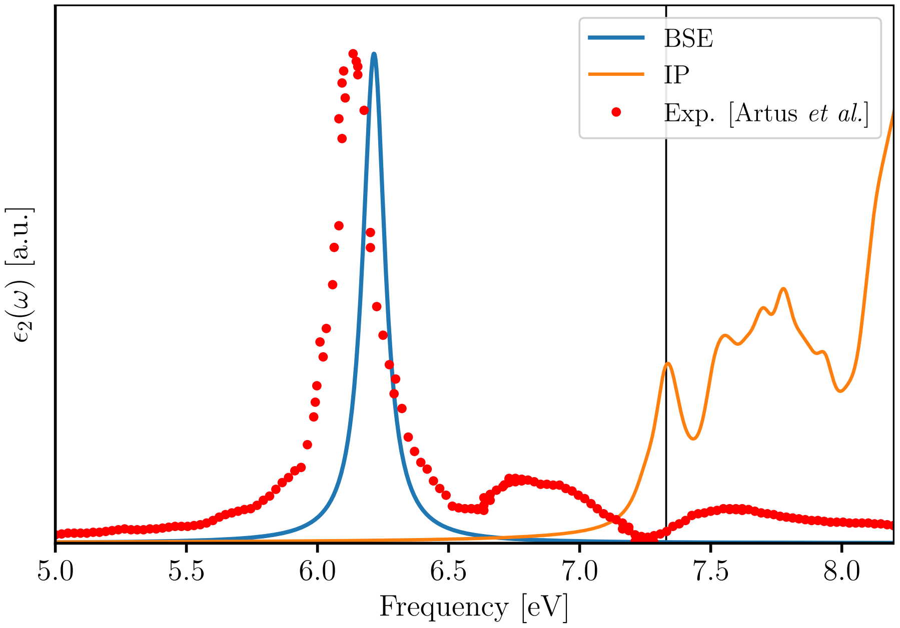

Figure 2.3. – Absorption spectrum of bulk hBN, computed at the independent particle level (orange) and at theBSE level (blue) of theory, compared to the experiment (red dots) of Ref. [30]. The vertical line is at the supposed gap energy. The orange curve watch shifted to match it. The inclusion of excitonic effects makes a striking difference from the independent particle level and gives a much better agreement with experiment, where peaks appear below the gap energy. Note that the blue curve is calculated to match only the first peak and all curves are normalized.

that we define as the *exciton dipole*, also known as exciton oscillator strength. Each exciton has a dipole associated to it. If the dipole is large, then peaks will be visible in the absorption spectra at the corresponding exciton energy. For this reason these excitons are called *bright*. Instead if the excitons have a dipole equal to zero, which can be the case for transitions forbidden by spin or momentum conservation, then the excitons are not visible in absorption and are called *dark*.

2.4.2. Luminescence

In general, luminescence is the spontaneous emission of light from an excited state of the material. Depending on how the system is excited, a prefix is added. For instance, if the system is excited by a laser, the process is called photoluminescence. It is called cathodoluminescence when the excitation is made by a beam of electrons, electroluminescence when an electric field is applied, an so on.[17]

Photoluminescence is the process that can be seen as the inverse of absorption : photoexcited carriers de-excite from the bottom of the conduction band to an empty state in the valence band by emitting light with a frequency corresponding to the gap energy. For direct semiconductors or insulators, considering that the light emission is the inverse process of the absorption is generally an acceptable approximation. In this case, the spectra for the two process should look identical [1]. However, for materials with indirect gaps, this simple picture does not hold anymore. Indeed, one needs to consider the phonon-assisted transitions, which give rise to phonon satellites in both the absorption and the luminescence spectra, as will be discussed later.

Here I will present an approximation to derive the spontaneous emission rate, which is the key quantity to compute luminescence spectra, for any kind of gapped material, starting from the absorption rate. We use the van Roosbroeck–Shockley relation, derived in 1954 to describe the light emission in Germanium [76] and follow Refs [29, 77]. This relation is based on a *steady-state* approximation, that is to say we consider the absorption rate and the spontaneous emission rate to be in detailed balance. We start by giving the relations for the case of independent particles and direct transitions only. For indirect transitions, the same kind of relations hold but they need to be slightly modified to include the phonon-assisted transitions, which will be done in the body of this thesis. Here we consider a quasi-equilibrium situation where excited electron and holes are relaxed at the band extrema after scattering with phonons, electrons or other relaxation processes. Hence we reach a quasi-equilibrium distribution of particles where some electrons have been removed from the top valence band and promoted in conductions bands. These electron and hole distributions are described by two Fermi-Dirac functions with two different chemical potentials (for a discussion see section 12.2.1 of Ref. [78]). The absorption rate is :

$$R^{abs}(\omega) = 2\pi\mathcal{K}(\omega)\frac{\mathcal{N}(\omega)}{N_k}\sum_{cv\mathbf{k}}|d_{cv\mathbf{k}}|^2\left[f_{v\mathbf{k}}(1-f_{c\mathbf{k}})-f_{c\mathbf{k}}(1-f_{v\mathbf{k}})\right]\delta(\epsilon_{c\mathbf{k}}-\epsilon_{v\mathbf{k}}-\omega) \tag{2.117}$$

where $f_{n\mathbf{k}} = \left[1+e^{\epsilon_{n\mathbf{k}}-\mu_{e/h}/k_BT}\right]^{-1}$ is the Fermi-Dirac occupation function for the state n at point $\mathbf{k}$, $\mu_{e/h}$ being the chemical potential for electrons or holes. $\mathcal{K}(\omega)$ is a dimensional factor depending on electromagnetic quantities. The rate of spontaneous emission writes :

$$R^{sp}(\omega) = 2\pi\mathcal{K}(\omega)\frac{\mathcal{G}(\omega)}{N_k}\sum_{cv\mathbf{k}}|d_{cv\mathbf{k}}|^2 f_{c\mathbf{k}}(1-f_{v\mathbf{k}})\delta(\epsilon_{c\mathbf{k}}-\epsilon_{v\mathbf{k}}-\omega) \tag{2.118}$$

These two expressions differ by the occupation functions of the electrons and holes, but also by the presence of the photon density of states $\mathcal{G}(\omega)$ in one and the photon density per unit energy $\mathcal{N}(\omega)$ in the other. The two are linked by the relation $\int\mathcal{N}(\omega)d\omega = \int\bar{\mathcal{N}}\mathcal{G}(\omega)d\omega$ where $\bar{\mathcal{N}}$ is the average photon number.
If we define the incoming photon flux as $\mathcal{F}(\omega) = \mathcal{N}(\omega)\frac{c}{n_1(\omega)}$, we can use the following relation :

$$R^{abs}(\omega) = \mathcal{F}(\omega)\alpha(\omega) \tag{2.119}$$

---

[1] In reality there are differences such as the Stokes shift, which is caused by the broadening of electronic states by phonons.

Finally, we can derive a Bose-Einstein type of occupation function by noticing that the following relation holds independently of which $(cv\mathbf{k})$ transition is considered :

$$\frac{f_{c\mathbf{k}}(1-f_{v\mathbf{k}})}{f_{v\mathbf{k}}(1-f_{c\mathbf{k}})-f_{c\mathbf{k}}(1-f_{v\mathbf{k}})} = \frac{1}{e^{\omega-(\mu_e-\mu_h)/k_BT}-1} \approx e^{-(\omega-\Delta\mu)/k_BT} \tag{2.120}$$

where in the last step we approximated the Bose-Einstein function with a Boltzmann distribution. Finally, by comparing the absorption and the spontaneous emission rates, we obtain :

$$\begin{aligned} R^{sp}(\omega) &= \frac{n_1(\omega)^2\omega^2}{\pi^2c^2}\,\alpha(\omega)\,e^{-(\omega-\Delta\mu)/k_BT} \\ &= \frac{n_1(\omega)\omega^3}{\pi^2c^3}\,\varepsilon_2(\omega)\,e^{-(\omega-\Delta\mu)/k_BT} \end{aligned} \tag{2.121}$$

We now have the spontaneous emission rate expressed in terms of absorption-related quantities that we are able to compute. Depending on which level of theory we consider, we can plug in either Eq. (2.114) at the independent particle level or Eq. (2.115) to include the excitonic effects. Note that in the latter case, the refractive index is calculated differently :

$$n_1^{exc}(\omega) = \sqrt{\tfrac{1}{2}\sqrt{\varepsilon_1^{exc}(\omega)^2+\varepsilon_2^{exc}(\omega)^2}+\varepsilon_1^{exc}(\omega)}. \tag{2.122}$$

We can slightly anticipate the following parts of this thesis and mention how this relation is modified in the case of indirect transitions, assisted by phonons :

$$R^{sp,exc}_{\mu q}(\omega) = \frac{n_1^{exc}(\omega)\omega(\omega-2\Omega_{q\mu})^2}{\pi^2c^3}\varepsilon_2^{exc}(\omega-2\Omega_{q\mu})n_B(\omega), \tag{2.123}$$

where $\Omega_{q\mu}$ refers to a phonon frequency for the phonon mode μ at momentum q, which will be introduced in the next section and n_B is the Boltzmann distribution.

2.5. Phonons and electron-phonon coupling

In solids, the collective motion of atoms can be treated as quasiparticles, called *phonons*. They represent the vibrational eigenmodes of atoms in the crystal. In this thesis we use the harmonic approximation, which means that we approximate the potential acting on the atoms as a sum of coupled harmonic oscillators. In this approximation the phonons are eigenstates of the system with infinite lifetime. Corrections due to the anharmonicity or to the coupling between electronic and atomic motions introduce a finite lifetime for the atomic vibrations, but these effects are not considered here.[66] A phonon is a quantum of lattice vibrations and similarly to the crystal momentum $\mathbf{k}$ of the electrons, phonons have a crystal momentum that we call $\mathbf{q}$. In a unit cell containing multiple atoms, there are two types of phonons based on the relative motion of the atoms. When the atoms oscillate in phase, the resulting vibration propagates as a sound wave, and these phonons are known as acoustic phonons. On the other hand, if the atoms oscillate in opposition of phases, the phonons are referred to as optical phonons.

Vibrational modes and their frequencies can be calculated classically by modelling the crystal by atoms linked with springs with different rigidities. One can also solve the problem analytically for simpler systems in the second quantization formalism.[79] Here I will present a scheme based on DFT which allows to compute the phonon frequencies and eigenvectors from the variation of the Kohn-Sham potential with respect to the atomic displacements. The following formulation is mainly adapted from Refs. [39, 77, 80].

We are still in the Born-Oppenheimer approximation presented in Sec. 2.1, *i.e.* the ionic Hamiltonian depends on the electronic potential evaluated only at the static ionic positions. Reciprocally, the electronic Hamiltonian depends parametrically on the ionic positions $\{\mathbf{R}\}$. The vibrational problem can be solved starting from the Taylor expansion of the total energy of the solid around the equilibrium positions of the atoms. We truncate the expansion at the second order, which is the *harmonic approximation*. It reads :

$$\begin{aligned} E(\{\mathbf{R}\}) = {} & E(\{\mathbf{R}^0\}) \\ & + \sum_{Ls\alpha} \left. \frac{\partial E(\{\mathbf{R}\})}{\partial R^0_{Ls\alpha}} \right|_0 (R_{Ls\alpha - R^0_{Ls\alpha}}) \\ & + \frac{1}{2} \sum_{\substack{Ls\alpha \\ Mt\beta}} \left. \frac{\partial^2 E(\{\mathbf{R}\})}{\partial R^0_{Ls\alpha} \partial R^0_{Mt\beta}} \right|_0 (R_{Ls\alpha} - R^0_{Ls\alpha})(R_{Mt\beta} - R^0_{Mt\beta}) + \dots \end{aligned} \tag{2.124}$$

where $\{\mathbf{R}\}$ and $\{\mathbf{R}^0\}$ are the set of positions and equilibrium positions of all the nuclei in the system. They depend on three indices : s, t count the nuclei in the unit cell, L, M denote for the unit cell index in the whole crystal and α, β are for the Cartesian directions. The first line of the above expression is the total energy evaluated at equilibrium positions, which in our case is calculated within DFT. The second line is the force acting on a nucleus when displaced around its equilibrium position. It is defined as :

$$F_{Ls\alpha} \equiv -\frac{\partial E(\{\mathbf{R}\})}{\partial R^0_{Ls\alpha}}. \tag{2.125}$$

The third term is the Hessian of the Born-Oppenheimer energy surface, or the force acting on the nucleus (Ls) induced by the displacement of another nucleus (Mt). We define the matrix of interatomic force constants as :

$$C^{Ls\alpha}_{Mt\beta} \equiv \frac{\partial^2 E(\{\mathbf{R}\})}{\partial R^0_{Ls\alpha} \partial R^0_{Mt\beta}} = -\frac{\partial F_{Ls\alpha}}{\partial R^0_{Mt\beta}} \tag{2.126}$$

The higher order terms are anharmonic and are relevant for the calculation of phonon lifetimes or temperature dependence of lattice constants for instance. We do not consider them in this thesis and work only in the harmonic approximation.

We now reformulate the problem in term of the atomic *displacements*, defined as

$\mathbf{u}_{Ls} = \mathbf{R}_{Ls} - \mathbf{R}^0_{Ls}$. Then the total energy writes :

$$E(\{\mathbf{R}\}) = E(\{\mathbf{R}^0\}) - \sum_{Ls\alpha} F_{Ls\alpha} u_{Ls\alpha} + \frac{1}{2} \sum_{\substack{Ls\alpha \\ Mt\beta}} C^{Ls\alpha}_{Mt\beta}\, u_{Ls\alpha} u_{Mt\beta} + \mathcal{O}(u^3) \tag{2.127}$$

In practice, we calculate the phonon properties on relaxed structures, which means the forces acting on the atoms are zero. Hence we only need the information from the C matrix. The size of the interatomic force constants matrix is $3N_c N_{at}$ where N_c is the number of unit cells in the periodic supercell considered and N_{at} is the number of atoms in the unit cell. However we can use the invariance of the force constants under a translation by a lattice vector τ, which means they only depend on the difference $\tau_I = \tau_L - \tau_M$. This allows us to take the Fourier transform and solve the problem in reciprocal space, where only a unit cell is needed and the sum over supercells is replaced by a sum over a grid of $\mathbf{q}$-points in the Brillouin Zone. We define the *dynamical matrix* as :

$$D^{s\alpha}_{t\beta}(\mathbf{q}) = \frac{1}{\sqrt{M_s M_t}} \sum_I C^{Is\alpha}_{t\beta} \mathrm{e}^{i\mathbf{q}\cdot\tau_I} \tag{2.128}$$

where M_s is the mass of atom s. The square of the phonon frequencies are eigenvalues of the dynamical matrix with the following eigenvalue problem :

$$\sum_{s\alpha} D^{s\alpha}_{t\beta}(\mathbf{q}) \xi^{\mu}_{s\alpha}(\mathbf{q}) = \omega^2_{\mu}(\mathbf{q}) \xi^{\mu}_{t\beta}(\mathbf{q}) \tag{2.129}$$

with the eigenvectors $\xi^{\mu}(\mathbf{q})$ associated with the mode μ, that are the normal modes of the oscillating system and obey the orthogonality relations :

$$\sum_{s\alpha} \xi^{\mu *}_{s\alpha} \xi^{\nu}_{s\alpha} = \delta_{\mu\nu}, \qquad \sum_{\nu} \xi^{\mu *}_{s\alpha} \xi^{\mu}_{t\beta} = \delta_{st}\delta_{\alpha\beta}. \tag{2.130}$$

Here we see the picture of collective motion emerge. Indeed the problem is no longer described as the sum of individual displacements, but rather in terms of $3N_{at}$ collective, periodic oscillations of the crystal with a momentum $\mathbf{q}$ and a frequency $\omega_\mu(\mathbf{q})$, which are independent of each other.

From this, we can obtain an expression for the atomic displacements in real-space and time, which have the form of standing waves :

$$u_{Ls\alpha}(t) = \frac{1}{2\sqrt{N_c M_s}} \sum_{\mu q} \mathrm{e}^{i\mathbf{q}\cdot\tau_L}\; \xi^{\mu}_{s\alpha}(\mathbf{q}) \left[A_\mu(\mathbf{q}, T) \mathrm{e}^{-i\omega_\mu t} + A^*_\mu(\mathbf{q}, T) \mathrm{e}^{i\omega_\mu t} \right] \tag{2.131}$$

where the temperature-dependent amplitudes of the oscillations are given by the equipartition theorem $A_\mu(\mathbf{q}, T) = \sqrt{2k_B T}/\omega_\mu(\mathbf{q})$ with k_B the Boltzmann constant.[81] In summary, we see that the crucial vibrational quantities are obtained after calculating the interatomic force constants matrix, and then diagonalizing the dynamical matrix. One way to do the former starting from DFT is presented in the next section.

2.5.1. Density Functional Perturbation Theory

This theory is a general formulation of the linear response of the Kohn-Sham wavefunctions and charge density obtained in DFT with respect to a perturbation. It is presented by Baroni *et al.* in Ref. [39], where they show that the linear response can be calculated in a self-consistent manner in reciprocal space, independently of the wavelength of the perturbation. This means that the use of supercells is not needed. In the case of phonons, one needs to compute the Hessian of the Born-Oppenheimer energy surface, which is the second derivative of the ground-state energy with respect to atomic displacements. One can show that the force constants matrix can be obtained from DFT with the following expression [82] :

$$\begin{aligned} C_{Mt}^{Ls} &= \left.\frac{\partial^2 E(\{\mathbf{R}\})}{\partial \mathbf{R}_{Ls}\partial \mathbf{R}_{Mt}}\right|_{\mathbf{R}=\mathbf{R}_0} = -\left.\frac{\partial \mathbf{F}_{Ls}}{\partial \mathbf{R}_{Mt}}\right|_{\mathbf{R}=\mathbf{R}_0} \\ &= \int \frac{\partial n(\mathbf{r})}{\partial \mathbf{R}_{Ls}}\frac{\partial v_{ext}(\mathbf{r})}{\partial \mathbf{R}_{Ls}} d^3r + \int n(\mathbf{r})\frac{\partial^2 v_{ext}(\mathbf{r})}{\partial \mathbf{R}_{Ls}\partial \mathbf{R}_{Mt}} d^3r + \frac{\partial^2 E_N(\mathbf{R}^0)}{\partial \mathbf{R}_{Ls}\partial \mathbf{R}_{Mt}} \end{aligned} \tag{2.132}$$

where v_{ext} and E_N are the ionic potential acting on the electrons and the nucleus-nucleus interaction, defined in Sec. 2.1, and n is the DFT groundstate electronic density. Its first derivatives are computed in a self-consistent way with the linearization of Eq. (2.11) :

$$\frac{\partial n(\mathbf{r})}{\partial \mathbf{R}_{Ls}} = 4\,\mathrm{Re}\sum_n \langle\psi_n|\,\frac{\partial}{\partial \mathbf{R}_{Ls}}\,|\psi_n\rangle \tag{2.133}$$

The change of the Kohn-Sham states is in turn obtained from first-order perturbation theory and summing over all the eigenstates :

$$\frac{\partial\,|\psi_n\rangle}{\partial \mathbf{R}_{Ls}} = \sum_{m\neq n} |\psi_m\rangle\,\frac{\langle\psi_m|\,\frac{\partial v_{\text{eff}}}{\partial \mathbf{R}_{Ls}}\,|\psi_n\rangle}{\epsilon_n-\epsilon_m} \tag{2.134}$$

This problem can be reformulated such that no empty states are needed :

$$(\hat{H}-\epsilon_n)\frac{\partial\,|\psi_n\rangle}{\partial \mathbf{R}_{Ls}} = -\left(\frac{\partial v_{\text{eff}}}{\partial \mathbf{R}_{Ls}} - \frac{\partial \epsilon_n}{\partial \mathbf{R}_{Ls}}\right)|\psi_n\rangle\,. \tag{2.135}$$

Eq. (2.135) corresponds to a reformulation of the DFT response of the system to an atomic displacement in the form of a Sternheimer equation.[83]

Long wavelength limit

Care has to be taken in the long wavelength limit, or equivalently the $\mathbf{q} \to 0$ limit. In this limit, the periodicity of the phonons tends to infinity, and it has consequences on both acoustic and optical modes. There will always be 3 acoustic modes in any crystal, one for each degree of freedom of the atom. When there are two or more atoms in the unit cell, there are $3N_{at} - 3$ optical modes.

The acoustic modes have a linear dispersion at small momenta, and they are constrained by the translational invariance of the crystal : at $\mathbf{q} = 0$ an acoustic phonon mode corresponds to a rigid translation of all atoms in the crystal in the same direction. This translation should have a frequency identically equal to zero. It might not be rigorously respected when computing the phonon dispersion numerically. For this reason, the acoustic sum rule is enforced to maintain the linear dispersion :

$$\sum_t C^{Is\alpha}_{t\beta}(|\tau_I| \to \infty) = 0 \tag{2.136}$$

In the case of non-2D polar semiconductors and insulators – hBN, the material we study in this thesis, falls in this category – the difference of electronegativity between the two types of atom creates electric dipoles, which in turn create long range electric fields when the atoms are oscillating out of phase. This is the case for optical phonons, whose frequencies are finite at $\mathbf{q} = 0$. At small momenta, the transverse optical (TO) modes, whose direction of propagation is orthogonal to the momentum $\mathbf{q}$, are unaffected. However the longitudinal optical (LO) modes can interact with the long range electric fields and their frequencies become larger. Hence there is a LO-TO frequency splitting at $\mathbf{q} = 0$ which can only be accounted for by adding a non-analytical term to the force constants matrix, given by :

$$\tilde{C}^{\mathrm{NA}s\alpha}_{t\beta}(\mathbf{q} \to 0) = \frac{4\pi}{\Omega} e^2 \frac{(\mathbf{q} \cdot \mathbf{Z}^*_s)_\alpha (\mathbf{q} \cdot \mathbf{Z}^*_t)_\beta}{\mathbf{q} \cdot \varepsilon^\infty \cdot \mathbf{q}} \tag{2.137}$$

The Born effective charges Z^* and the electronic contribution to the dielectric permittivity tensor ε^∞ can be obtained from Density Functional Perturbation Theory (DFPT) with a macroscopic electric field as the perturbation.[39]

2.5.2. Electron-phonon coupling

In the previous sections, we solved the problem of electrons and ions independently of one another. Here we will reintroduce the coupling between these two systems. The coupled system of electrons and phonons is described by a three-part Hamiltonian :

$$\hat{\mathcal{H}} = \hat{H}_e + \hat{H}_p + \hat{H}_{ep} \tag{2.138}$$

The electron-electron interactions are contained in the Kohn-Sham Hamiltonian, that can be written in second quantization $\hat{H}_e = \sum_{n\mathbf{k}} \epsilon_{n\mathbf{k}} \hat{a}^\dagger_{n\mathbf{k}} \hat{a}_{n\mathbf{k}}$. We can define the nuclear

Hamiltonian as a sum of quantum harmonic oscillators, which has the following second-quantized form :

$$\hat{H}_p = \sum_{\mathbf{q}\mu} \hbar\omega_\mu(\mathbf{q}) \left(\hat{b}^\dagger_{\mathbf{q}\mu} \hat{b}_{\mathbf{q}\mu} + \frac{1}{2} \right) \tag{2.139}$$

where $\hat{b}$ and $\hat{b}^\dagger$ are annihilation and creation operators of a phonon with momentum $\mathbf{q}$ and branch index μ. They follow the commutation relations $\left[\hat{b}_{\mathbf{q}\mu}, \hat{b}^\dagger_{\mathbf{q}'\mu'} \right] = \delta_{\mathbf{q},\mathbf{q}'}\delta_{\mu,\mu'}$ and $\left[\hat{b}_{\mathbf{q}\mu}, \hat{b}_{\mathbf{q}'\mu'} \right] = \left[\hat{b}^\dagger_{\mathbf{q}\mu}, \hat{b}^\dagger_{\mathbf{q}'\mu'} \right] = 0$. We see that in the Born-Oppenheimer and harmonic approximations, lattice vibrations are quantized as perfect bosons.

With these we can construct the electron-phonon Hamiltonian as the first order expansion of the effective potential in terms of the atomic displacements :

$$H^{(1)}_{ep} = \sum_{Ls\alpha} \frac{\partial v_{\text{eff}}}{\partial R_{Ls\alpha}} u_{Ls\alpha} = \sum_{nm\mu\mathbf{kq}} g^{\mu\mathbf{q}}_{nm\mathbf{k}} \hat{a}^\dagger_{n\mathbf{k}} \hat{a}_{m\mathbf{k}-\mathbf{q}} (\hat{b}_{\mathbf{q}\mu} + \hat{b}^\dagger_{-\mathbf{q}\mu}). \tag{2.140}$$

In the last equality, the electron-phonon coupling matrix element g is introduced. It is the probability that a phonon of branch index μ and momentum $\mathbf{q}$ scatters a Kohn-Sham electron from a state $|m\mathbf{k}-\mathbf{q}\rangle = |\psi_{m\mathbf{k}-\mathbf{q}}\rangle$ into another state $|n\mathbf{k}\rangle$. It is written in a simplified form as :

$$g^{\mu\mathbf{q}}_{nm\mathbf{k}} = {}_{uc}\langle n\mathbf{k}| \Delta_{\mathbf{q}\mu} v_{\text{eff}} \, |m\mathbf{k}-\mathbf{q}\rangle_{uc} \tag{2.141}$$

or in a more complete form, following the notation adopted by Giustino in Ref. [66] :

$$g^{\mu\mathbf{q}}_{nm\mathbf{k}} = g^{\mu}_{nm}(\mathbf{k},\mathbf{k}-\mathbf{q}) = \sum_{Ls} \mathrm{e}^{i\mathbf{q}\cdot\mathbf{R}_{Ls}} \, \frac{\xi^\mu_s(\mathbf{q})}{\sqrt{2M_s\omega_\mu(\mathbf{q})}} \; {}_{uc}\langle n\mathbf{k}| \frac{\partial v_{\text{eff}}}{\partial \mathbf{R}_{Ls}} \, |m\mathbf{k}-\mathbf{q}\rangle_{uc} \tag{2.142}$$

where the subscript uc signifies that the integral is taken over a unit cell of the crystal, using the lattice-periodic parts of the Kohn-Sham wavefunctions $u_{n\mathbf{k}}$. These matrix elements are the one we will use throughout this thesis to compute the magnitude of the interaction between electrons and phonons. They are also a key ingredient to define the exciton-phonon coupling *ab initio*.

Note that one can go beyond the first order and compute for instance the matrix elements generated by the second derivative of the effective potential with respect to the atomic displacements. One would obtain the so-called Debye-Waller term, which can be used in a self-energy framework to compute the renormalization of the electronic bands by the lattice vibrations.[66, 84, 85]

Summary of Chapter 2

Summary of Section 2.2

- Density Functional Theory allows to compute the ground state density $n(\mathbf{r})$ and the equilibrium crystal structure of materials.
- The Kohn-Sham eigenvalues $\epsilon_i(\mathbf{r})$ obtained from DFT give an estimation of the band structure.
- Along with the Kohn-Sham wavefunctions $\psi_i(\mathbf{r})$, these are the starting quantities for the more involved calculations presented in the following sections.

Summary of Section 2.3

- The GW approximation includes many-electron effects for weakly correlated systems, that are absent in DFT.
- We obtain from this the quasiparticle corrections that give more accurate electronic band structures.
- We switch to a basis of bound electron-hole pair, the so-called excitons, better suited to describe optical processes.
- We compute the exciton properties with the Bethe-Salpeter equation, from which we obtain exciton energies and eigenvectors.

Summary of Section 2.4

- We simulate optical spectra with the linear response function obtained from MBPT, including excitonic effects.
- The imaginary part of the dielectric function, calculated *ab initio*, gives access to the optical absorption spectrum.
- We use a steady state approximation to obtain the luminescence spectrum from the absorption one.

Summary of Section 2.5

- Phonons are quanta of vibrations of the lattice.
- They are quasiparticles with frequencies and eigenvectors that we obtain from DFPT.
- The coupling between electrons and phonons enters an Hamiltonian in second quantization, in the form of matrix elements.

3. Hexagonal Boron Nitride under strain

This chapter is partly based on our publication Ref. [86]. Some of the text and figures contained in this Chapter are adapted from this reference.

Contents

3.1. Introduction and experimental motivations

Strain is a powerful tool to engineer electronic and optical properties of materials. It is possible to modify the electronic dispersion of strained crystals, in particular the position of the conduction and valence band extrema. In some cases it can even lead to direct to indirect bandgap transitions, as it was shown for Germanium [87, 88] and more recently for transition metal dichalcogenides.[89, 90, 91] Regarding hBN, the effect of strain on vibrational properties was investigated experimentally in exfoliated samples with various thicknesses,[92] while theoretically biaxial tensile strain was considered for the mono- and bilayer hBN [93, 94] as well as its role on hBN quantum emitters.[95] However, little is known about the effect of strain on the optical properties of bulk hBN, which is the simplest mean to characterize this material.

A recent experiment showed a remarkable modification of the cathodoluminescence spectrum of hBN under strain.[96] In this experiment Léonard Schué and colleagues suspended a nanosheet of hexagonal Boron Nitride over a trench carved out from an SiO_2 substrate. The nanosheet is about 100 nm thick and curves under the effect of gravity, as illustrated in Fig. 3.1(a), and was imaged by Atomic Force Microscopy (AFM) (Fig. 3.1(b)). When measuring the cathodoluminescence spectra at different positions on the sample, one can see that the intensity ratios between different peaks are varying. Their interpretation is that the deformation of the sample induces uniaxial (compressive) strain,

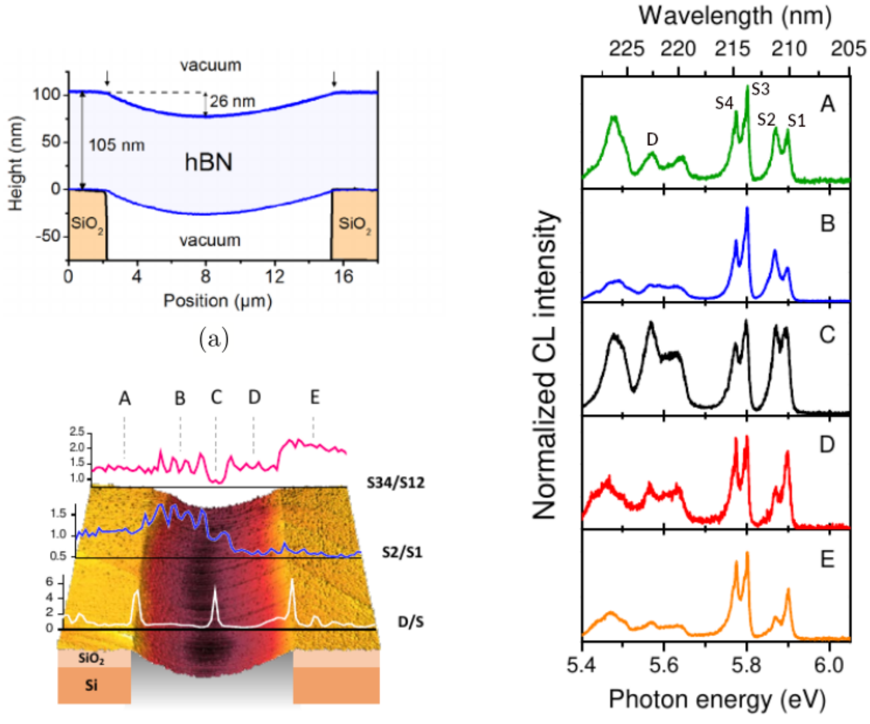

(a)

(b)

(c)

Figure 3.1. – (a) Sketch of the deposited hBN nanosheet on the trench. (b) AFM profile and relative intensity ratios of different emission peaks with respect to spatial region. (c) Cathodoluminescence intensity measured on different regions of the sample. Courtesy of Léonard Schué and Julien Barjon

perpendicular to the trench. This strain could have an effect on the recombination process of excitons or their scattering with phonons, leading to a change in the luminescence intensity. They measured an intensity ratio between the S1/2 and the S3/4 peaks varying from ≈ 4 at equilibrium to almost 1 at the bottom of the trench. In this Chapter we try to simulate this phenomenon and use a finite difference method to reproduce the phonon-assisted luminescence in strained structures from first principles.

3.2. Structure and phonons

In order to simulate the hBN sample in suspension, we consider an infinite bulk crystal under uniaxial strain. In the experiment, the beam of electron penetrates only on the upper part of the nanosheet, where the strain is compressive. However we study a range of strain including both stretching and compression around the equilibrium structure. First, we obtain the strained structure by taking an orthorombic cell of the pristine crystal, larger than the hexagonal unit cell. Because it has three orthogonal lattice vectors, the orthorombic cell is more suited for the application of a uniaxial strain for the geometry

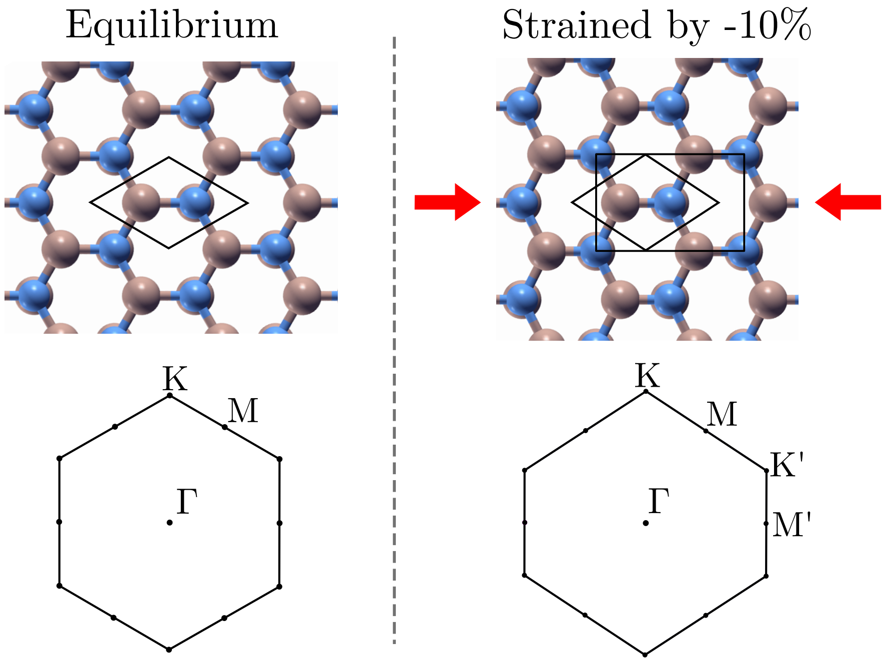

Figure 3.2. – Left : top view of the equilibrium crystal with the unit cell and the corresponding hexagonal Brillouin Zone below. Right : top view of the strained crystal, for a compression of 10% of the equilibrium bond length. The pseudo-hexagonal diamond-shaped unit cell is shown with the corresponding deformed hexagonal Brillouin Zone. The orthorombic unit cell, more practical to apply uniaxial strain as discussed in the text, is also drawn.

relaxation. To do so, we simply alter the length of one cell vector, up to an arbitrary length corresponding to a value of strain. We studied different strain values, in an interval going from a $+2.5\%$ to a -2.5% variation of the equilibrium length. In this work we applied strained in the armchair direction, the one parallel to the B-N bond. After setting the length of the cell to the desired length corresponding to a strain value, we let the atom positions and the other two cell vectors relax, using a damped molecular dynamics algorithm where the forces acting on the atoms are computed in DFT using the Hellmann–Feynman theorem. This procedure in implemented in the QUANTUM ESPRESSO suite.[56, 57] More computational details can be found in Appendix C. We found that once the two cell vectors orthogonal to the strained one are relaxed, their length is linearly proportional to the strain value.

Once we have the relaxed strained orthorombic cells, we construct a pseudo-hexagonal unit cell containing only four atoms. This way, we can compare the structures obtained for different strain values with the equilibrium structure in a consistent way and proceed with the calculation of electronic and optical properties. To construct the pseudo-hexagonal cells from the strained orthorombic ones, we followed the procedure described in Appendix B. We computed the phonon-related properties using DFPT in the four-atom

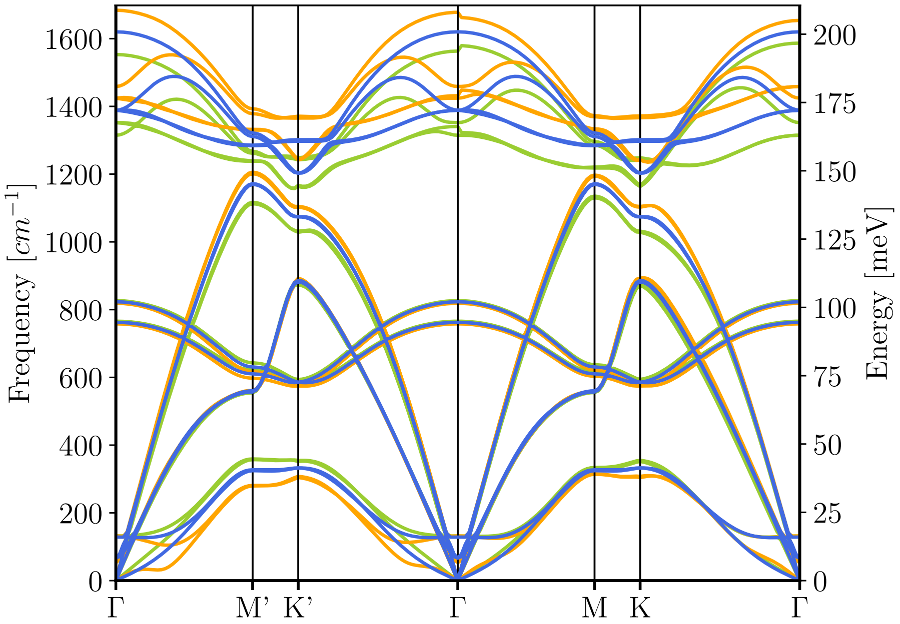

Figure 3.3. – Phonon dispersion versus uniaxial strain. Blue lines are at equilibrium, green lines at 2.5% stretch and orange lines at 2.5% compression.

strained cells. In the strained crystal, whatever the value of strain, the 120° rotational symmetry is broken and this makes the M and K points in the BZ nonequivalent to the M' and K' points. The path between high-symmetry points containing all four of these points can be seen in Fig. 3.2. The resulting phonon dispersions are shown in Fig. 3.3, for three strain values : a $+2.5\%$ stretch, a -2.5% compression and the equilibrium one. For the unstrained dispersion we can notice the splitting of the highest branch at Γ with the two branches below. This is the LO-TO splitting mentioned in Sec. 2.5.1.

We found that the optical modes (the branches with the highest energies) are the most affected by strain. With compressive strain, their frequencies are increased at all $\mathbf{q}$ points and they are decreased for tensile strain. We also observe the splitting of the E_{2g} modes, whose frequencies are degenerate at Γ just below 175 meV (1400 cm^{-1}) for the unstrained structure. They split as soon as a strain is applied. This is in agreement with Raman measurements and previous calculations.[97, 92] It is also interesting to notice that depending on the direction along which the Γ point is approached, the splitting of the two E_{2g} modes has different magnitudes.

On the mid-energy range of the dispersion, the LA, TA and TO modes are not very affected by strain. This will be important in the discussion about luminescence in the following.

At the lower frequency end, the acoustic modes are affected in an opposite way. Under compression, their frequencies are decreased and increased under stretch. The orange curve shows a softening of the lowest branch close to Γ. We noticed that increasing the value of compressive strain leads to the appearance of negative frequencies. This happens

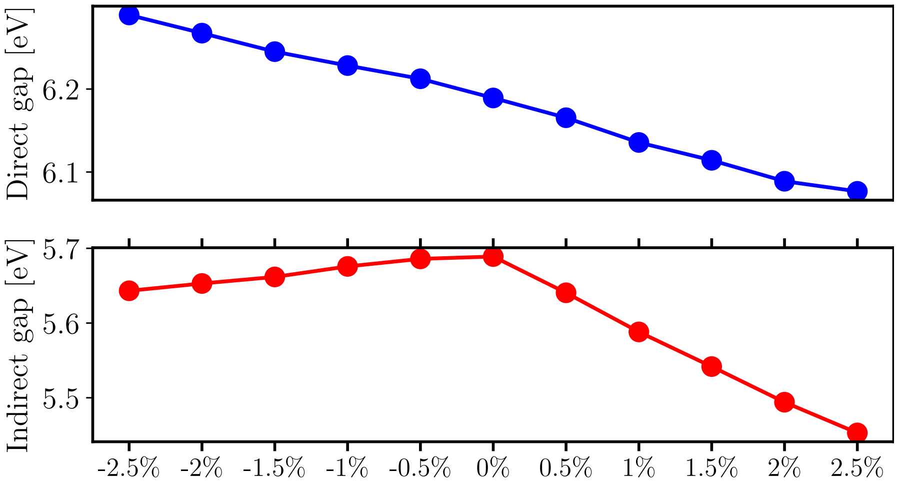

Figure 3.4. – Quasiparticle corrections to the direct and indirect bandgaps at the G_0W_0 level with respect to strain.

when the geometry is unstable. Then the second derivative in Eq. (2.126) is negative and the eigenvalues ω^2 in Eq. (2.129) are negative. The imaginary solutions would be plotted as negative, by convention. We did not investigate this instability caused by compression, since the range of strain we are interested in is below $+2.5\%$ of strain. Nonetheless, the phonon dispersions show that our systems are stable in the range of strain considered.

3.3. Electronic band structure

In order to study the electronic band structure of strained hBN, we first computed the Kohn-Sham eigenvalues in DFT and then we performed a one-shot G_0W_0 calculation to compute the quasiparticle corrections using the `yambo` code.[58] We found that these corrections are a rigid shift in energy of the KS eigenvalues, independently of the strain applied in the range we considered. In Fig. 3.4 we report the variation of the direct gap (at M) and of the indirect gap (between K and M) with respect to strain. The direct gap decreases linearly with increasing relative values of strain, while the indirect gap is maximal for the unstrained system and decreases both for compression and stretch.

The electronic dispersions along the path in reciprocal space shown in Fig. 3.2 are plotted in Fig. 3.5 for the two maximally strained systems and for the unstrained one. At equilibrium, the direct gap is located between states at M. The indirect gap is between a point close to K for the valence band and the M point for the conduction band. As discussed above, strain breaks one of the symmetries of the crystal and this effect is visible on the dispersions at high-symmetry points. Under compression, the conduction band is shifted down at M while it is increased at M'. This trend is reversed under stretch. Hence, the conduction band minimum is at M for the compressed crystal and at M' for the stretched crystal. These variations can be explained in term of the variation of the

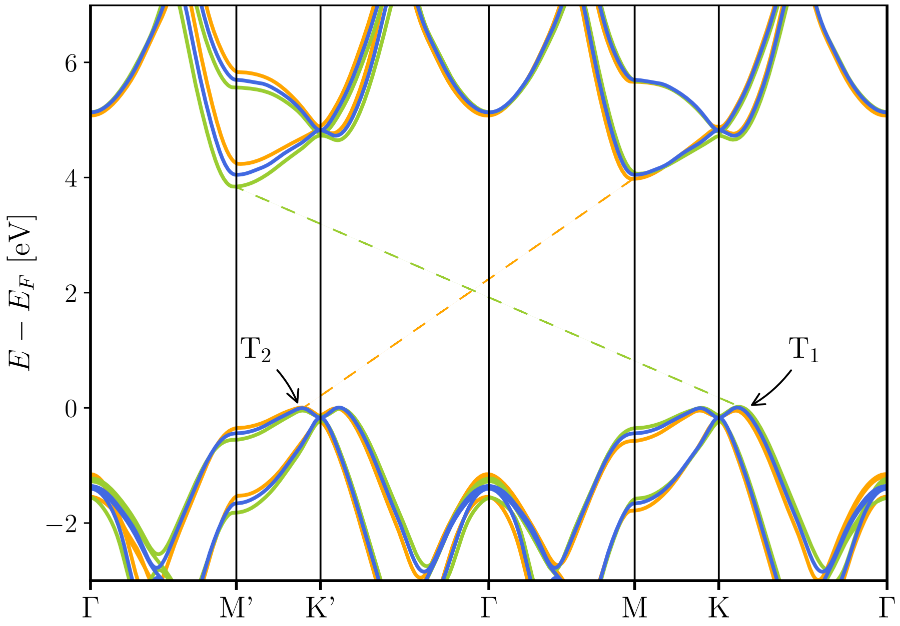

Figure 3.5. – Details of the electronic band structure under the maximum stretch and compression considered in the manuscript. Blue lines are at equilibrium, green lines at +2.5% stretch and orange lines at -2.5% compression. We report also the location of the new indirect gaps in the two cases. Notice that at equilibrium all indirect transitions between the different K and M points are equivalent.

orbital properties. The π^* atomic-like orbitals at M and M' have a different shape, as

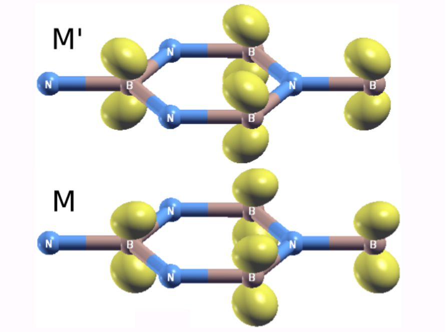

Figure 3.6. – π^* atomic-like orbitals of the conduction band minima on one of the layers for a compression of 0.5%. At M', the components of the wavefunctions are oriented along the compressed B-N bond. At M, they are oriented along one of the other bonds.

illustrated in Fig. 3.6 for a compression of 0.5%. While they are degenerated in energy for the unstrained crystal, this degeneracy is lifted due to the symmetry breaking. The state with orbital components along the strained bond is the one whose energy changes with strain at M'. Moreover these orbitals have a strong dependence on the interlayer interactions,[98] which in turns depends on the interlayer distance. This distance varies linearly with the strain applied to the system in our relaxation process. These two effects, the breaking of the in-plane symmetries and the change in the interlayer interaction, explain the splitting and shift of the bands induced by strain at the M' point.

The valence states around K and K' are only slightly changed in energy. This can be explained because the orbitals corresponding to these states are protected from interlayer interactions by symmetry, as shown in the theoretical study of Ref. [98]. There is nonetheless a slight change in energy, which causes the valence band maximum to be located at the point called T_2 under compression and at T_1 under stretch. These two points are close to K. All these modifications of the band structure induce a change in the position of the minimal indirect band gaps for compressive and tensile strain that are indicated by the dotted lines in Fig. 3.5.

3.4. Excitons and absorption

At the low-energy end of the excitonic spectrum of bulk hBN, we find two pairs of degenerate excitons. The splitting between the pairs is caused by the interlayer interactions and is called the Davydov splitting.[99] The two pairs transform differently under inversion operation (*i.e.* taking $\mathbf{r} \to -\mathbf{r}$ or $\mathbf{k} \to -\mathbf{k}$), as explained in Appendix D. The pair with the lowest energy is even for inversion symmetry, which means it is dark in absorption. The second lowest pair instead is odd for inversion symmetry and thus bright. Note that this is true for one-photon absorption, at the linear response level. In non-linear optics, for instance two-photon absorption, the dark and bright characters are reversed.[100] The 120° rotational symmetry breaking induced by uniaxial strain has an effect on the degeneracy of the Davydov pairs. First, looking at the energies of the four lowest excitons at Γ, as displayed in panel (a) of Fig. 3.7, we see that the energies are split, both for compression and stretching. These changes in energy are mainly due to the change in electronic gap reported in the above section. Indeed, they follow the same linear trend as the strain value increases and are of the same magnitude, about ± 0.1 eV. We could also verify that the binding energies of the direct excitons remain approximately constant on the strain range considered, varying only by 10 to 15 meV.

The associated absorption spectra are displayed in panel (b) of Fig. 3.7. As the inversion symmetry is not broken by uniaxial strain, the lowest two excitons remain dark when strain is applied. For the third and fourth lowest excitons in the strained systems, they are not degenerate anymore, as it is the case in the pristine crystal, due to the breaking of rotational symmetry. This gives both excitons a non-zero dipole, and we see two peaks appearing in the absorption spectra.

The change of peak energy induced by strain is quantified by the strain gauge factor, which is defined as the spectral shift per % of uniaxial strain. From our calculations, we find a value of $\approx$ 43 meV/%, which is in the same range as transition metal dichalcogenides as reported in Ref. [101].

The splitting is also visible on the exciton wavefunctions in real space. It is displayed in Fig. 3.8 for the lowest two excitons at Γ, for a stretch of +2.5%. In the pristine

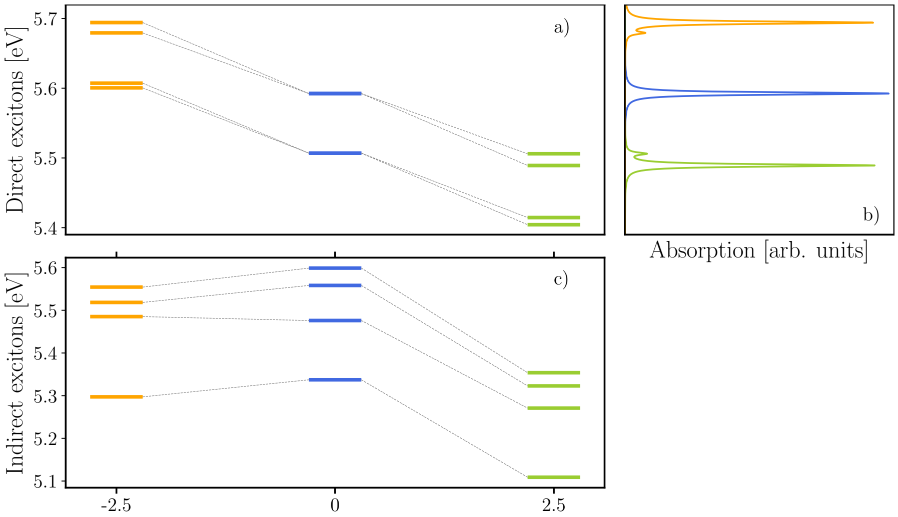

Figure 3.7. – (a) Energies of the lowest 4 excitons at Γ (b) Absorption spectra associated with the direct excitons. Both excitons of the bright Davydov pair have a non-zero dipole matrix element and we can distinguish two peaks in the spectra for the strained crystals. (c) Energies of the lowest 4 indirect excitons. Blue lines are for equilibrium crystal, orange is for compression and green is for stretch.

crystal, these two wavefunctions are mixed and have a circular shape. Here the splitting is clearly visible on the shape of the distribution, with one of the wavefunctions having its components along the strained B-N bond or the armchair direction, while the other has its components along the zigzag direction.

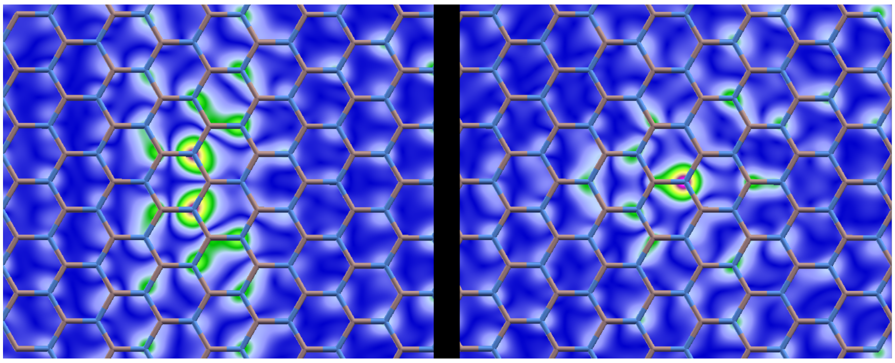

Figure 3.8. – Electron distribution when the hole is fixed near the central Nitrogen atom, that we call exciton wavefunction. Left is the lowest dark exciton at Γ, right is the second lowest dark exciton at Γ, taken for a stretch of +2.5%. Note that the wavefunctions of the lowest bright excitons, not shown here, have the same structure as the dark ones

We observe the same trend for the lowest-lying excitons with non-zero momentum, which we will call indirect excitons because they are formed by indirect electronic transitions. Their change in energy with strain is reported in Fig. 3.7 (c). It follows the same variation as the indirect gap and here again their binding energy is almost invariant with strain. The indirect excitons of hBN play an important role in light emission by luminescence. These changes in energy combined with the change in phonon frequencies will have an impact on the luminescence spectra of the strained crystals. This will be discussed in the next two sections.

3.5. Exciton-phonon coupling from finite differences

As presented in the introduction of the thesis, the inclusion of lattice vibrations in our computational framework is necessary to describe accurately the phonon-assisted features in the luminescence spectrum of hBN. In particular the exciton-phonon coupling is the central quantity to take into account. To do so, I present in this section how to calculate the macroscopic dielectric function with a static correction due to lattice vibrations, in a finite-difference scheme. The method can be found in Ref. [29] and in a slightly different approach in Ref. [28].

The key idea is to take the Taylor expansion of the macroscopic dielectric function with respect to atomic displacements. By displacing the atoms around their equilibrium positions along the phonon eigenvectors obtained earlier with DFPT and calculating the response function with the BSE in the displaced configurations, we will obtain the coupling between the exciton responsible for the optical response and the phonons. The link between the response function and the macroscopic dielectric function is given by Eq. (2.112).

Our goal is to write the dielectric constant as a term at equilibrium plus a correction due to the atomic motion as $\varepsilon(\omega) \approx \varepsilon^{(0)}(\omega) + \varepsilon_{\bar{q}}^{st,(2)}(\omega)$, where the second term is the static correction induced by the atomic displacements, and it will be averaged over the displacements along all phonon modes.[49] The contribution from exciton λ to the response function writes :

$$\chi^{\lambda}_{R=0}(\omega) = \frac{|T^{\lambda}_{R=0}|^2}{E^{\lambda}_{R=0} - \omega + i\eta} \tag{3.1}$$

where the subscript $R = 0$ indicates that the quantities are evaluated at clamped ion positions. The infinitesimal η is taken independent of R for simplicity. The single-exciton contribution can be highlighted by writing :

$$\chi_{R=0}(\omega) = \sum_{\lambda} \chi^{\lambda}_{R=0}(\omega), \tag{3.2}$$

$$\epsilon_M(\omega) = 1 - 4\pi\chi_{R=0}(\omega) = 1 - 4\pi \sum_{\lambda} \frac{|T^{\lambda}_{R=0}|^2}{\omega - E^{\lambda}_{R=0} + i\eta}, \tag{3.3}$$

The exciton dipoles are defined as $T^\lambda = \sum_{cvk} \bar{A}^{cvk}_\lambda d_{cvk}$, with the dipole matrix elements $d_{cv\mathbf{k}} = \langle v\mathbf{k}|\hat{r}|c\mathbf{k}\rangle$. The first derivative entering in the Taylor expansion will be :

$$\left.\frac{\partial \chi^\lambda_R(\omega)}{\partial R}\right|_{R=0} = \left.\frac{\partial |T^\lambda_R|}{\partial R}\right|_{R=0} \frac{2|T^\lambda_{R=0}|}{E^\lambda_{R=0} - \omega + i\eta} + \left.\frac{\partial \left[E^\lambda_R - \omega + i\eta\right]^{-1}}{\partial R}\right|_{R=0} |T^\lambda_{R=0}|^2. \quad (3.4)$$

This expression has a term linear in the exciton dipole and a term at the second power, both taken at clamped ion positions. It means that for dark excitons, the first derivative in the Taylor expansion will be zero, but it can have a non-zero contribution for bright excitons, for a discussion see Refs. [49, 102]. Dark excitons are labelled λ', and we have $\frac{\partial \chi^{\lambda'}_R(\omega)}{\partial R}\big|_{R=0} = 0$. In hBN, the excitons involved in luminescence are the ones with the lowest energies in the finite momentum dispersion. Because of momentum conservation, they cannot recombine and emit light which has almost zero momentum, hence they are dark at clamped ion positions. Phonons are needed to transfer momentum and assist their recombination.

Similar arguments hold for the second derivative in the Taylor expansion and the only non-vanishing term that remains is :

$$\frac{\partial^2 \chi^{\lambda'}_R(\omega)}{\partial R^2} = \left.\frac{\partial^2 |T^{\lambda'}_R|^2}{\partial R^2}\right|_{R=0} \left[E^{\lambda'}_{R=0} - \omega + i\eta\right]^{-1} \quad (3.5)$$

This equation shows that it is equivalent to compute the finite-difference derivative of the full response function or only of the exciton dipoles if we are only interested in corrections up to the second order. This was verified numerically in Ref. [29]. In our calculations, we compute the derivative of the dipoles since they can be obtained more easily in the code. This above second derivative is evaluated numerically with the finite difference formula :

$$\frac{\partial^2 \chi^{\lambda'}_R(\omega)}{\partial R^2} \approx \frac{\chi(\Delta\mathbf{R};\omega) - 2\chi_0(\omega) + \chi(-\Delta\mathbf{R};\omega)}{\Delta\mathbf{R}^2} \quad (3.6)$$

Since we are interested in phonon-assisted luminescence and we know where the minima lie in the excitonic dispersion, we know the phonon momentum $\bar{q}$ necessary to satisfy momentum conservation. Therefore we calculate the derivatives of the excitonic dipoles only for a momentum $\bar{q}$ that connect the minimum of the exciton dispersion to Γ. Then we label the displacements $R \to R_{\mu\bar{q}}$. They are along the eigenvector of a particular phonon mode μ taken at the momentum $\bar{q}$. The displacement magnitudes are given, similarly to Eq. (2.131) taken for $t = 0$, by the real part of the phonon eigenvector multiplied by a scaling factor c :

$$u^{\mu\bar{q}}_{Ls\alpha}(t=0) = \frac{c}{\sqrt{M_s}} \mathrm{Re}\left\{e^{i\bar{\mathbf{q}}\cdot\boldsymbol{\tau}_L} \xi^{\mu\bar{q}}_{s\alpha}\right\} \quad (3.7)$$

The c parameter is a scaling factor which needs to be converged. Indeed for the finite difference derivative, we want to keep the displacements as small as possible. However if they are too small, their effect will be indistinguishable from numerical noise, but if they are too large, effects beyond the second-order derivatives will start to appear. For this work, we converged the displacements to a value of $|\Delta\mathbf{R}| = 0.05$ Å. To accommodate the periodicity of the phonon at $\bar{q}$, we construct supercells that map the $\bar{q}$ point at Γ by folding the Brillouin Zone. These supercells are non-diagonal in general,[103] and we built them using the `yambopy` Python tool.[58] Note that we approximate the momentum $\bar{q}$ so that its vector coordinates are accommodable in reasonably small supercells. The second-order of the Taylor expansion of ε is:

$$\varepsilon^{st,(2)}_{\mu\bar{q}}(\omega) = \frac{\partial^2 \varepsilon^0}{\partial R^2_{\mu\bar{q}}} \Delta R^2_{\mu\bar{q}} \tag{3.8}$$

The expansion to finite temperature is done with a product of integrals over each phonon mode, and since the phonon wavefunctions are Gaussian, the integrals are analytic. Combined with the factor $\Delta R^2_{\mu\bar{q}}$, we obtain the thermal average of the squared displacement of the a quantum harmonic oscillator for each phonon mode, given by :

$$\sigma^2_{\mu\bar{q}}(T) = l^2_{\mu\bar{q}}(2n_{\mu\bar{q}}(T) + 1). \tag{3.9}$$

$n_{\mu\bar{q}}(T)$ is the Bose-Einstein occupation function, and $l^2_{\mu\bar{q}} = 1/(2M_{\mu\bar{q}}\Omega_{\mu\bar{q}})$ is the zero-temperature squared displacement (from now on we refer to phonon frequencies with capital Omega). In our case the reference mass is $M_{\mu\bar{q}} = \sum_s^{N_{ions}} M_s|\xi_s^{\mu\bar{q}}|^2$. More details on the derivation of this factor can be found in Ref. [104]. Finally the second-order correction to the full dielectric function due to the transitions assisted by a single phonon of momentum $\bar{q}$ is :

$$\varepsilon^{st,(2)}_{\bar{q}}(\omega) = \frac{1}{2}\sum_{\mu}\left[\sum_i^{N_{\bar{q}}} \frac{1}{2}\sum_j^{2} \left.\frac{\partial^2 \varepsilon_j^{(0)}(\omega)}{\partial R^2_{\mu\bar{q}}}\right|_{eq}\right] \sigma^2_{\mu\bar{q}} \tag{3.10}$$

where j is the polarization direction of the incoming light. We average over two orthogonal in-plane directions. The index i runs over the equivalent $\bar{q}$ points in the BZ where the exciton energies are minimal. For a perfect hBN crystal, $N_{\bar{q}} = 6$ but in our case, $N_{\bar{q}} = 4$. Finally the imaginary part of the dielectric function follows from Eqs. (3.5),(3.1) and (2.112) :

$$\mathrm{Im} \left.\frac{\partial^2 \varepsilon^{(0)}(\omega)}{\partial R^2_{\mu\bar{q}}}\right|_{eq} = \frac{8\pi}{N_k V}\sum_{\lambda'} \left.\frac{\partial^2 |T^{\lambda'}|^2}{\partial R^2_{\mu\bar{q}}}\right|_{eq} \mathrm{Im}\left\{\frac{1}{\omega - E^{\lambda'} + i\eta}\right\}. \tag{3.11}$$

At this point we can reintroduce the dependence on the phonon frequency coming from the energy conservation in perturbation theory, which was neglected above (more details can be found in Ref. [77]). Two terms appear, one coming from the process of phonon emission which is proportional to $1 + n_{\mu\bar{q}}$ and one from phonon absorption proportional to $n_{\mu\bar{q}}$. We have the transformation :

$$\frac{2n_{\mu\bar{q}}+1}{\omega - E^{\lambda'} + i\eta} \to \frac{n_{\mu\bar{q}}+1}{\omega - E^{\lambda'} - \Omega_{\mu\bar{q}} + i\eta} + \frac{n_{\mu\bar{q}}}{\omega - E^{\lambda'} + \Omega_{\mu\bar{q}} + i\eta} \tag{3.12}$$

At low temperature, $n_{\mu\bar{q}} \ll 1$ which means that absorbing a phonon is much less likely than emitting one. The final expression writes :

$$\varepsilon_{\bar{q}2}^{(2)}(\omega) = \frac{8\pi}{N_k V} \sum_{\lambda'} \left. \frac{\partial^2 |T^{\lambda'}|^2}{\partial R_{\mu\bar{q}}^2} \right|_{eq} l_{\mu\bar{q}}^2 \left[n_{\mu\bar{q}} + 1/2 \mp 1/2 \right] \delta(\omega - E^{\lambda'} \pm \Omega_{\mu\bar{q}}). \tag{3.13}$$

The upper (lower) sign refers to the process of phonon absorption (emission). One thing to note here is that we neglect the variation of the exciton energies induced by the coupling with phonon, which is an effect beyond second order derivative for indirect excitons, so we expect this renormalization to be minor.[105] Moreover we know that due to the approximations adopted in this work we will not be able to get the correct absolute position[30] of the exciton but only the relative position of indirect emission with respect to the direct one.

3.6. Luminescence results

In order to compute the luminescence spectra, we used the van Roosbroeck–Shockley relation from Eq. (2.123) combined with the expression of the dielectric function in Eq. (3.13). We simulate a crystal at low temperature, which we set at 55K in agreement with the experimental measurements. At this temperature, the phonon emission processes widely dominate the absorption ones and we have $n_{\mu\bar{q}} \ll 1$. Therefore we set these factors to zero in the numerator. We get a final expression for the luminescence as :

$$\begin{aligned} I(\omega) = \mathcal{D} R^{sp}(\omega) = \mathcal{D} \sum_{\mu,\bar{q}} \frac{\omega(\omega - 2\Omega_{\mu\bar{q}})^2}{\pi c^3} n_1(\omega) \sum_{\lambda'} \left. \frac{\partial^2 |T^{\lambda'}|^2}{\partial R_{\mu\bar{q}}^2} \right|_{\text{eq}} \\ \times \operatorname{Im} \left\{ \frac{1}{\omega - (E^{\lambda'} - \Omega_{\mu\bar{q}}) + i\eta} \right\} n_B(E_{\bar{q}}^{\lambda'}, T_{exc}) \end{aligned} \tag{3.14}$$

where $\mathcal{D}$ is a dimensional factor, $n_1(\omega)$ is the refractive index given by Eq. (2.122), $n_B(E_{\bar{q}}^{\lambda'}, T_{exc}) = e^{-(E^{\lambda'} - E^{min})/k_B T_{exc}}$ is the Boltzmann occupation for excitons where the energy difference is taken with the minimal exciton energy over the whole Brillouin Zone E^{min}. Except for a multiplicative factor, the formula for the luminescence is equivalent to the phonon-assisted absorption one, with the difference that excitons are weighted by an occupation factor. It means that the lowest valleys in the exciton dispersion will be populated by relaxed excitons, while the higher states will have exponentially decaying populations.

The excitonic temperature T_{exc} is higher than the lattice temperature because we consider a steady-state process in which the excitons do not thermalize, since they are constantly pumped by the laser. We obtained the value by fitting the experimental data of Ref. [27] which gave us the value of $T_{exc} = 105$ K for a lattice temperature of $T_L = 55$ K. The effect of temperature is also taken into account in the broadening parameter of the peaks with the Lorentzian model : $\eta = \Gamma_0 + aT + bB(T)$ where the values of the parameters can be found in Refs. [29, 106]. Another approximation we made is to compute the dipoles at the displaced configurations with the statically screened interaction W evaluated at the equilibrium configurations :

$$\frac{\partial^2 |T^{\lambda'}(W, L)|^2}{\partial R^2_{\mu\bar{q}}} \simeq \frac{\partial^2 |T^{\lambda'}(W(R = R_{eq}), L)|^2}{\partial R^2_{\mu\bar{q}}}. \tag{3.15}$$

It has been shown previously that this has negligible effects for the calculation of electron-phonon matrix elements,[107] and we verified that our results are not modified by this approximation.

Now comes the discussion about the choice of $\bar{q}$. For the pristine hBN crystal, the indirect electronic gap is between two points close to the K point and the M point. The usual approximation is to consider that the gap lies on the K point, and that the momentum that connects the two points is $\mathbf{q} = (\frac{1}{3}, -\frac{1}{6}, 0)$ and that the minimum of the exciton dispersion is also at this momentum. This approximation has been shown to produce reliable results in similar systems.[28, 29] This simplifies the construction of the supercells needed to accommodate the phonon modes at this **q**-vector. In our case, because of the symmetry breaking in the electronic dispersion, there are several indirect gaps which have a very similar energy, especially for low values of strain. This could lead to a broadening of the peaks in the luminescence spectra. In order to verify this hypothesis, we constructed the supercells which accommodate all the vectors corresponding to the transitions $\mathbf{M} - \mathbf{K}$, $\mathbf{M} - \mathbf{K}'$, $\mathbf{M}' - \mathbf{K}$, $\mathbf{M}' - \mathbf{K}'$. Then we performed a BSE calculation for all these non-diagonal supercells containing 24 displaced atoms and summed the dipoles. Because of the displacement of atoms, some symmetries are broken and the dark excitons which are folded at Γ acquire a finite dipole, hence contributing to the luminescence spectra if they are populated by the Boltzmann occupation function.

The resulting spectra for various values of strained are displayed in Fig. 3.9. First, we can see on the top plot that the equilibrium luminescence spectrum is quite well reproduced compared to experiment. At low values of strain, the excitons originating from the different $\mathbf{M}^{(\prime)} - \mathbf{K}^{(\prime)}$ transitions have a very close energy and therefore all of them contribute to the luminescence spectra as they are not suppressed by the Boltzmann function. These excitons scatter with phonons who also have their frequencies modified. These combined effects create a splitting of the peaks which increases with strain, materialized by the gray dashed lines. There is also a slight increase in the intensity of the S1 and S2 peaks, coming from scattering with LA and TA modes. At equilibrium, we found that the S3/S1 intensity ratio is ≈ 3.7 and it decreases down to ≈ 2.7 with strain. This result is in line with those of Léonard Schué in Ref. [96], however they found a ratio going down to ≈ 1

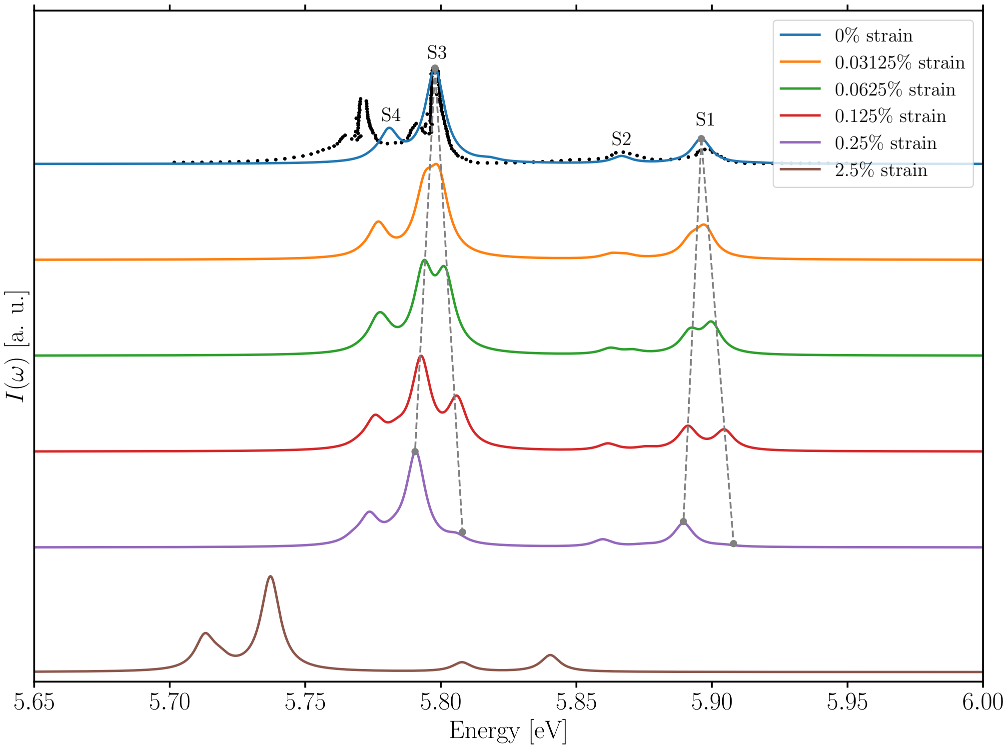

Figure 3.9. – Luminescence spectra for selected values of compressive strain. Plots are shifted vertically for clarity. On the top plot, experimental data from Ref. [25] is represented by the black dots. The spectra have been shifted to match the position of the indirect exciton at equilibrium, and compensate the numerical error of the GW approximation.[30] Dashed lines are a guide for the eye.

in their compressed samples.

This discrepancy could be explained by the lack of fine sampling of the exciton and phonon dispersions. Indeed with a larger density of states to scatter to, the intensity of some peaks could be increased even more. The differences could also come from experimental factors not accounted for in our simulation methods, such as surface effects or the fact that the strain field could be non-uniform and with an unknown direction, which we cannot reproduce with the uniaxial and homogeneous strain that we simulated.

Finally, for larger values of strain, the exciton energies split so much that the peaks coming from the higher one are suppressed by the Boltzmann function in the van Roosbroeck–Shockley relation. The spectrum thus acquires the same shape as the equilibrium one but translated to lower energies due to the closure of the indirect gap, and the change in the phonon frequencies. Note that the 2.5% value of strain is extreme and is probably out of reach in the experimental conditions we try to reproduce. The results are similar for the tensile strain.

Conclusion of the chapter

In this chapter, I presented our results about the electronic, phononic and optical properties of bulk hBN under uniaxial strain, both tensile and compressive, along the armchair direction. We observed a splitting of the exciton at Γ due to the breaking of the threefold rotational symmetry. This splitting could be measured in reflectivity experiments.[26] We also found that the direct excitons energies vary linearly with the applied strain, while the indirect exciton energies decrease both with compression and stretch. We were also able to evaluate the strain gauge factor, which was found to be similar to that of transition metal dichalcogenides. I presented a method to include the exciton-phonon coupling in the response function and hence in the optical spectra of the strained crystals. It is based on a finite-difference derivative approach and is well-suited for materials with a indirect and deep exciton dispersion minimum. The coupling of excitons and phonons is calculated only for a few momenta in the Brillouin Zone. Since this method requires the use of supercells, it is particularly adapted to the study of defects such as was done in Ref. [108]. We employed this method to compute the phonon-assisted luminescence spectrum and how it changes with strain. We found that at low strain, additional peaks appear in the spectra due to the breaking of the degeneracy between the different K and M points in the Brillouin Zone. These additional peaks decrease the intensity ratio between the acoustic- and the optical-phonon assisted transitions, in agreement with recent measurements. For large compressive strain we found that only one valley contributes to the luminescence, and the spectra return to a shape similar to the equilibrium one but shifted at lower energies. This prediction could be verified by means of luminescence measurements in highly strained hBN.[97]

Summary of Chapter 3

- The coupling between excitons and phonons was included in the second derivative of the response function with respect to the atomic displacements along phonon eigenvectors, in Sec. 3.5
- We evaluated this derivative numerically by building supercells and displacing the atoms along all phonon modes.
- We then computed the response function with a BSE calculation on the displaced configurations.
- We obtained the luminescence spectra *via* the van Roosbroeck–Shockley relation for several values of strain and compared our results to the experimental spectra in Sec. 3.6.

4. Ab initio exciton-phonon coupling

This Chapter is partly based on our publication Ref. [109]. Some of the text and figures contained in this Chapter are adapted from this reference.

Contents

4.1. Introduction

In recent years, single or few-layer materials have attracted a great deal of attention due to their peculiar properties, often different from their bulk counterparts. For example, MoS_2 undergoes an indirect-to-direct band gap transition when reducing its thickness to the monolayer limit.[110, 111] This transition was discovered thanks to the increase in the luminescence signal, since it is well-known that indirect materials tend to be poor light emitters due to higher-order processes mediating the electron-hole recombination. A similar band gap transition was also predicted for hBN.[99]

For many years it was not possible to measure the luminescence signal of a single hBN layer,[33] and this was attributed either to the increase of the exciton-exciton annihilation rate in low-dimensional structures[112, 113] or to other quenching mechanisms. However, recent experiments reported a photoluminescence signal from direct excitons in single-layer hexagonal Boron Nitride (mBN) epitaxially grown on Graphite, showing the existence of a fine two-peak structure.[1, 3] These experiments were later repeated using exfoliated hBN on a silicon oxide substrate,[2] where only one dominant peak was found. Very recently, a group achieved the technical prowess of measuring the cathodoluminescence signal of a monolayer of hBN grown on a Graphite substrate.[34] Their results have a very low signal-to-noise ratio, but it seems that only one peak appears. However care has to be taken since this article is still in the process of peer-reviewing. The various mBN spectra that appeared in the literature present notable differences which were attributed first to coupling with phonon modes and later to the presence of bubbles in the mBN structure. In addition, the first luminescence measurements of another polytype of BN with an AB stacking, the so-called Bernal Boron Nitride (bBN) was reported recently.[31, 32] These measurements seemed to show the coexistence of emission peaks from both direct and indirect excitons in the same spectrum.

From a theoretical point of view, mBN has been always considered a direct band gap materials in models,[114] while the nature of its gap in *ab initio* approaches depends on the approximation used in the calculations.[115, 116] Regarding bulk hBN, models and *ab initio* calculations agree on its nature as an indirect gap insulator.[12] For the intermediate situation, for few-layers hBN, the magnitude and nature of the quasiparticle band gap depends both on the number of layers and on the stacking order.[12, 116, 117]

In light of these results, we decided to investigate the luminescence of mBN using a novel approach that includes the coupling between excitons and phonons within an *ab initio* framework and allows for an accurate treatment of both direct and phonon-assisted peaks in the spectra. The motivation of this study is threefold. First, mBN could present both direct and indirect peaks in its luminescence spectra, which is an ideal test for our theory, while its well-known bulk counterpart provides an excellent benchmark. Second, the presence of new and partially unclear experiments on mBN makes the application of this new methodology interesting and timely. Third, a detailed study of the relation between the lattice structure and phonon and exciton dispersions could pave to way to an experimental tuning of the intensity of various features in the luminescence spectra.

At variance with older theoretical works on exciton-phonon coupling, where the values of the coupling matrix elements were taken as parameters, recent formulations focused on accurate *ab initio* numerical simulations, either tackling the exciton-phonon problem by means of finite-difference displacements in supercells as it was done in the previous chapter, or, more recently, by combining DFPT with BSE simulations, in order to avoid the need of large supercells.[118] In the first two sections of this chapter we put forward a formal derivation within MBPT which captures phonon mediated photoluminescence in a steady-state approximation, and combine it with DFPT to perform accurate *ab initio* numerical simulations in a single unit cell. The great advantage of this formulation is the possibility of integrating over exciton momenta in the full Brillouin Zone, thus calculating the renormalization of the direct peak induced by the indirect transitions. This is essential when studying an emission spectrum that may have competing direct and indirect peaks, such as the case investigated here. We test this method on the well-documented bulk hBN and then apply it to mBN, which constitute the main result of this Chapter. Finally, we present preliminary results on bBN.

4.2. Theory of the ab initio exciton-phonon coupling

In this section we present an *ab initio* approach to obtain the exciton-phonon coupling matrix elements, that goes beyond the finite-difference approach presented in Sec. 3.5. The great advantage of this formulation is the possibility to integrate over exciton momenta in the full Brillouin Zone and to obtain the coupling between all excitons and all phonon modes.

In this work in order to study optical response we start from an exciton-phonon Hamiltonian where excitons are independent quasi-particle, and the coupling with phonons acts as an interaction term between excitons mediated by phonons. This Hamiltonian can be assumed as a model [46, 119] or formally derived as it was by our collaborator Fulvio Paleari in his PhD thesis, [77] itself stemming from the theoretical work of Pierluigi Cudazzo published in Ref. [55]. In this approach, the electron-phonon interaction is included in the BSE kernel via a phonon propagator. The induced dynamical perturbation induced adds a term to the BSE kernel and it yields a general *dynamical* Bethe-Salpeter Equation :

$$\mathcal{L}(1234) = L(1234) + \int d5678\; L(1625)\; \tilde{\Xi}^D(5867)\; \mathcal{L}(7483) \tag{4.1}$$

where L is the two-particle propagator solution of the static BSE in Eq. (2.79). The kernel $\tilde{\Xi}^D$ has an additional dynamical term induced by the electron-phonon interaction. The dynamical kernel does not allow a direct inversion of the dynamical BSE since it depends self-consistently on L and cannot be written in terms of two times. Then, after a few approximations, the problem can be formally inverted and mapped onto an exciton-phonon Hamiltonian, which gives the exciton-phonon matrix elements. I refer the interested reader to Ref. [55, 77], where the rigorous derivation can be found.

In this thesis, I will present another way to derive the same exciton-phonon matrix elements, adapted from Ref. [118]. It uses first-order perturbation theory for the excitonic Hamiltonian, the perturbation being a displacement of atoms along phonon modes. It introduces an additional interaction term due to the electron-phonon coupling, from which the exciton-phonon matrix elements can be identified.
Note that another, more general approach exists in litterature. It consists in treating the electron-electron, the electron-phonon interactions and the external field on the same

footing,[54] which lifts some of the approximation we use, but it does not introduce relevant changes for the systems investigated here.

We consider a system with displacements from equilibrium positions $\boldsymbol{u}_{Ls}$ (L labels the unit cell and s the atom). We start from the DFT level and take the Taylor expansion of the Kohn-Sham potential, labelled as v_{eff} in Eq. (2.14), which we call V^{KS} here. The expansion around the equilibrium positions reads :

$$V^{KS}(\{\mathbf{u}_{Ls}\}) = V_0^{KS} + \sum_{Ls\alpha} \frac{\partial V^{KS}}{\partial \mathbf{u}_{Ls\alpha}} \mathbf{u}_{Ls\alpha} + \mathcal{O}(\{\mathbf{u}_{Ls}\}^2) \tag{4.2}$$

The electronic wave functions and eigenvalues of the perturbed system depend on the atomic displacements $\{\mathbf{u}_{Ls}\}$. To obtain their change in the perturbed system, we apply first-order perturbation theory by keeping terms linear in $\{\mathbf{u}_{Ls}\}$. To first order, the correction to the eigenvalues vanishes while the correction to the Kohn-Sham wave functions ψ_i (solutions of Eq. (2.10)) can be written as :

$$\delta \left|\psi_i\right\rangle = \sum_{j \neq i} \frac{\left\langle\psi_j\right| \Delta V \left|\psi_i\right\rangle}{\epsilon_i - \epsilon_j} \left|\psi_j\right\rangle, \qquad \text{with } \Delta V = \sum_{Ls\alpha} \frac{\partial V^{KS}}{\partial \mathbf{u}_{Ls}} \cdot \mathbf{u}_{Ls} \tag{4.3}$$

In the following, we use the tilde to label quantities of the perturbed system and write the perturbed wave function as :

$$\left|\tilde{\psi}_i\right\rangle = \left|\psi_i\right\rangle + \delta\left|\psi_i\right\rangle = \left|\psi_i\right\rangle + \sum_{j \neq i} \Delta_{ij} \left|\psi_j\right\rangle \tag{4.4}$$

with

$$\Delta_{ij} \equiv \frac{\left\langle\psi_j\right| \Delta V \left|\psi_i\right\rangle}{\epsilon_i - \epsilon_j} \tag{4.5}$$

We set ourselves in the Tamm-Dancoff approximation and we use the resonant Hamiltonian from Eq. (2.95) as the Hamiltonian of the unperturbed system $H \equiv H^{2p}(\{\boldsymbol{u}_{Ls}\} = 0)$. For the perturbed system, we have $\tilde{H} \equiv H^{2p}(\{\boldsymbol{u}_{Ls}\})$. The perturbed Hamiltonian matrix element is :

$$\tilde{H}_{\tilde{v}\tilde{c},\tilde{v}'\tilde{c}'} = \left\langle\tilde{v}\tilde{c}\right| \tilde{H} \left|\tilde{v}'\tilde{c}'\right\rangle = (\tilde{\epsilon}_c - \tilde{\epsilon}_v)\delta_{\tilde{v}\tilde{v}'}\delta_{\tilde{c}\tilde{c}'} + \tilde{\Xi}_{\tilde{v}\tilde{c}}^{\tilde{v}'\tilde{c}'} \tag{4.6}$$

where v, c refer to valence and conduction bands, respectively. The perturbed Bethe-Salpeter kernel is defined just as in Eq. (2.93), except that it is evaluated with the screened interaction of the perturbed system $\tilde{W}$, and its matrix elements are expressed in the perturbed basis.

Solving the BSE in Eq. (2.98) gives the exciton wave functions that we will name $|\lambda\rangle$

and energies E_λ :

$$\sum_{v',c'} H_{vc,v'c'} A_\lambda^{v'c'} = E_\lambda A_\lambda^{vc} \tag{4.7}$$

$$|\lambda\rangle = \sum_{vc} A_\lambda^{vc} |vc\rangle \tag{4.8}$$

To derive the exciton-phonon interaction, we project the perturbed BSE Hamiltonian onto the unperturbed basis set and keep only the terms to first-order in the phonon perturbation. By such a process, the terms that will arise and be different from the unperturbed BSE Hamiltonian will define the exciton-phonon interaction. One can show that to first order, the perturbed and unperturbed electronic energies coincide, so we will use $\tilde{\epsilon}_i = \epsilon_i$. The perturbed Hamiltonian in the unperturbed basis is :

$$\begin{aligned}\tilde{H}_{\lambda\lambda'} = \langle\lambda'|\,\tilde{H}\,|\lambda\rangle &= \sum_{\tilde{v}\tilde{c},\tilde{v}'\tilde{c}'} \langle\lambda'|\tilde{v}\tilde{c}\rangle\,\langle\tilde{v}\tilde{c}|\,\tilde{H}\,|\tilde{v}'\tilde{c}'\rangle\,\langle\tilde{v}'\tilde{c}'|\lambda\rangle \\ &= \sum_{vc,v'c'}\ \sum_{\tilde{v}\tilde{c},\tilde{v}'\tilde{c}'} \langle\lambda'|vc\rangle\,\langle vc|\tilde{v}\tilde{c}\rangle\,\langle\tilde{v}\tilde{c}|\,\tilde{H}\,|\tilde{v}'\tilde{c}'\rangle\,\langle\tilde{v}'\tilde{c}'|v'c'\rangle\,\langle v'c'|\lambda\rangle\end{aligned}$$

where we used the completeness relations of both basis sets, $\sum_{vc}|vc\rangle\langle vc| = \mathbb{1}$ and $\sum_{\tilde{v},\tilde{c}}|\tilde{v}\tilde{c}\rangle\langle\tilde{v}\tilde{c}| = \mathbb{1}$. By definition of the BSE wave functions $\langle v'c'|\lambda\rangle = A_\lambda^{v'c'}$, then we can write the above equation as :

$$\tilde{H}_{\lambda\lambda'} = \langle\lambda'|\,\tilde{H}\,|\lambda\rangle = \sum_{vc,v'c'} A_{\lambda'}^{vc*} A_\lambda^{v'c'} \times \left[\sum_{\tilde{v}\tilde{c},\tilde{v}'\tilde{c}'} \langle vc|\tilde{v}\tilde{c}\rangle\,\langle\tilde{v}\tilde{c}|\,\tilde{H}\,|\tilde{v}'\tilde{c}'\rangle\,\langle\tilde{v}'\tilde{c}'|v'c'\rangle\right] \tag{4.9}$$

The term inside the square brackets can be separated in two :

$$\begin{aligned}&\sum_{\tilde{v}\tilde{c},\tilde{v}'\tilde{c}'} \langle vc|\tilde{v}\tilde{c}\rangle\,\langle\tilde{v}\tilde{c}|\,\tilde{H}\,|\tilde{v}'\tilde{c}'\rangle\,\langle\tilde{v}'\tilde{c}'|v'c'\rangle = \sum_{\tilde{v}\tilde{c},\tilde{v}'\tilde{c}'} \langle vc|\tilde{v}\tilde{c}\rangle \left[(\tilde{\epsilon}_{\tilde{c}} - \tilde{\epsilon}_{\tilde{v}})\delta_{\tilde{v}\tilde{v}'}\delta_{\tilde{c}\tilde{c}'} + \tilde{\Xi}_{\tilde{v}\tilde{c}}^{\tilde{v}'\tilde{c}'}\right] \langle\tilde{v}'\tilde{c}'|v'c'\rangle \\ &= \sum_{\tilde{v}\tilde{c}} \langle vc|\tilde{v}\tilde{c}\rangle\,(\epsilon_{\tilde{c}} - \epsilon_{\tilde{v}})\,\langle\tilde{v}\tilde{c}|v'c'\rangle + \sum_{\tilde{v}\tilde{c},\tilde{v}'\tilde{c}'} \langle vc|\tilde{v}\tilde{c}\rangle\,\tilde{\Xi}_{\tilde{v}\tilde{c}}^{\tilde{v}'\tilde{c}'}\,\langle\tilde{v}'\tilde{c}'|v'c'\rangle\end{aligned}$$

We make the choice to approximate the perturbed kernel with the unperturbed one, $\tilde{\Xi}_{\tilde{v}\tilde{c}}^{\tilde{v}'\tilde{c}'} \approx \langle\tilde{v}\tilde{c}|\,\Xi\,|\tilde{v}'\tilde{c}'\rangle$, that is to say the effect of atomic displacements on the screened interaction can be neglected and $W \approx \tilde{W}$. This is the same approximation we took in Chapter 2 when we evaluated the response function by finite difference derivative.[86, 29, 28] With this approximation we have :

$$\sum_{\tilde{v}\tilde{c},\tilde{v}'\tilde{c}'} \langle vc|\tilde{v}\tilde{c}\rangle\,\tilde{\Xi}_{\tilde{v}\tilde{c}}^{\tilde{v}'\tilde{c}'}\,\langle\tilde{v}'\tilde{c}'|v'c'\rangle \approx \sum_{\tilde{v}\tilde{c},\tilde{v}'\tilde{c}'} \langle vc|\tilde{v}\tilde{c}\rangle\,\langle\tilde{v}\tilde{c}|\,\Xi\,|\tilde{v}'\tilde{c}'\rangle\,\langle\tilde{v}'\tilde{c}'|v'c'\rangle = \langle vc|\,\Xi\,|v'c'\rangle = \Xi_{vc}^{v'c'} \tag{4.10}$$

and thus the term in square brackets in Eq. (4.9) becomes

$$\sum_{\tilde{v}\tilde{c},\tilde{v}'\tilde{c}'} \langle vc|\tilde{v}\tilde{c}\rangle \langle \tilde{v}\tilde{c}|\, \tilde{H}\, |\tilde{v}'\tilde{c}'\rangle \langle \tilde{v}'\tilde{c}'|v'c'\rangle = \sum_{\tilde{v}\tilde{c}} \langle vc|\tilde{v}\tilde{c}\rangle \left(\epsilon_{\tilde{v}} - \epsilon_{\tilde{c}}\right) \langle \tilde{v}\tilde{c}|v'c'\rangle + \Xi_{vc}^{v'c'} \tag{4.11}$$

Next, we use Eq. (4.4) to expand $\sum_{\tilde{v}\tilde{c}} \langle vc|\tilde{v}\tilde{c}\rangle \left(\epsilon_{\tilde{c}} - \epsilon_{\tilde{v}}\right) \langle \tilde{v}\tilde{c}|v'c'\rangle$ to order $\mathcal{O}(\Delta)$. Since we work within the Tamm-Dancoff approximation and keep only the resonant part of the BSE Hamiltonian, only valence-valence and conduction-conduction phonon-mediated scattering are allowed, that is to say $\Delta_{vc} = \Delta_{cv} = 0$ where the operator Δ was defined in Eq. (4.5). Using Eq. (4.4) we get :

$$\begin{aligned}
\langle vc|\tilde{v}\tilde{c}\rangle = \langle v|\tilde{v}\rangle \langle c|\tilde{c}\rangle &= \left(\delta_{v\tilde{v}} + \sum_{v''\neq\tilde{v}} \Delta_{\tilde{v}v''}\delta_{vv''}\right)\left(\delta_{c\tilde{c}} + \sum_{c''\neq\tilde{c}} \Delta_{\tilde{c}c''}\delta_{cc''}\right) \\
&= \left(\delta_{v\tilde{v}}\delta_{c\tilde{c}} + \delta_{v\tilde{v}} \sum_{c''\neq\tilde{c}} \Delta_{\tilde{c}c''}\delta_{cc''} + \delta_{c\tilde{c}} \sum_{v''\neq\tilde{v}} \Delta_{\tilde{v}v''}\delta_{vv''}\right) + \mathcal{O}(\Delta^2)
\end{aligned} \tag{4.12}$$

and similarly

$$\langle \tilde{v}\tilde{c}|v'c'\rangle = \langle v'|\tilde{v}\rangle^* \langle c'|\tilde{c}\rangle^* = \left(\delta_{v'\tilde{v}}\delta_{c'\tilde{c}} + \delta_{v'\tilde{v}} \sum_{c''\neq\tilde{c}} \Delta^*_{\tilde{c}c''}\delta_{c'c''} + \delta_{c'\tilde{c}} \sum_{v''\neq\tilde{v}} \Delta^*_{\tilde{v}v''}\delta_{v'v''}\right) + \mathcal{O}(\Delta^2) \tag{4.13}$$

With these expressions, there are five first-order terms in $\sum_{\tilde{v}\tilde{c}} \langle vc|\tilde{v}\tilde{c}\rangle \left(\epsilon_{\tilde{c}} - \epsilon_{\tilde{v}}\right) \langle \tilde{v}\tilde{c}|v'c'\rangle$ that we can simplify using the Kronecker delta :

$$\begin{aligned}
&\sum_{\tilde{v}\tilde{c}} \langle vc|\tilde{v}\tilde{c}\rangle \left(\epsilon_{\tilde{c}} - \epsilon_{\tilde{v}}\right) \langle \tilde{v}\tilde{c}|v'c'\rangle \\
&\quad \approx (\epsilon_c - \epsilon_v)\delta_{vv'}\delta_{cc'} + \delta_{cc'} \sum_{\tilde{v}} (\epsilon_c - \epsilon_{\tilde{v}}) \sum_{v''\neq\tilde{v}} \left(\Delta^*_{\tilde{v}v''}\delta_{vv''}\delta_{v'\tilde{v}} + \Delta_{\tilde{v}v''}\delta_{v'v''}\delta_{v\tilde{v}}\right) \\
&\qquad + \delta_{vv'} \sum_{\tilde{c}} (\epsilon_{\tilde{c}} - \epsilon_v) \sum_{c''\neq\tilde{c}} \left(\Delta_{\tilde{c}c''}\delta_{cc''}\delta_{c'\tilde{c}} + \Delta^*_{\tilde{c}c''}\delta_{c'c''}\delta_{c\tilde{c}}\right) \\
&\quad = (\epsilon_c - \epsilon_v)\delta_{vv'}\delta_{cc'} + \delta_{cc'} \left[\sum_{v''\neq v'} (\epsilon_c - \epsilon_{v'})\Delta^*_{v'v''}\delta_{vv''} + \sum_{v''\neq v} (\epsilon_c - \epsilon_v)\Delta_{vv''}\delta_{v'v''}\right] \\
&\qquad + \delta_{vv'} \left[\sum_{c''\neq c'} (\epsilon_{c'} - \epsilon_v)\Delta_{c'c''}\delta_{cc''} + \sum_{c''\neq c} (\epsilon_c - \epsilon_v)\Delta^*_{cc''}\delta_{c'c''}\right] \\
&\quad = (\epsilon_c - \epsilon_v)\delta_{vv'}\delta_{cc'} + \delta_{cc'}(\epsilon_{v'} - \epsilon_v)\Delta_{vv'} + \delta_{vv'}(\epsilon_c - \epsilon_{c'})\Delta^*_{cc'}
\end{aligned} \tag{4.14}$$

where we used $\Delta_{ij} = -\Delta^*_{ji}$ to obtain the last line. Finally, the perturbed Hamiltonian in the excitonic basis in Eq. (4.9) becomes :

$$\begin{aligned}\tilde{H}_{\lambda\lambda'} &= \sum_{vc,v'c'} A^{vc*}_{\lambda'} A^{v'c'}_{\lambda} \times \left\{ \left[(\epsilon_c - \epsilon_v)\delta_{vv'}\delta_{cc'} + \Xi^{v'c'}_{vc} \right] + \delta_{cc'}(\epsilon_{v'} - \epsilon_v)\Delta_{vv'} + \delta_{vv'}(\epsilon_c - \epsilon_{c'})\Delta^*_{cc'} \right\} \\ &= E_{\lambda'}\delta_{\lambda\lambda'} + \sum_{vc,v'c'} A^{vc*}_{\lambda'} A^{v'c'}_{\lambda} \cdot \left(\delta_{cc'}(\epsilon_{v'} - \epsilon_v)\Delta_{vv'} + \delta_{vv'}(\epsilon_c - \epsilon_{c'})\Delta^*_{cc'} \right)\end{aligned} \tag{4.15}$$

where we use the fact that the unperturbed Hamiltonian is diagonal in the excitonic space:

$$E_{\lambda'}\delta_{\lambda\lambda'} = \sum_{vc,v'c'} A^{vc*}_{\lambda'} A^{v'c'}_{\lambda} \times \left((\epsilon_c - \epsilon_v)\delta_{vv'}\delta_{cc'} + \Xi^{v'c'}_{vc} \right). \tag{4.16}$$

Therefore, the first term in the second line of Eq. (4.15) is the unperturbed Hamiltonian, while the second term is the exciton-phonon interaction,

$$\tilde{H}_{\text{exc-ph}} = \sum_{vc,v'c'} A^{vc*}_{\lambda'} A^{v'c'}_{\lambda} \cdot \left(\delta_{cc'}(\epsilon_{v'} - \epsilon_v)\Delta_{vv'} + \delta_{vv'}(\epsilon_c - \epsilon_{c'})\Delta^*_{cc'} \right). \tag{4.17}$$

To obtain the final result, we reintroduce the periodicity of the Kohn-Sham states stemming from Bloch theorem :

$$|\phi_i\rangle \rightarrow |\phi_{n\mathbf{k}}\rangle \tag{4.18}$$

and the transition basis set for an exciton with center of mass momentum $\mathbf{Q}$ is $|vc\rangle = |v\mathbf{k}_v, c\mathbf{k}_c\rangle = |v\mathbf{k}_v, c\mathbf{k}_v + \mathbf{Q}\rangle$. We write the change in potential due to atomic displacements in second quantization using the phonon normal coordinates :

$$\Delta V = \sum_{\mu\mathbf{q}} \sqrt{\frac{1}{2\Omega_{\mu\mathbf{q}}}} \partial_{\mu\mathbf{q}} V^{KS} (\hat{b}_{\mu\mathbf{q}} + \hat{b}^{\dagger}_{\mu-\mathbf{q}}) \tag{4.19}$$

where the operator $\partial_{\mu\mathbf{q}}$ should be understood as the derivative with respect to a displacement $R_{\mu\mathbf{q}}$ along a phonon mode μ at momentum $\mathbf{q}$. Then the Δ_{ij} describing the transition from i-th to j-th state becomes :

$$\Delta_{n\mathbf{k}n'\mathbf{k}'} = \frac{\langle n'\mathbf{k}' | \Delta V | n\mathbf{k}\rangle}{\epsilon_{n\mathbf{k}} - \epsilon_{n'\mathbf{k}'}} = \sum_{\mu\mathbf{q}} \frac{g_{nn'\mu}(\mathbf{k}, \mathbf{q})\delta(\mathbf{k}' - \mathbf{k} - \mathbf{q})}{\epsilon_{n\mathbf{k}} - \epsilon_{n'\mathbf{k}'}} (\hat{b}_{\mu\mathbf{q}} + \hat{b}^{\dagger}_{\mu-\mathbf{q}}) \tag{4.20}$$

where $g_{nn'\mu}(\mathbf{k}, \mathbf{q})$ are the electron-phonon matrix elements defined in Eq. (2.142), namely the probability amplitude for an electron in band n with crystal momentum $\mathbf{k}$ to transition to a final state in band n' and momentum $\mathbf{k}' = \mathbf{k} + \mathbf{q}$ by absorbing or emitting a phonon with mode index μ and wave vector $\mathbf{q}$. The slight difference with Eq. (2.142) is that we change the arguments to have a more compact form : the first argument is the momentum of the initial state and the second argument is the phonon momentum.

To proceed further we have to make on additional approximation on the nature of excitons : they are considered as independent bosons. This way, we can define a bosonic

Hamiltonian for excitons as :

$$H_{\text{exc}} = \sum_{\lambda} E_{\lambda}(\mathbf{Q})\hat{a}^{\dagger}_{\lambda\mathbf{Q}}\hat{a}_{\lambda\mathbf{Q}} \tag{4.21}$$

where $\hat{a}^{\dagger}_{\lambda\mathbf{Q}}, \hat{a}_{\lambda\mathbf{Q}}$ are the creation/annihilation operators for an exciton λ with center-of-mass momentum $\mathbf{Q}$ and energy $E_{\lambda}(\mathbf{Q})$. The full Hamiltonian also includes the phonon term, which is ignored here without loss of generality since it is only an additive constant. The bosonic approximation for excitons ignores the fact that excitons are a pair of two bound fermions, this is why it works best at low exciton density so that the exciton are weakly interacting. It has been shown to correctly reproduce several experimental results.[29, 46] However, there are theoretical evidence that the fermionic character of excitons cannot always be neglected.[120] Using this approximation we rewrite the exciton-phonon interaction from Eq. (4.17) in second quantization :

$$\tilde{H}_{\text{exc-ph}} = \sum_{\lambda\lambda'\mu,\mathbf{Qq}} \mathcal{G}^{\mu}_{\lambda\lambda'}(\mathbf{Q},\mathbf{q})\hat{a}^{\dagger}_{\lambda\mathbf{Q}+\mathbf{q}}\hat{a}_{\lambda'\mathbf{Q}}(\hat{b}_{\mu\mathbf{q}} + \hat{b}^{\dagger}_{\mu-\mathbf{q}}). \tag{4.22}$$

where we defined the exciton-phonon matrix elements as :

$$\begin{aligned}\mathcal{G}^{\mu}_{\lambda\lambda'}(\mathbf{Q},\mathbf{q}) = &\sum_{\substack{vcv'c'\\ \mathbf{k}_v\mathbf{k}_c\mathbf{k}'_{v'}\mathbf{k}'_{c'}}} A_{\lambda\mathbf{Q}+\mathbf{q}}(v\mathbf{k}_v, c\mathbf{k}_c)A^{*}_{\lambda'\mathbf{Q}}(v'\mathbf{k}'_{v'}, c'\mathbf{k}'_{c'})\\ &\times\left[\delta_{vv'}g_{c'c\mu}(\mathbf{k}'_{c'},\mathbf{q})\delta(\mathbf{k}_c - \mathbf{k}'_{c'} - \mathbf{q}) - \delta_{cc'}g_{vv'\mu}(\mathbf{k}_v,\mathbf{q})\delta(\mathbf{k}'_{v'} - \mathbf{k}_v - \mathbf{q})\right].\end{aligned} \tag{4.23}$$

Let us make momentum conservation explicit to obtain the final expression. The exciton-phonon coupling constant $\mathcal{G}_{\lambda\lambda'\mu}(\mathbf{Q},\mathbf{q})$ is the probability amplitude for scattering from an exciton with band index λ with center-of-mass momentum $\mathbf{Q}+\mathbf{q}$ to an exciton with band index λ' and center-of-mass momentum $\mathbf{Q}$. This convention will be clarified later. Since $A_{\lambda\mathbf{Q}}(v\mathbf{k}_v, c\mathbf{k}_c) \neq 0$ only for $\mathbf{k}_c - \mathbf{k}_v = \mathbf{Q}$, in Eq. (4.23) we can impose three constraints : $\mathbf{k}_c - \mathbf{k}_v = \mathbf{Q}$, $\mathbf{k}'_c - \mathbf{k}'_v = \mathbf{Q}+\mathbf{q}$ and $\mathbf{k}'_c - \mathbf{k}_c = \mathbf{q}$ (or $\mathbf{k}'_v - \mathbf{k}_v = \mathbf{q}$). As a consequence, we drop three $\mathbf{k}$-point BZ summations and the final result for the exciton-phonon matrix element for a given exciton momentum $\mathbf{Q}$ and phonon momentum $\mathbf{q}$ is :

$$\begin{aligned}&\mathcal{G}^{\mu}_{\lambda\lambda'}(\mathbf{Q},\mathbf{q})\\ &= \sum_{\mathbf{k}}\left[\sum_{vcc'} A_{\lambda\mathbf{Q}+\mathbf{q}}(v\mathbf{k}, c\mathbf{k}+\mathbf{Q}+\mathbf{q})A^{*}_{\lambda'\mathbf{Q}}(v\mathbf{k}, c'\mathbf{k}+\mathbf{Q})g_{c'c\mu}(\mathbf{k}+\mathbf{Q}+\mathbf{q}, -\mathbf{q})\right.\\ &\qquad\left. - \sum_{cvv'} A_{\lambda\mathbf{Q}+\mathbf{q}}(v\mathbf{k}-\mathbf{q}, c\mathbf{k}+\mathbf{Q})A^{*}_{\lambda'\mathbf{Q}}(v'\mathbf{k}, c\mathbf{k}+\mathbf{Q})g_{vv'\mu}(\mathbf{k}-\mathbf{q},\mathbf{q})\right].\end{aligned} \tag{4.24}$$

This is the general expression which was implemented in the `yambo` code. This expression is made of two contributions relative to the coupling of phonons with either the electron in the conduction band or the hole in the valence band constituting the exciton. It corresponds to a rotation of the electron-phonon coupling in the exciton basis. This basis shifts the picture from electrons and holes scattering with phonons to transitions between excitonic states mediated by phonons.

This formula allows to compute various quantities depending on the exciton-phonon matrix elements, such as the exciton lifetimes or more interestingly for us, the response functions including phonon-assisted transitions. Then from the optical response function we will obtain a formula for the luminescence intensity.

4.3. Phonon-assisted response function

Now we can proceed to the solution of the exciton-phonon Hamiltonian. A direct diagonalization is out of reach because the transitions at different $\mathbf{Q}$ are mixed by the electron-phonon scattering, therefore the dimension of the Hilbert space becomes too large. Hence we will make use of MBPT to find an approximate solution to Eq. (4.22).

We chose an approach that consists in taking the electron-phonon interaction only up to first order. This way, we define the two-particle propagator with a first-order dynamical correction $L^{(1)}$ as the solution of Eq. (4.1), obtained by replacing $\mathcal{L}$ on the right hand side of Eq. 4.1 by the static L :

$$L^{(1)}(1234) = L(1234) + \int d5678 \; L(1625) \, \tilde{\Xi}(5867) \, L(7483) \tag{4.25}$$

where $\tilde{\Xi}$ is the kernel perturbed by first-order electron-phonon interaction, the same introduced in the above section in Eq. (4.6). With this equation can consider only interaction mediated with a single phonon. Extension to multiple-phonon scattering exists in literature,[119] but the present formulation is the first order of a cumulant expansion and its generalization to coupling with phonons at all orders is straightforward.[55]
Using the relation Eq. (2.84), we can obtain the response function in the excitonic basis in terms of one frequency (or two times), including the first-order correction due to exciton-phonon coupling :

$$\chi^{(1)}_{\lambda\lambda'}(\omega) = \chi_{\lambda\lambda'}(\omega) + \chi_{\lambda}(\omega) \, \Pi^{\text{excp-ph}}_{\lambda\lambda'}(\omega) \, \chi_{\lambda'}(\omega) \tag{4.26}$$

where we used the short-hand notation $\chi_\lambda(\omega) = \chi_{\lambda\lambda'}(\omega)\delta_{\lambda\lambda'}$. On the right hand side, the quantity $\Pi^{\text{excp-ph}}_{\lambda\lambda'}(\omega)$ is the exciton self-energy describing dynamical effects induced by the electron-phonon interaction. We will refer to it as *exciton-phonon self-energy*. It can be computed starting from the exciton-phonon Hamiltonian Eq. 4.17 in MBPT[121] in a similar way as for the electron-phonon case.[66] Owing to the fact that we consider the first order only in exciton-phonon scattering, we will have a self-energy similar to the Fan-Migdal one for the electron-phonon problem : $\Pi^{\text{excp-ph}} = \mathcal{G}^2 DL$ where the exciton propagator L replaces the electron one, D is the phonon propagator and $\mathcal{G}$ are the exciton-phonon matrix elements derived in the previous section given by Eq. (4.24).

Keeping only the first order dynamical correction allows scattering with only one

phonon at a time, but this scattering can be re-summed at higher order solving the Dyson equation with a dynamical self-energy, that allows to formally write two different ways of summing contributions to infinite orders, hence scattering with any number of phonons. The first one is to take a Dyson equation $\chi^D = \chi + \chi\Pi^{\text{excp-ph}}\chi$ which corresponds to a partial re-summation of the general Eq. (4.1).[122] It will yield the correction to the exciton energies due to coupling with phonons but will fail to describe the phonon satellites in the optical spectra, just as the PES satellites given by the GW approximation are inaccurate. Another infinite summation is the cumulant expansion $\chi_C = \chi e^C$ with the cumulant coefficient of the form $C_\lambda(t) = \int dt \Pi^{\text{excp-ph}}_{\lambda\lambda}(t)e^{iE_\lambda t}$, determined by the diagonal components of the self-energy.[55] The cumulant ansatz is able to capture the physics giving rise to phonon satellites.
Notice that the first order of these two summations is identical and is given by Eq. (4.26). It is the one we use for the rest of this thesis. We will focus on the description of the satellite structures in optical spectra and neglect the corrections to exciton energies. The exciton-phonon self-energy writes :

$$\Pi^{\text{excp-ph}}_{\lambda\lambda'}(\mathbf{Q},\omega) = \frac{1}{N_q}\sum_{\mu\beta\mathbf{q}} \mathcal{G}^{\mu}_{\beta\lambda}(\mathbf{Q},\mathbf{q})\mathcal{G}^{\mu*}_{\beta\lambda'}(\mathbf{Q},\mathbf{q}) \times \left[\frac{1-n_\beta(\mathbf{Q}+\mathbf{q})+n_{\mathbf{q}\mu}}{\omega - E_{\mathbf{Q}+\mathbf{q},\beta} - \Omega_{\mathbf{q}\mu} - i\eta} + \frac{n_\beta(\mathbf{Q}+\mathbf{q})+n_{\mathbf{q}\mu}}{\omega - E_{\mathbf{Q}+\mathbf{q},\beta} + \Omega_{\mathbf{q}\mu} - i\eta}\right] \tag{4.27}$$

where N_q is the number of q-points summed over in the Brillouin Zone, $\Omega_{\mathbf{q}\mu}$ is the frequency of phonon mode μ at momentum $\mathbf{q}$, $n_{\mathbf{q}\mu}$ and $n_\beta(\mathbf{Q})$ are the temperature-dependent occupation factors for phonons and excitons, respectively. The imaginary infinitesimal $-i\eta$ comes from the analytic continuation in the Matsubara formalism for finite-temperature extension.[121] From here on, we label β the finite-momentum, lowest lying excitons states that are populated. The internal sum over β excitons includes every possible exciton level $E_{\mathbf{Q}+\mathbf{q},\beta}$ that can be connected to the external exciton levels $E_{\mathbf{Q},\lambda}$ by emitting or absorbing one phonon with frequency $\Omega_{\mathbf{q}\mu}$.

Since we are interested in optical properties, only excitons at zero momentum $\mathbf{Q} = 0$ are involved in the response functions, therefore we specialize the self-energy only for $\mathbf{Q} = 0$. To simulate the process of luminescence, we assume that the sample is constantly pumped with a laser and that there is a quasi-equilibrium population of excited carriers. In the excitonic picture, it means that the minima of the exciton dispersion are populated. When these minima are at indirect momenta, the process of light emission will start from an exciton β at finite momentum $\mathbf{q}$ that will be scattered by a phonon with the same momentum $\mathbf{q}$ and frequency $\Omega_\mathbf{q}$ into a direct exciton λ at $\mathbf{Q} = 0$. This direct exciton is allowed to recombine radiatively but it is a virtual, intermediate state. The frequency of the emitted light will be $\hbar\omega_{PL} = \hbar E_{\mathbf{q}\beta} \pm \hbar\Omega_{\mathbf{q}\mu}$. This allows us to simplify the expression of the exciton-phonon matrix elements in Eq. (4.24) as $\mathcal{G}^{\mu}_{\lambda\lambda'}(\mathbf{Q}=0,\mathbf{q}) = \mathcal{G}^{\mu}_{\lambda\lambda'}(\mathbf{q})$. Then, we make two approximations to compute the self-energy in Eq. (4.27). The first one is to neglect the excitonic occupations n_β compared to the phonon ones $n_{\mathbf{q}\mu}$. This is realistic for an equilibrium and even for the quasi-equilibrium situation we are interested in (see Supplemental Materials of Ref. [25] for an estimation of the excitonic density in hBN). The second is to use only the diagonal components of the self-energy. This means that an exciton λ that scatters with a phonon $\mu\mathbf{q}$ can only end up in an excitonic state of the same branch λ. In our case this approximation is valid because for luminescence we are only interested in the lowest excitons at finite momentum, that are not degenerate. In the general case one has to take into account the off-diagonal terms that are also responsible for the asymmetric Lorentzian shape of the excitonic peaks in the spectrum.[41] The simplified expression for the self-energy reads :

$$\begin{aligned}\Pi^{\text{excp-ph}}_{\lambda}(\mathbf{Q}=0,\omega) = \frac{1}{N_q}\sum_{\mu\beta\mathbf{q}} |\mathcal{G}^{\mu}_{\beta\lambda}(\mathbf{q})|^2 \\ \times\left[\frac{1+n_{\mathbf{q}\mu}}{\omega - E_{\mathbf{q}\beta} - \Omega_{\mathbf{q}\mu} - i\eta} + \frac{n_{\mathbf{q}\mu}}{\omega - E_{\mathbf{q}\beta} + \Omega_{\mathbf{q}\mu} - i\eta}\right].\end{aligned} \tag{4.28}$$

Plugging Eq. (4.28) in Eq. (4.26), we obtain for the diagonal case :

$$\chi^{(1)}_{\lambda}(\omega) = \frac{|T^{\lambda}|^2(1-Z_{\lambda})}{\omega - E_{\lambda} + i\eta} + \frac{|T^{\lambda}|^2}{N_q}\sum_{\mu\beta\mathbf{q}} \frac{|\mathcal{G}^{\mu}_{\beta\lambda}(\mathbf{q})|^2}{(E_{\mathbf{q}\beta} - E_{\lambda} \pm \Omega_{\mathbf{q}\mu})^2} \frac{1/2 \pm 1/2 + n_{\mathbf{q}\mu}}{\omega - E_{\mathbf{q}\beta} \mp \Omega_{\mathbf{q}\mu} - i\eta} \tag{4.29}$$

where the upper (lower) sign refer to phonon emission (absorption). The above expression contains two terms : the first one describes the response coming from direct transitions. Its weight is reduced by the renormalization factor Z_{λ} compared to the static case. The second term gives the phonon satellites coming from transitions assisted by the absorption or emission of a single phonon. They appear at the energy of the finite-momentum excitons plus or minus on phonon frequency $E_{\mathbf{q}\beta} \pm \Omega_{\mathbf{q}\mu}$. The renormalization factor Z_{λ} is given by :

$$Z_{\lambda} = -\left.\frac{\partial \Pi^{\text{excp-ph}}_{\lambda\lambda}(\omega)}{\partial\omega}\right|_{\omega=E_{\lambda}} \tag{4.30}$$

$$= \frac{1}{N_q}\sum_{\mu\beta\mathbf{q}} |\mathcal{G}^{\mu}_{\beta\mu}(\mathbf{q})|^2 \left[\frac{n_{\mathbf{q}\mu}+1}{(E_{\mathbf{q}\beta} - E_{\lambda} + \Omega_{\mathbf{q}\mu})^2} + \frac{n_{\mathbf{q}\mu}}{(E_{\mathbf{q}\beta} - E_{\lambda} - \Omega_{\mathbf{q}\mu})^2}\right] \tag{4.31}$$

It is the derivative of the self-energy with respect to incoming light frequency. It is a measure of how much weight is transferred from the direct peak to the satellites structures in the optical spectra when including the exciton-phonon coupling. Notice that there is a divergence when the phonon frequency is resonant with the exciton energy difference in the denominators. This unphysical behavior is an artifact of the finite-order perturbation theory.[40] If higher order terms are included, as in the cumulant expansion for instance, then a correction to the exciton energies and a broadening enter then denominators, which removes the divergence. This fictitious divergence could be particularly important for the material studied in this Chapter, mBN. In fact one of the experimental interpretation is that a phonon satellite caused by a transition between two zero-momentum excitons is visible in the photoluminescence spectrum of mBN. Hence we have to take special care when performing the q integration around Γ. To avoid divergences, we excluded the three acoustic modes with zero frequency at Γ in the sum over phonon modes.[1] Moreover to have a precise description of the phonon and exciton dispersions at small momentum, we used a double-grid scheme as explained in Appendix E.

Now we use Eq. (2.112) to get the imaginary part of the macroscopic dielectric function Eq. (4.29). Then we can derive a formula for the luminescence intensity using the van Roosbroeck–Shockley relations from Eqs. (2.121) and (2.123). This formula will include both the direct and the phonon assisted emission terms in the form :

$$R^{sp}(\omega) = R_0^{sp}(\omega) + \frac{1}{N_q}\sum_{\mathbf{q}\mu} R^{sp}_{\mathbf{q}\mu}(\omega) \tag{4.32}$$

where $R_0^{sp}(\omega)$ is the spontaneous emission rate for direct transitions only given by Eq. (2.121) and the second term includes the phonon-assisted transition is given by Eq. (2.123). Note that here the refractive index entering the two term $n_1(\omega)$ can be excellently approximated by Eq. (2.122) with just the static BSE result for ε^{exc}. Our final luminescence intensity formula up to a multiplicative constant reads :

$$\begin{aligned} I(\omega) = \mathcal{D}R^{sp}(\omega) = \mathcal{D}\,\mathrm{Im}\sum_{\lambda}|T^{\lambda}|^2 \Bigg\{ \omega^3 n_1(\omega)\frac{1-Z_\lambda}{\omega - E_\lambda + i\eta}\, e^{-\frac{E_\lambda - E_{min}}{k_B T_{exc}}} \\ + \frac{1}{N_q}\sum_{\mu\beta\mathbf{q}} \omega(\omega \mp 2\Omega_{\mathbf{q}\mu})^2 n_1(\omega)\frac{|\mathcal{G}^{\mu}_{\beta\lambda}(\mathbf{q})|^2}{(E_{\mathbf{q}\beta} - E_\lambda \pm \Omega_{\mathbf{q}\mu})^2}\frac{1/2 \pm 1/2 + n_{\mathbf{q}\mu}}{\omega - E_{\mathbf{q}\beta} \pm \Omega_{\mathbf{q}\mu} - i\eta}\, e^{\frac{E_{\mathbf{q}\beta} - E_{min}}{k_B T_{exc}}} \Bigg\} \end{aligned} \tag{4.33}$$

where $\mathcal{D}$ is a dimensional factor, $n_1(\omega)$ is the refractive index. Notice that the excitonic occupation that appears in the luminescence formula cannot be disregarded as in the self-energy, because fundamentally it gives the weight of the indirect transitions. We use a Boltzmann occupation function whose parameters are E_{min}, the minimum of the exciton dispersion and T_{exc}, the effective excitonic temperature. The latter is the only parameter in the whole process that needs to be fitted and we estimated it from the experimental measurements of Ref. [27]. For a lattice temperature of 10 K, the fit gives an excitonic temperature of $T_{exc} = 24$ K. The Boltzmann function for excitons is an approximation of the Bose-Einstein assumption that we made earlier, but it is valid for low excitonic density and reproduces correctly the experimental exponential decay of the phonon satellite peaks.

In this thesis we also tried to use an occupation factor made out of the single-particle fermionic occupations rotated in the exciton basis, just as it is done in Refs. [28, 123, 108], with an occupation function given by $n_\lambda = \sum_{cv\mathbf{k}} \langle\lambda|cv\mathbf{k}\rangle\, f_{c\mathbf{k}}(1 - f_{v\mathbf{k}})\,\langle cv\mathbf{k}|\lambda\rangle$,

---

[1] Notice that the electron-phonon coupling for acoustic modes goes to zero for $\mathbf{q} \to 0$, and so do the corresponding exciton-phonon coupling.

where f is the Fermi-Dirac function. However it gives rise to unphysical occupations as can be seen in Fig. 4.1 for three different BN nanostructures, namely mBN, hBN and bBN. Indeed, the lowest excitonic state is populated, but so are the higher states coming from the same transitions, that are the analogous of the Wannier exciton's excited states. Hence we stuck to the Boltzmann occupation instead of that derived from non-equilibrium Green's functions.

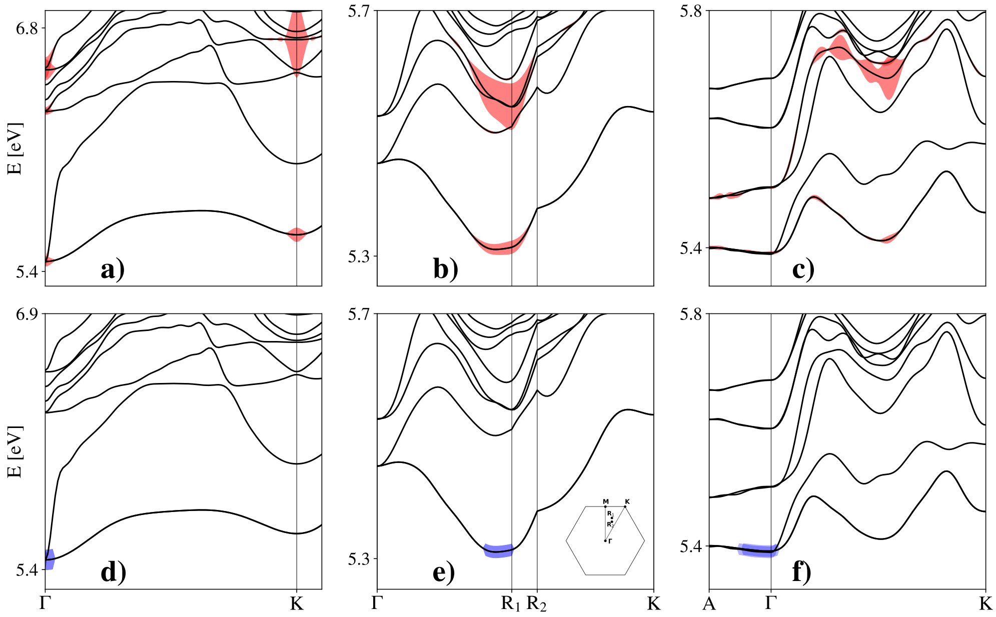

Figure 4.1. – Comparison of Boltzmann (blue areas) and quasi-Fermi (red areas) excitonic occupations for mBN (first column), hBN (second column) and bBN (third column). See main text for the definition of the occupation functions and section 4.5.1 for the definition of the R_1 and R_2 points. The black lines are the Fourier interpolation of exciton dispersions, calculated at the G_0W_0+BSE level.

The final expression for luminescence intensity Eq. (4.33) is to be compared with the one obtained with the finite difference method in Chapter 2, Eq. (3.14). Unlike the previous method where only the indirect transitions were included, in the present formula we have both the term coming from direct transitions and the term related to phonon satellites. The major theoretical advance here is that the renormalization factor from Eq. (4.31) allows to compare the relative intensities of the direct and the satellite peaks. Besides, the satellite weight denominators include the addition or removal of the phonon frequency not present in the static approximation of Eq. (3.14). Finally, thanks to this *ab initio* formulation we can perform the whole workflow necessary to evaluate Eq. (4.33) in the unit cell, which is also an improvement with respect to the previous method.

4.4. Excitons in mBN and exciton-phonon coupling

In this section we will apply the theoretical development presented in the two previous sections to the case of monolayer hBN. We will first present its electronic and excitonic properties then we will include phonons and their coupling with excitons.

4.4.1. Excitonic properties of a monolayer of hexagonal Boron Nitride

The electronic and optical properties of monolayer hexagonal Boron Nitride (mBN) have been the subject of numerous studies using both *ab initio* and semi-empirical methods.[114] Within DFT, with the LDA exchange-correlation functionals, mBN is a direct band gap material at high-symmetry point K, but the G_0W_0 corrections change its gap from direct to indirect, going from K to Γ.[115] We verified that the system remains indirect even at the semi-self-consistent "eigenvalue-GW" level (evGW). We plot the electronic band structure in Fig. 4.2 at different levels of theory : DFT within the LDA, G_0W_0 and evG_4W_4. The latter means that we iterated the Hedin's equation in the GW approximation four times, modifying only the poles of G at every iteration.[124] This process is compensating the lack of higher order correction of the G_0W_0 approximation and usually improves the agreement with experiments regarding the bandgap values.[125] In mBN the indirect gap is due to the presence of nearly-free electron states at Γ. In

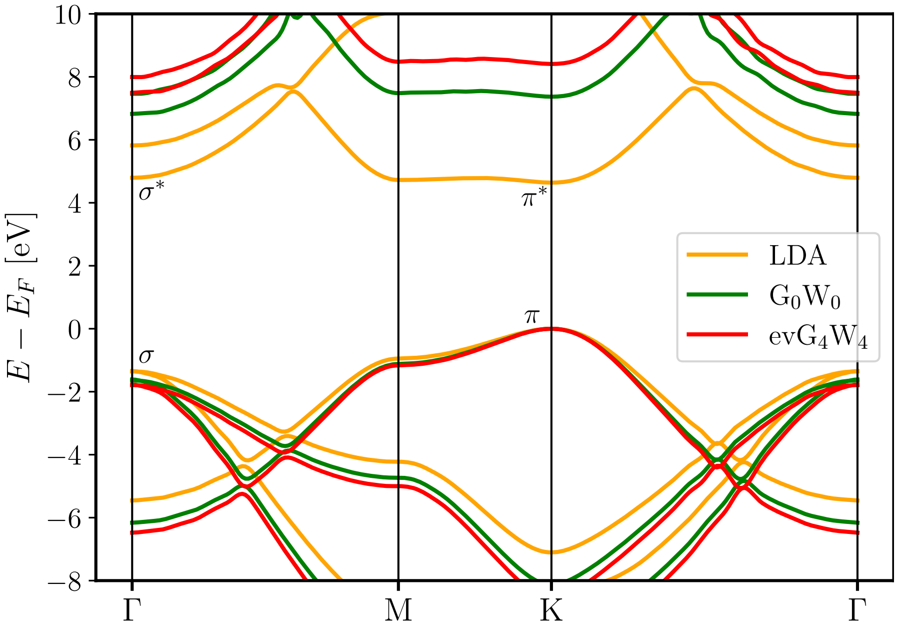

Figure 4.2. – Electronic bands of freestanding monolayer BN with different levels of theory : DFT (orange), G_0W_0 (green) and evG_4W_4 (red)

fact, the GW self-energy does not correct the σ^*-like states at Γ as much as the π^*-like states around K and M and this makes the system indirect. The nearly-free electron states have been investigated in the past in BN nanotubes and mBN,[126, 127] but only at the independent-particles, DFT level. They may provide a possible mechanism for luminescence quenching.[33]

Despite the presence of these states at Γ, the optical properties of BN-based systems are actually dictated by the π bands around K and M, and this remains true for mBN. The optical spectrum of mBN is characterized by a strong doubly degenerate excitonic peak of symmetry E at about 6 eV. Exciton dispersions have been reported in several articles.[128, 129, 12] In Fig. 4.3 we also report our calculated dispersion along selected high-symmetry lines, starting both from the quasiparticle band structure and the DFT one plus a scissor operator. The scissor shift is chosen in such a way that the lowest exciton energy at $\mathbf{Q} = 0$ matches the one obtained starting from the GW quasiparticle band structure. Our exciton dispersion compares well with previously publicated results.[129, 12]

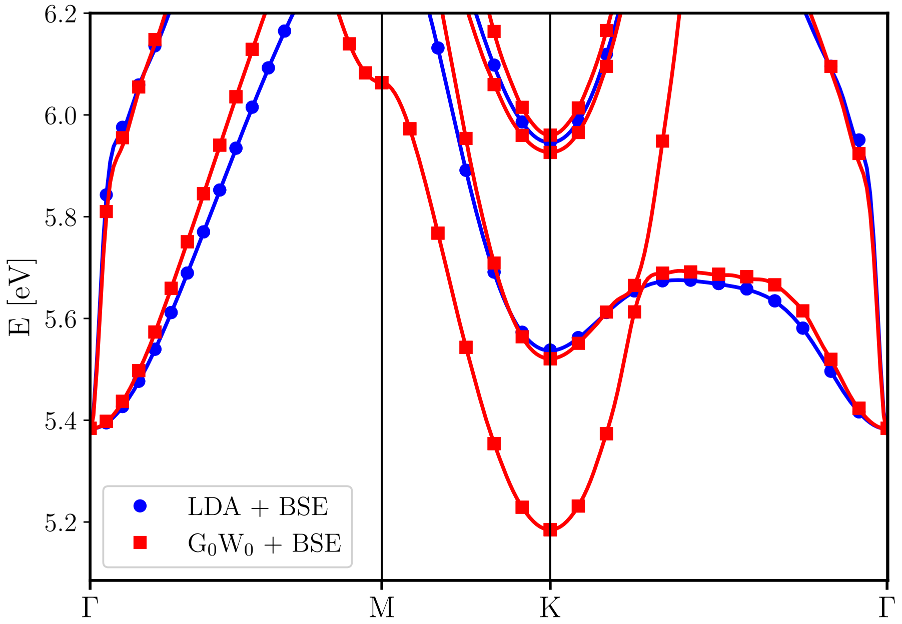

Figure 4.3. – Calculated exciton dispersion for monolayer hBN, starting from either the DFT-LDA eigenvalues with a scissor operator (blue) or the G_0W_0 quasiparticle energies (red). Dots represent our calculated BSE data, lines are Fourier interpolations

We found that excitons at momentum $\mathbf{q} = K$ have a lower energy than the direct exciton at $\mathbf{q} = 0$ when starting from the G_0W_0, a feature inherited from the indirectness of the quasiparticle structure. In fact, these low-energy excitons are due to transitions towards the nearly-free electron states at Γ. These new excitonic states are clearly distinguishable from the “standard” BN excitons by plotting their wavefunctions in real space, as it is done in the insets of Fig. 4.4 for several different center-of-mass momenta of the various states.

We plot the electron distribution in real space when fixing the hole just above a Nitrogen atom, like it would be in a p_z orbital. This is what we call the exciton wavefunction in real space.

We tracked the exciton wavefunction of the lowest two bands the high-symmetry lines. We can see that the exciton momentum confers the wavefunction a shape according to the symmetry of the point, *e.g.* it has a straight shape at M but is circular at Γ and K. While the usual $\pi \rightarrow \pi^*$-derived states (green exciton bands in the figure) display the electronic density strongly localized on the Boron sublattice, when the hole is fixed on top of a Nitrogen, the $\pi \rightarrow \sigma^*$-derived states (red exciton band) present an electron density strongly delocalized away from the layer plane. This is a clear signature of nearly-free electron character.

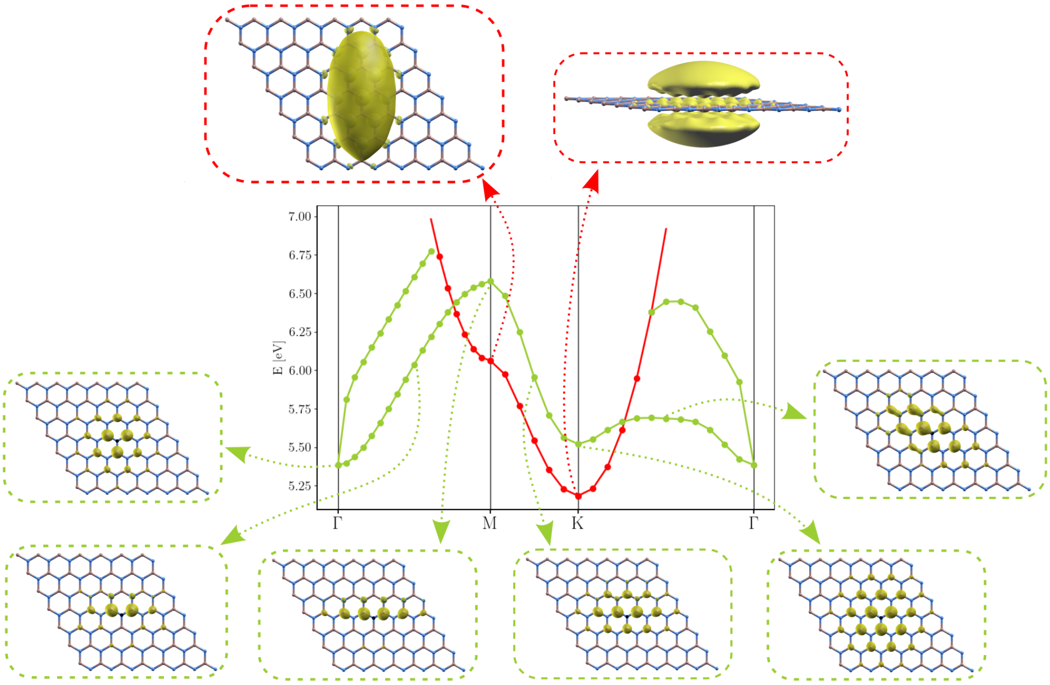

Figure 4.4. – Details of the exciton dispersion of monolayer hexagonal BN. The insets show the spatial localization of the exciton wavefunction at several different q-points and branches (this is obtained by fixing the hole position on top of a Nitrogen atom, i.e. on a valence π orbital, and plotting the resulting electron density). As evidenced in the insets, the red branch in the dispersion plot is due to the nearly-free electron states (involving conduction bands with σ^* character), while the green branches originate from the optically active $\pi - \pi^*$ band transitions.

With this analysis and for other reasons that will be explained in Sec. 4.6, we decided to use the DFT eigenvalues with a scissor operator as a starting point of the BSE and the subsequent steps, namely the calculation of exciton-phonon coupling and the luminescence spectrum.

4.4.2. Exciton-phonon matrix elements resolved in momentum

We can plot the calculated matrix elements over the Brillouin Zone thanks to the $\mathbf{q}$-dependence in Eq. (4.24).

3D bulk hBN

For the bulk hBN, we plot in Fig. 4.5 the exciton-phonon coupling modulus for the lowest-lying finite-momentum excitons $\beta = 1$ and $\beta = 2$ scattered into the bright excitons $\lambda = 3$ and $\lambda = 4$ for all phonon modes. We sum over degenerate excitons and phonon modes. We average over the $\mathbf{q}_z$ points belonging to discrete planes orthogonal to the ΓA line in order to have a two-dimensional plot. The quantity we plot is :

$$|\mathcal{G}_{3+4,1+2}(\mathbf{q}_{\|})| = \frac{1}{N_{q_z}} \left| \sum_{\mu,q_z} \mathcal{G}^{\mu}_{3+4,1+2}(q_z, \mathbf{q}_{\|}) \right| \tag{4.34}$$

We also plot the same quantity but keeping only ZA and ZO phonon modes in the sum. It is the probability that the excitons $\beta = 1$ and $\beta = 2$ are scattered into the zero-momentum excitons $\lambda = 3$ and $\lambda = 4$ by all phonon modes with the corresponding momentum. The information we can extract from this plot is that the coupling has the same symmetry as the crystal, where the 3-fold rotation symmetry is clearly visible. From the panel (a) of Fig. 4.5, we see that the scattering is maximal with excitons close to the ΓA line. From the panel (b), we see that the ZA and ZO modes couple more with the minimum excitons

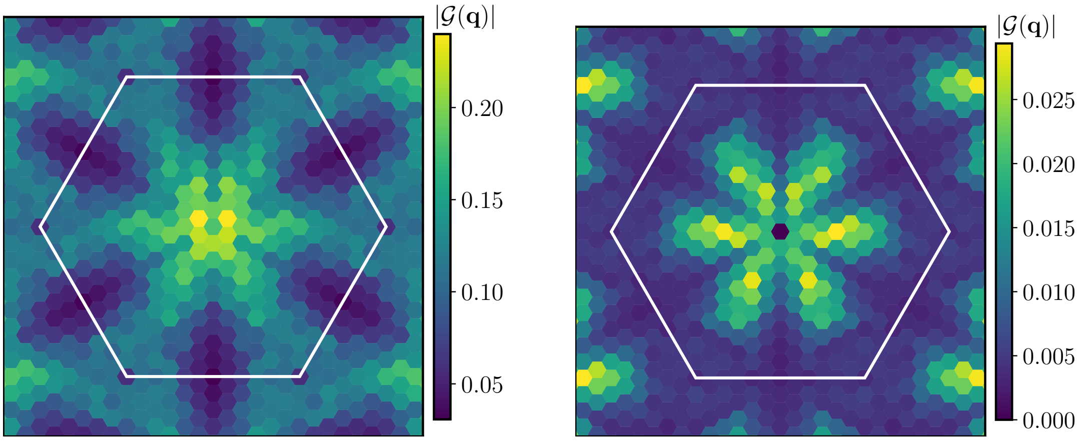

(a) All phonon modes.

(b) ZA+ZO modes only.

Figure 4.5. – Magnitude of the coupling between the finite-momentum excitons and the lowest-lying bright excitons in bulk hexagonal BN. Color bar is the modulus of $\mathcal{G}(\mathbf{q})$ in eV, for a 18×18 $\mathbf{q}$-points grid.

on the ΓK lines. This coupling contributes to about ten percent of the sum of all modes, as can be seen with the color bars.

2D mBN

For the monolayer BN, we plot a similar quantity in Fig. 4.6, except there is no need of averaging over planes since the BZ is two-dimensional. We plot the scattering of finite-momentum excitons $\beta = 1$ and $\beta = 2$ into the two degenerate bright excitons $\lambda = 1$ and $\lambda = 2$ at Γ (where the β and λ indices coincide). Here the situation is different since most of the coupling happens around Γ and is about 4 times stronger than in the bulk materials. The 3-fold hexagonal pattern can still be distinguished but with a lower coupling strength. This result is a first hint that in mBN, it is less likely to see phonon-satellites coming from the scattering of an exciton at the BZ edge than at the center.

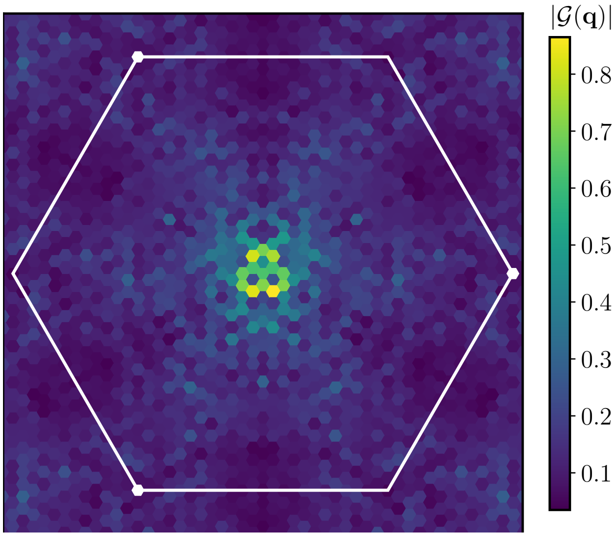

Figure 4.6. – Magnitude of the coupling between the finite-momentum excitons and the lowest-lying bright excitons in monolayer hBN. Color bar is the modulus of $\mathcal{G}(\mathbf{q})$ in eV for a $\mathbf{q}$-points grid of 36×36 grid.

4.5. Luminescence spectra

4.5.1. Benchmark on bulk hBN

We now put to the test our method by calculating the luminescence spectra of bulk hBN which will serve as a benchmark. Indeed we can compare it to our finite difference method as well as existing calculations in the literature and most importantly to experiments. We plot in Fig. 4.7 the phonon and exciton dispersion of bulk hexagonal Boron Nitride. The phonon dispersion has the labels of the different modes. The exciton dispersion exhibits

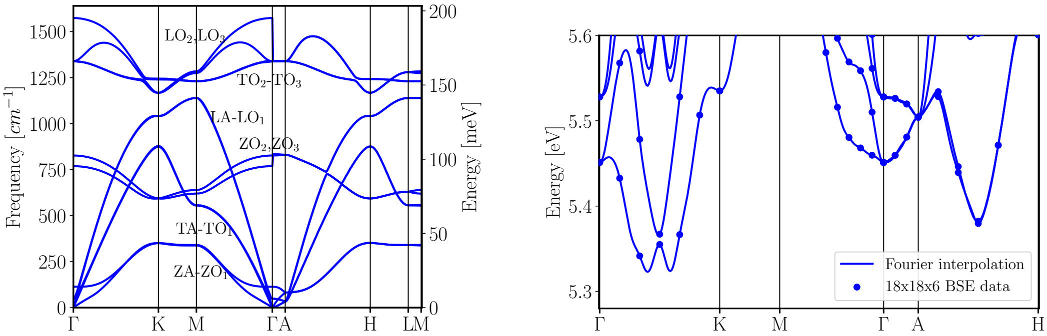

(a) Phonon dispersion of hBN

(b) Exciton dispersion of hBN

Figure 4.7. – Phonon (left) and exciton (right) dispersions of bulk hBN.

a double local minimum on the ΓK line with the Fourier interpolation. However the true minimum is on a point that is not on the ΓK line. This is verified in Ref. [130]. With our coarse $18\times 18\times 6$ momentum grid, the points with the minimum excitonic energies are labelled R_1 and R_2 and their reduced coordinates are fractions of the reciprocal lattice vectors $R_1 = (\frac{1}{9}, \frac{2}{9}, 0)$ and $R_2 = (\frac{1}{9}, \frac{5}{18}, 0)$. With the double-grid approach explained in Appendix E, the sampling of the exciton dispersion is much finer and the true minimum momentum is more accurately located.

In the left panel of Fig. 4.8, we plot the luminescence spectra obtained with the exciton-phonon coupling from finite difference, as presented in Chapter 2, compared with the present *ab initio* method. The peaks are given by a Dirac delta function with a finite broadening added to follow a Lorentzian shape and match the experimental peak shapes (more numerical details can be found in Appendix E). The shape of the LA/TA phonon satellites on the high energy side of the spectrum, computed with the present *ab initio* method, are broader than the single Lorentzian peaks of the finite difference method. This is a consequence of the integration on the full $\mathbf{q}$-grid present in the former method and not in the latter. In addition, we used a double-grid for the exciton energies, the phonon frequencies but keeping the exciton-phonon matrix elements on the coarse grid, so that the numerical instabilities of the renormalization factor in Eq. (4.31) are smoothed out and the dispersions are accurately described. We verified that we obtain similar spectra when we restrict the sum on $\mathbf{q}$ in Eq. (4.33) to the $\bar{q}$ points used in Chapter 2. The difference comes from the renormalization due to the denominators in the self-energy Eq. (4.28) which is missing in the finite difference formula. It should also be noted that the inclusion of phonon absorption processes does not give additional peaks in the spectrum. Indeed, the satellites due to phonon absorption have an intensity proportional to the Bose-Einstein occupation of phonons, which is low for the lattice temperature of 6 K we simulated. We have verified that these peaks appear when the lattice temperature is increased. Similarly, we have verified that higher-energy excitons become populated by the Boltzmann occupation function when we increased T_{exc} and produce satellite peaks in the spectrum.

In the right panel of Fig. 4.8, we also compare our result with the spectrum obtained by

Chen *et al.* in Ref. [118]. As mentioned previously, the exciton-phonon matrix elements we compute are the same than in their formulation, if we do the correct change of variable to account for their different momentum conservation convention. We implemented their convention in `yambo` and verified that the spectra do not change when using one or the other. They compute the luminescence intensity differently than the van Roosbroeck–Shockley relation, this is why the spectra look different. Our spectrum reproduces correctly the position of the satellites measured in Ref. [25] (note that all spectra have been shifted to match the energy of the experimental peaks) and the intensity of the LA/TA doublet on the high energy side, which is an improvement compared to the results of Chen *et al.*. However, the intensity of the LO/TO doublet on the low energy side is not well reproduced. It is in fact inverted, with the TO peak being less intense than the LO one. Since this inaccuracy in the intensity is still in the correct order of magnitude, we decided to proceed with this implementation.

We can also notice that the experimental peaks have phonon overtones due to the scattering with multiple phonon which give them an asymmetric shape,[106] and this is not included in our framework.

Besides, another issue in the spectrum is the presence of a low intensity peak at 5.93 eV, which appear neither in other numerical spectra, nor in experimental measurements. To investigate the origin of this peak, we can separate the contribution of each phonon mode to the spectrum. We plot said contributions in Fig. 4.9 We see that the additional peaks come from scattering of excitons with ZO and ZA phonon modes. In our simulations, we set the light polarization to be in-plane. Hence optically created excitons are in-plane, and their scattering with out-of-plane phonons (namely the ZA and ZO modes) and their

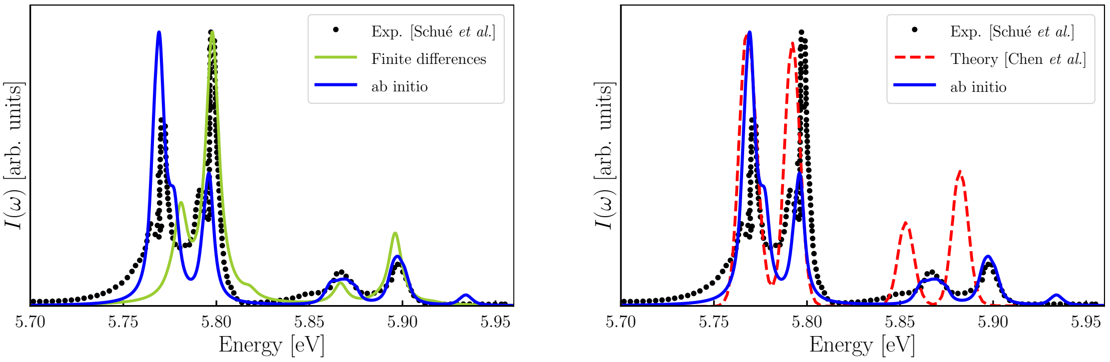

(a) Comparison of finite-difference and *ab initio* methods.

(b) Comparison of our *ab initio* method and the one of Chen *et al.*

Figure 4.8. – Comparisons of the normalized luminescence spectrum obtained with the exciton-phonon matrix elements obtained from our *ab initio* method (blue line) and the finite difference method (green line) on the left panel. On the right, we compare it to the result of Ref. [118] (red dashed line). In both panels, the experimental data (black dots) comes from Ref. [25].

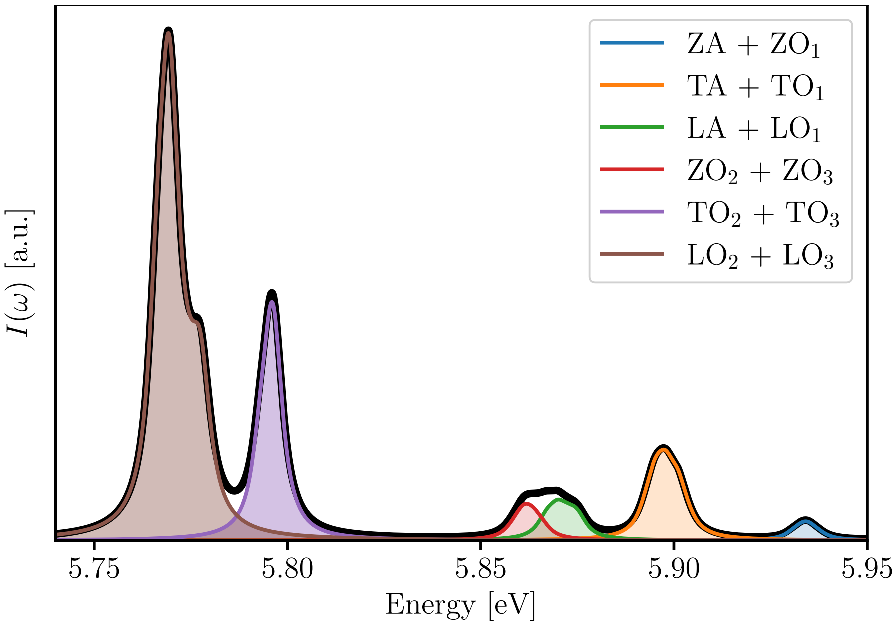

Figure 4.9. – Luminescence spectrum of bulk hBN (black curve) with separated phonon contributions.

successive recombination is forbidden by symmetry.[29, 27] If the crystal symmetries are changed, then these forbidden peaks can appear in photoluminescence. It is the case for rhombohedral BN.[130] In our case, the problem arises from the construction of the exciton-phonon matrix elements in Eq. (4.24). The electron-phonon matrix elements and the exciton eigenvectors have different random phases that depend on the different sets of Kohn-Sham wavefunctions that were used to generate them in the first place. It is a non-trivial technical and numerical issue to account for these phases consistently. Indeed, some DFPT implementations (like QUANTUM ESPRESSO) recalculate the KS wavefunctions at $\mathbf{k}+\mathbf{q}$ for each $\mathbf{q}$. Instead, a single set of wavefunctions is used to define the BSE matrix at any momentum $\mathbf{Q}$ in the `yambo`code, where the $\mathbf{k}+\mathbf{q}$ wavefunctions are obtained by symmetry transformations, thus imposing a specific choice of the relative phase between the wavefunctions. This difference causes a phase mismatch in the definition of the exciton-phonon matrix elements, Eq. (4.24), because both the electron-phonon matrix element and the excitonic coefficients enter as full complex numbers. This is likely the reason why the magnitude of the coupling with ZA and ZO phonon modes is as large as displayed in Fig. 4.8 (b). This issue remains also if the electron-phonon matrix elements are obtained via Wannier interpolation[118], since the wavefunction used to construct the excitonic matrix would be different from the ones resulting via the Wannier procedure. [2] In this case the interpolation process should be modified by fixing the wavefunction phases[131]. The phase mismatch is not present in calculations based on finite differences[99, 86]

---

[2] Notice the curve of Chen *et al.* in panel (b) of Fig.4.8 ends at 5.9 eV, therefore we cannot compare the results for the ZA/ZO case.

because in this case exciton-phonon coupling is directly calculated as a derivative of the exciton dipole matrix elements on a supercell. However, these types of calculations are restricted to a single $\mathbf{q}$-vector. In the case of hBN luminescence, we verified that the phase mismatch only gives small changes in the numerical results (by testing different sets of wavefunctions with different random phases).

A workaround of these issues was used by Zanfrognini *et al.* in Ref. [130] where the same implementation was used to compute the luminescence of bulk hBN and rhombohedral BN. They did not use the crystal symmetries to reduce the size of the BZ and wrote an interface with a third simulation code in order to build the exciton-phonon matrix elements without the phase issue. Overall, this was a much heavier numerical calculation but it allowed to solve two issues in the spectrum. The spectrum they obtained for hBN does not contain the ZA/ZO satellite and has improved relative intensities for the LO/TO and LA/TA doublet with respect to experiments.

Overall, our spectrum is in fairly good agreement with the experimental one. Keeping in mind the issues discussed above, we turn to the study of a case where the main advantage of our method is fully exploited : the fact that we can compare the relative intensities of direct peaks and phonon satellites.

4.5.2. Results on mBN

In this section we report the luminescence spectrum of monolayer hBN calculated using the method presented in Sec. 4.3 with the computational parameters reported in Appendix E. Here we consider an isolated monolayer and compared our results with different experiments reported in the literature. The effect of the substrate will be discussed in the next sections.

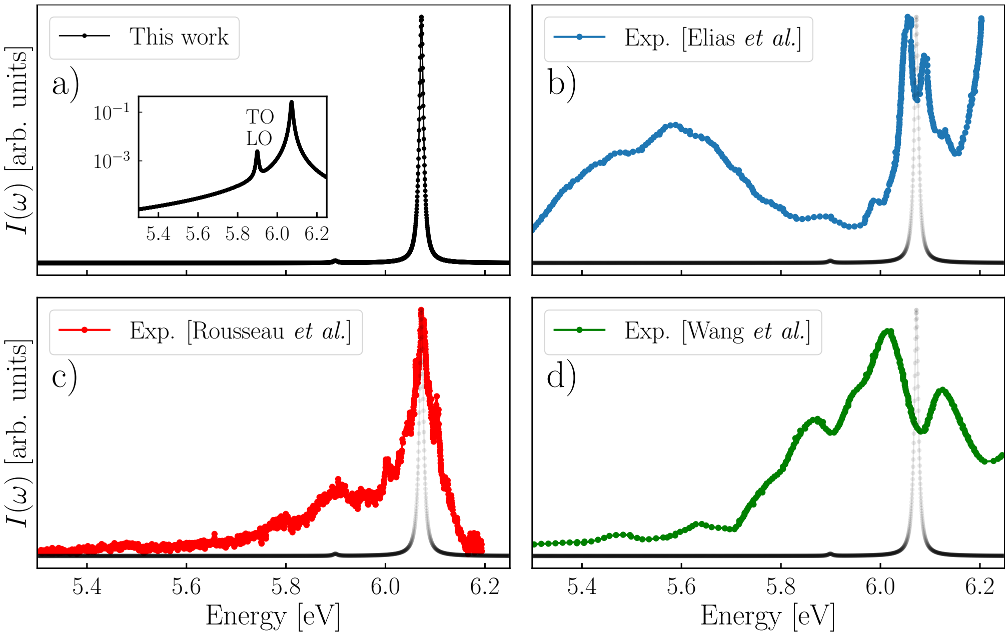

Figure 4.10. – Calculated luminescence spectrum of monolayer hBN (a) compared to the experimental results of Ref. [1](b), Ref. [2](c) and Ref. [3](d). The theoretical spectrum has been shifted to match the main experimental peak (c). For clarity, we have plotted the theoretical spectrum next to each experimental result. In the inset of panel (a) we show the theoretical spectrum in a logarithmic scale, revealing the presence of a small phonon satellite.

We plot the central result of this chapter in Fig. 4.10. In panel (a) we report our luminescence calculations of a single layer m-hBN compared to the measurements of Refs. [1, 3, 2], panels (b),(c),(d). Beside the main direct emission peak, we found a satellite at lower energy that has a small intensity, about two orders of magnitude lower than the direct peak (see inset in logarithmic scale in the panel (a)). We were able to identify the different terms contributing to the satellite intensity by analyzing the single terms of the sum in Eq. (4.33), both in terms of phonons modes and in momenta. Thus we identify the satellite as a scattering from a zero-momentum exciton due to the LO and TO phonons.

We also included possible indirect transition from excitons with momentum corresponding to the K point due to the $\pi \to \pi^*$ transitions (relative minimum of the green curve in Fig. 4.4). However, we found that due to the relatively large energy difference of 0.14 eV between direct and indirect excitons, the contribution of these latter states to the luminescence spectrum is null.[3] Therefore, the additional peaks seen in some of the experiments are not explained by our calculations.

Finally as a sanity check, we considered the possibility that the distance between the

---

[3] We did not consider polaritonic effects that could slightly modify the luminescence spectra, see Ref. [132] for a discussion.

exciton K and Γ is not well reproduced by our calculations and analyzed the matrix elements of the phonon-assisted transitions between K and Γ. We found that these are in any case too small to explain the additional peak seen close to the main one in the experiments with a Graphite substrate.

In the light of these results, let us now discuss the different experiments. The details of the three luminescence spectra reported in the literature, see Fig. 4.10 (b-d), are the following: two of them feature mBN grown by molecular beam epitaxy on Graphite,[1, 3] and one mechanically exfoliated on Silicon Oxide.[2] With the Graphite substrate, multiple peaks are visible. These peaks have been attributed to various causes, which we will briefly summarized here. In the work of Elias *et al.*,[1] the possibility of additional satellites appearing due to scattering of the indirect excitons at K was considered. We also mention that in a very recent article, not peer-reviewed yet,[34] cathodoluminescence measurements of mBN on Graphite revealed a faint peak at 6.04 eV, that was attributed to the phonon-assisted recombination of the K exciton assisted with a ZA phonon. In the work of Rousseau *et al.*[2] they put forward the possible presence of bubbles in the sample as cause of the additional peaks. Finally, in the article of Wang *et al.*[3], these additional peaks were attributed to the presence of multilayer BN regions and the peak at the middle of the three should be caused by defects that would allow the triplet excitons (out of the scope of this thesis) to recombine radiatively.

Our theoretical work allows us to rule out the first hypothesis since, as shown above, the energy difference between Γ and K is large and the phonon-assisted transitions have too low an intensity to have indirect excitons visible in luminescence in the energy range where the second experimental peak appears, while the $\pi \rightarrow \sigma^*$ transitions seem to play no role. Regarding the effect of bubbles in the sample on the luminescence spectra, we have shown in the previous Chapter that strain can induce shifts of the luminescence spectra.[86] Yet, in order to obtain a significant effect, the strain must be very large, and in addition it is difficult to explain with strain the presence of two well-defined peaks, like those visible in the experimental spectra. Finally, there is the hypothesis of defects or multi-layers BN. We think this is the most plausible hypothesis, because it has been shown that some defects can produce levels close to the main exciton,[133] and multi-layers BN induce splittings of the main peak.[99] Finally, note that the presence of defects or edges, which break translational symmetry, could make the indirect exciton visible without the need for phonon mediation.[134]

4.6. Effects of the substrate on the electronic gap and excitons of mBN

In the previous section we considered the isolated mBN and its luminescence spectrum. However it is well known that the interaction of 2D materials with a substrate can strongly modify their electronic and optical properties. In this section we analyze how the presence of a Graphite substrate could modify the picture presented in the previous section. In particular, we will investigate the role of nearly-free electron states and of indirect excitons. In order to see if we can really expect an optical experimental signature from the exciton made of nearly-free electron states – that will make the system functionally indirect – we decided to investigate how the presence of a substrate modifies their position with respect to the direct gap, compared to the freestanding mBN. We included a graphitic substrate in the simulation, analogous to the one used in some of the experiments. Since we are not able to include a full bulk Graphite in the simulation, we modelled it with one and two layers of Graphene. We found that the presence of a graphitic substrate lowers the direct gap at K much more than the indirect one, actually making the system a true direct band gap insulator again. This is most likely due to the stronger interaction of the p_z orbitals of boron with those of Graphene while the planar σ^* states are less affected. The dependence of the mBN gaps on the number of substrate Graphene layers is shown in Fig. 4.11 (calculation details are given in Appendix E).

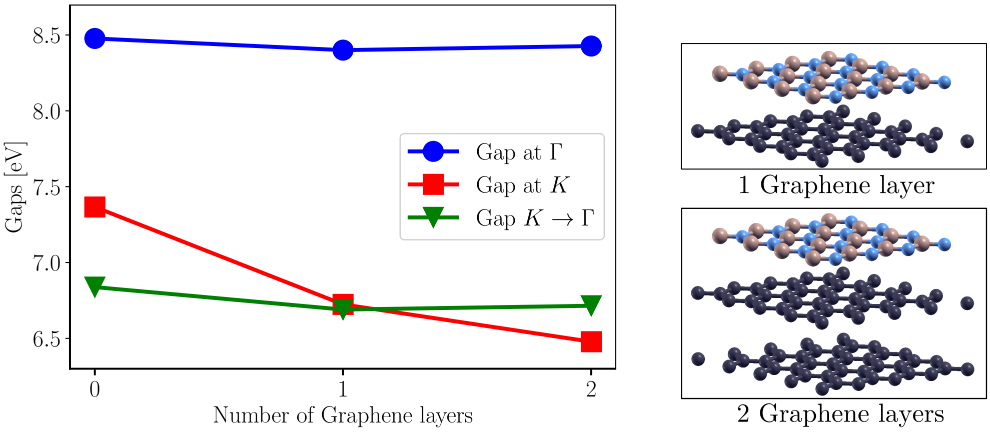

1 Graphene layer

2 Graphene layers

Figure 4.11. – Band gaps of mBN as a function of the number of Graphene layers included in the simulation cell. The large direct gap at Γ is in blue, the indirect $\pi \to \sigma^*$, i.e. $K \to \Gamma$, is in green and the smallest $K \to K$ direct gap is in red.

Therefore, we expect that these states at Γ will not contribute to the luminescence in a realistic experiment where mBN is deposited or grown on a substrate. In order to simulate luminescence from an ideal mBN deposited on a substrate we started from the LDA band structure and applied a scissor operator that allows us to maintain the direct nature of mBN (*i.e.* removing the red "band" in Fig. 4.4).

Next, we investigate the effect of a substrate on the indirect excitons of mBN. As computing the excitonic dispersion in the presence of a substrate would be computationally prohibitive, we decided to use a simple model to study the impact on luminescence. We know that the difference in energy between the excitons at Γ and K is due to correlation effects. Therefore with the substrate increasing the screening, we expect this gap to decrease. Indeed, with increased screening the atractive term in the BSE kernel is stronger, hence increasing the finite-momentum excitons binding energy. By adding a parameter that renormalizes the exciton energies proportionally to their momentum with the formula $E(\mathbf{q}) = E_0(\mathbf{q}) + \alpha|\mathbf{q}|$, we can roughly simulate this effect and bring the exciton at K lower in energy than the one at Γ. Hence, this new minimum gets more populated with the Boltzmann occupation function and it might increase the intensity of phonon satellites. An *ab initio* treatment of the Graphite substrate is possible at the GW and BSE level with recent numerical developments,[135] but it remains too expansive computationally for our way of calculating the exciton-phonon coupling, given the number of $\mathbf{k}$ and $\mathbf{q}$ points needed to accurately describe the sharp electronic dispersion of Graphene layers. More advanced numerical procedures to include the screening of a substrate or any external environment exist,[136, 137] but they are beyond the scope of this thesis.

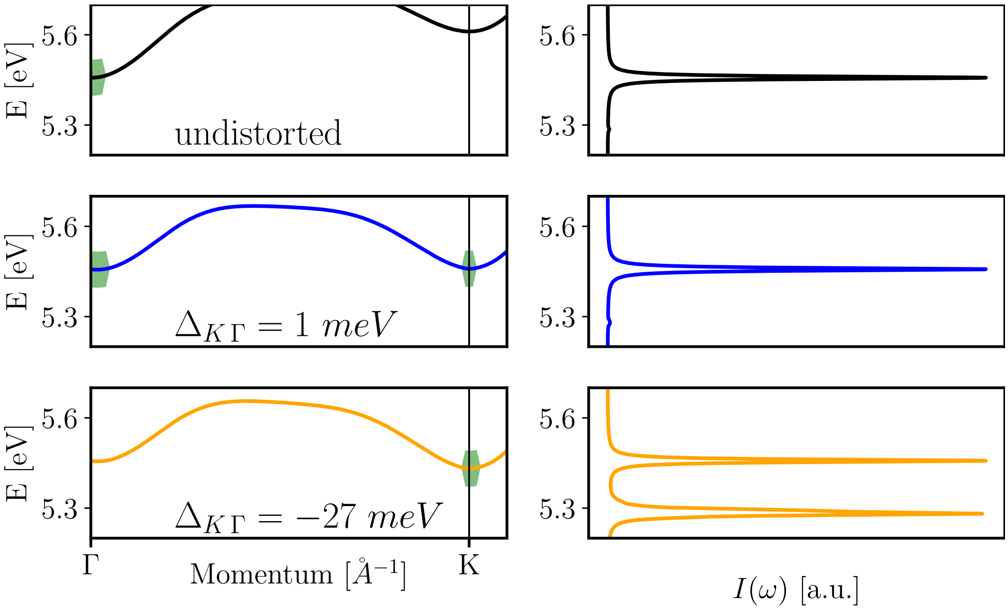

Figure 4.12. – Left column : plots of the Fourier interpolated lowest excitonic band in the dispersion of mBN, between Γ and K, when momentum-dependent distortion is applied to decrease the energy at K. The Boltzmann occupation function is represented in green. Right column : corresponding luminescence plots, normalized to 1. The main peak is always visible and the phonon satellite gain intensity when the distortion brings the energy at K lower than at Γ.

We plot the undistorted exciton dispersion and luminescence spectrum in the two upper panels of Fig. 4.12. In this case the phonon-assisted satellite coming from the K valley is invisible due to the energy separation. In the middle panels, we see that when $\Delta_{K\Gamma} \equiv E_1(\mathrm{K}) - E_1(\Gamma) = 1meV$, the valley at K gets populated, but the corresponding luminescence plots still show a phonon satellite barely visible compared to the direct peak. It is an overlap of the satellites from Γ and from K, that scatter with the same phonon modes and hence have the same energy here. Finally, in the bottom panels when $\Delta_{K\Gamma} = -27$ meV, the K valley is much more populated than the Γ one and thus the phonon satellite becomes visible.

Notice that we did not modify the exciton-phonon matrix elements unchanged for this particular plot, which is probably an inadequate approximation since the screening of the Graphite substrate screening also influences the electron-phonon coupling.[138] It means that the change in the luminescence spectra with the distortion is only due to the change in exciton energies at finite-momentum and to the Boltzmann occupation function. As a consequence, the satellite in the bottom-right panel of Fig. 4.12 appears because the direct exciton is less populated. In any case, to see this effect the K valley needs to be renormalized of about 170 meV, which seems unrealistic for a Graphite substrate. This is another indication to rule out the possibility that the satellite coming from K could be as bright as the direct peak in the experiments.

4.7. Preliminary results on bBN

The Bernal form as a similar crystal structure as hBN, but the stacking of the layers is AB instead of AA', with a Boron atom lying above the center of an hexagon, as illustrated in Fig. 1.1. This part of the thesis is a preliminary study for a larger work where we will also investigate the effect of different DFT functionals and convergence parameters on bBN properties. As a start, we used the same computational parameters as the more studied bulk hBN, that can be found in Table. E.1 of Appendix E.

The Bernal stacking type exhibits an identical phonon dispersion with hBN, meaning that the stacking has no influence on the energies of the phonons. However it has quite a different exciton dispersion compared to hBN, as displayed in Fig. 4.13. The relative minimum along ΓK now has an higher energy than the one at Γ. The energy of the exciton at Γ is 5.39 eV and the minimum at $\mathbf{q} = (\frac{1}{6}, \frac{1}{6}, 0)$, which is $|\Gamma K|/2$, is 5.41 eV. This 20 meV difference means that the indirect exciton will be populated at large effective temperatures by the Boltzmann occupation function, but only sparsely in a low-temperature measurement. We then expect most of the photoluminescence intensity to come from the direct exciton, with very little phonon-assisted satellite peaks in the spectrum.

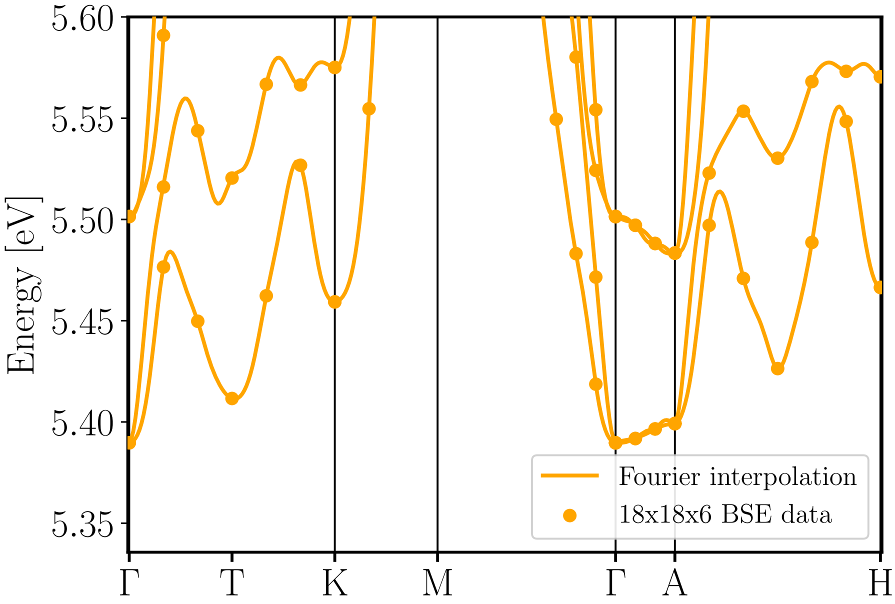

Figure 4.13. – Calculated exciton dispersion in Bernal BN

We plot the exciton-phonon matrix elements for bBN in Fig. 4.5. The coupling for all phonon modes is very similar than for hBN, with a snowflake shape. The maximum of the coupling is around Γ with some coupling along the ΓK lines. Concerning the ZA and ZO modes, the matrix elements are more homogeneous with maxima at the middle of the ΓK lines and the coupling is non-zero over the whole BZ, although the magnitude is slightly lower than for hBN.

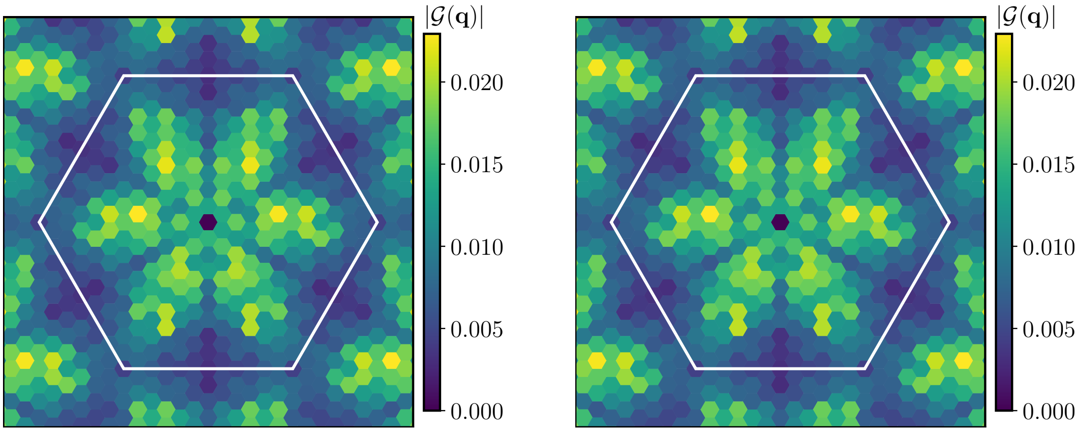

(a) All phonon modes.

(b) ZA+ZO modes only.

Figure 4.14. – Magnitude of the coupling between the finite-momentum excitons and the lowest-lying bright excitons in Bernal BN. Color bar is the modulus of $\mathcal{G}(\mathbf{q}_{\|})$ in eV, for a 18×18 $\mathbf{q}$-points grid.

We found most of the contribution to the luminescence came from excitonic states at Γ and along the ΓA line which has a low dispersion (see Fig. 4.13). This is in agreement with the exciton-phonon matrix elements showing a higher coupling around Γ.

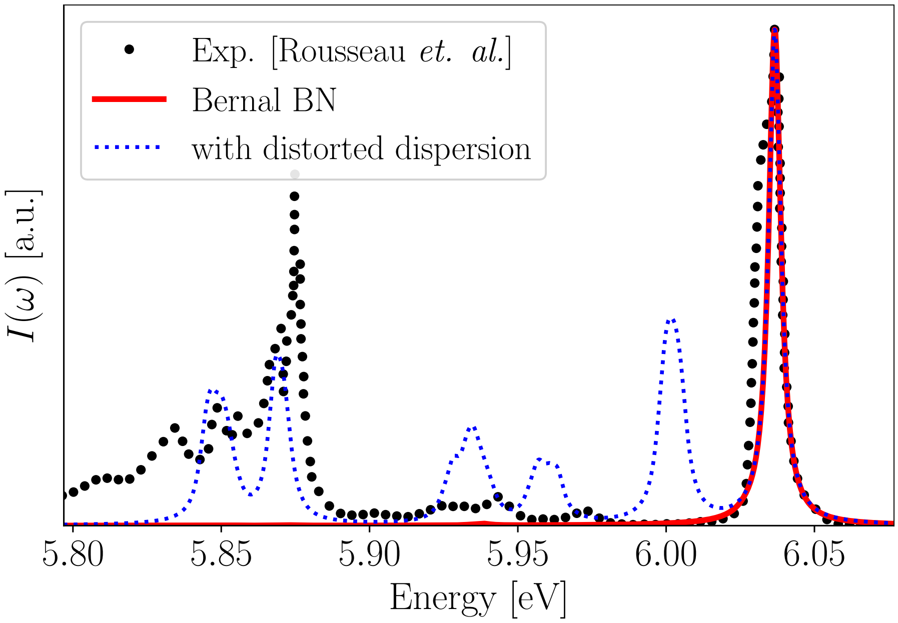

Figure 4.15. – Plots of the calculated luminescence spectrum of Bernal BN, with and without exciton energy distortion, compared to experiments. We shifted the calculated spectra to match the experimental peaks.

As in the mBN case, we now investigate how a small distortion of the excitonic dispersion modifies the luminescence spectra. We expect that some satellite peaks will appear with intensities comparable to the direct one. In Fig. 4.15 we report the luminescence spectra with and without distortion of the excitonic dispersion. We applied a distortion such that the valley at the middle of the ΓK line $T = |\Gamma K|/2$ gets a few meV lower that the Γ excitonic state : $\Delta_{\Gamma T} = -13$ meV. This corresponds to a renormalization of $\Delta E(T) = 35$ meV.
The luminescence plot with separated phonon contributions in Fig. 4.16 allows to identify the peaks that are absent in the experiments and that are made visible with the distortion. Here we plot only the satellite contributions to luminescence. These satellites come from scattering with excitons in the new minimal T valley on the ΓK line. We see that one of the major contribution comes from a ZO phonon mode, which should be forbidden by symmetry. This is the same numerical issue that was explained above, for the ZA and ZO peaks in the spectra of hBN.

Since a change in the exciton energies can change drastically the luminescence spectrum, we need to perform a careful study of all the numerical parameters involved in the workflow. This is still ongoing work.

Conclusion of the chapter

In this Chapter, I presented a first-principles methodology to calculate phonon-assisted luminescence in exciton-dominated materials. It is based on a dynamical correction to the static Bethe-Salpeter Hamiltonian given by an excitonic self-energy term describing exciton-phonon interaction. Using this self-energy, we obtained a formula for the optical response that contains corrections up to first order in the exciton-phonon coupling. Unlike previous formulations, we are also able to calculate the renormalization factor for direct transitions, which allows for a quantitative comparison between direct and phonon-assisted emission signatures. From the optical response function, and employing a steady-state approximation, we obtained a formula for the phonon-assisted luminescence. All ingredients that enter in this formulation have been calculated *ab initio*, except for the excitonic temperature relative to the occupation of excitonic states. We first validate our approach on bulk hBN, where clear and well-established experiments exist. We then applied this approach to the BN single layer, where recent discordant photoluminescence measurements were reported independently by different groups. In mBN we found that the luminescence spectrum is dominated by the single direct peak only and phonon replicas, while present, have negligible intensity. In addition, phonon-assisted transitions from the lowest indirect exciton remain too low in intensity to explain the measured spectra. Therefore, we rule out phonon-assisted processes as the cause of the additional spectral fine structure sometimes seen in experiment. We support the interpretation that this fine

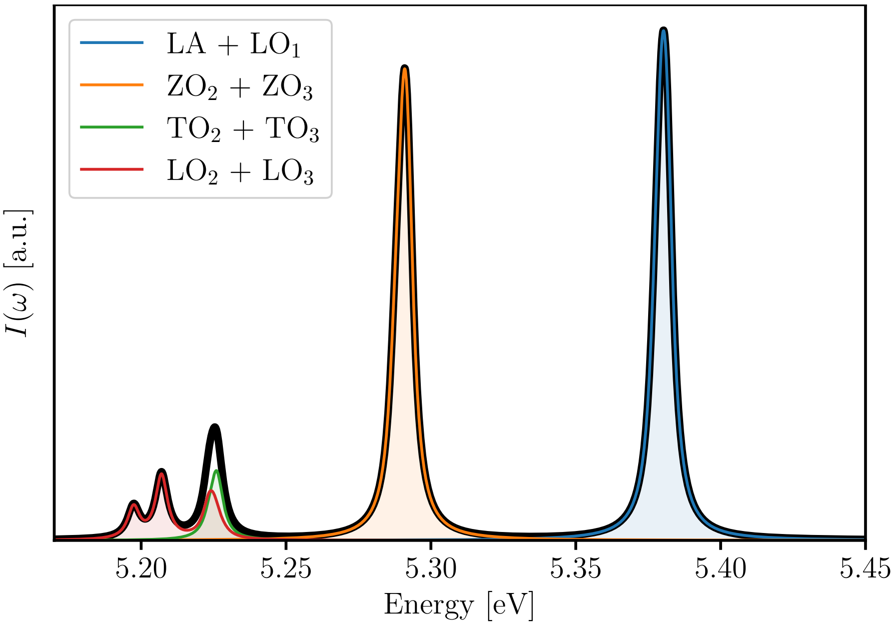

Figure 4.16. – Plots of the satellite contributions to the luminescence spectrum of Bernal BN, where the different phonon mode contributions are separated (shifted to match the experimental peaks). The black curve is the total luminescence signal.

structure is not intrinsic, nor due only to substrate effects, but depends on sample quality.

Regarding bBN, our first numerical studies suggest a direct luminescence. Despite considering a small distortion of the excitonic dispersion, our spectrum still differs from the experimental one. We are investigating the role of van der Waals correction and the possible numerical problems in our procedure to provide an accurate interpretation for the experimental results.

Finally, we would like to mention that our methodology based on the dynamical self-energy has been fully implemented in the `yambo` code and is applicable to other systems of interest. This formulation allows one to compute more observables than just the luminescence presented here, such as phonon-assisted absorption, exciton linewidths and relaxation rates.

Added note. We have become aware of a recently published article, Ref. [139], in which a formula for the phonon-assisted luminescence was derived using non-equilibrium Green's functions theory. It includes renormalization factors in a very similar way to our approach.

Summary of Chapter 4.

- The coupling between excitons and phonons was computed *ab initio* in Sec. 4.2 by treating the electron-phonon interaction as a dynamical perturbation.
- This approach allowed to compute the interaction between all excitons and all phonon modes in the full Brillouin Zone.
- Within MBPT, we could formally build an exciton-phonon self-energy that corrected the response function dynamically in Sec. 4.3.
- Using the van Roosbroeck–Shockley relation, we were able to compute luminescence spectra with contributions from both direct excitons and phonon-assisted transitions, with a renormalization factor that allowed their relative intensities to be compared.
- We benchmarked the method on bulk hBN and applied it to the monolayer mBN and to the Bernal phase bBN, and compared our results with available experimental measurements.

Conclusion

The scope of this thesis was to reproduce and predict the luminescence spectra of distinct hBN nanostructures. To do so, we used and developed various theoretical and numerical approaches to the study of phonon-assisted luminescence. Additionally it provides an insightful interpretation of the different features appearing in experimental measurements thanks to first-principles calculations of the exciton-phonon coupling. These calculations are built upon the state-of-the-art *ab initio* theories presented in the second Chapter.

Main results

In the third Chapter, we applied an existing approach where the response function gets a static correction due to the phonon-assisted transitions. This correction is calculated through finite-difference derivatives, wherein we build supercells and displace the contained atoms along all the phonon modes. We applied this method to compute the luminescence spectra of bulk hBN under uniaxial strain. We found that multiple nonequivalent excitonic valleys in the Brillouin Zone contribute to luminescence due to rotational symmetry breaking. Therefore the phonon-assisted peaks split for low values of strain. This splitting also broadens the peaks and increases the intensity of the LA/TA doublet in relation to the LO/TO. This partially agrees with recent experimental measurements of cathodoluminescence of strained hBN.

In the fourth Chapter, we went beyond the finite-difference method and presented the derivation of an *ab initio* method to obtain exciton-phonon coupling.This method enables the treatment of the coupling of all excitons with all phonon modes in the entire Brillouin Zone and represents an improvement in both numerical and theoretical aspects. It yields the renormalization of the direct peak by the appearance of phonon-assisted satellites in the luminescence spectrum, originating from the dynamical correction to the response function. We implemented this approach in the `yambo` code and applied it to the calculation of phonon-assisted luminescence of a monolayer of hBN. We obtained the first results of calculated luminescence from first-principles, encompassing both direct and phonon-assisted emission signatures. We were able to compare their relative intensities and ruled out the possibility of distinguishing phonon satellites due to the bright intensity of the direct peak. This possibility was one of the interpretations proposed in very recently published experimental measurements displaying features of debated origin. We also investigated the role of the screening of a graphitic substrate on the intensity of the indirect exciton peak and found that it is likely not sufficient to reveal the phonon-assisted processes in the experiments.

We finally showed the preliminary results of an ongoing study on the Bernal phase of BN. Theoretical and experimental evidence suggest that both direct and phonon-assisted emission processes could be visible with comparable intensities. This makes it an ideal testing ground for our approach. First results suggest a direct luminescence, but a deeper investigation is necessary as the results have a strong dependence on small changes in the numerical parameters used in the simulations.

Future work and perspectives

We expect that the work of this thesis will spark numerous future developments, both in terms of applications, new theoretical models and collaborations between theory and experience. The subsequent paragraphs outline the future developments pertaining to each part of the thesis.

Regarding the results of strained hBN, the agreement with experimental data could be improved by sampling the excitonic dispersion with a finer grid in reciprocal space. A tight-binding model adjusted on coarse *ab initio* data could help refine this sampling. Moreover, the strain could be included as a parameter of the model. Experimentally, the strain applied to the sample could be estimated with reflectance and optical absorption experiments. These could be compared with our results for the variation of exciton energy and the splitting of the absorption main peak. We plan to start a new joint experimental and theoretical study of the effect of strain on the optical properties of hBN to get further insight on this topic.

Regarding the *ab initio* calculation of the exciton-phonon coupling, a workaround to the wrong intensities and to the phase problem was found by Zanfrognini *et al* in Ref. [130]. However their approach necessitates the use of a third simulation code and does not exploits the crystal symmetries to reduce the size of the Brillouin Zone. This significantly increases the computational load and the disk space necessary for the workflow. A promising solution to the phase problem is currently being developed, which involves a different way of calculating the electron-phonon interaction.

For the study of the Bernal phase of BN, we are investigating ways to reduce the disk space required, which can be prohibitive for more complex materials, without compromising the accuracy of the workflow. The study of bBN and the dependence of its luminescence spectrum with respect to the position of the excitonic valleys could pave the way for engineering its optical properties and potentially build devices that take advantage of the direct and indirect nature of this material. We expect a new article to be submitted on this subject before the end of the year.

Although in this thesis the exciton-phonon coupling has been calculated with two different methods, the luminescence intensity has been obtained using the van Roosbroeck–Shockley relation in both cases. On the one hand, assuming we are in a steady state situation, it allows to compute the luminescence from the knowledge of the macroscopic dielectric function that we obtain *ab initio*. It is much simpler both numerically and theoretically than considering the out-of-equilibrium interplay between electrons, holes, phonons and photons. On the other hand, it requires an external parameter, the excitonic temperature, hence the workflow is not fully *ab initio*. It should be possible to avoid this and derive an exciton conversion rate from the exciton-phonon coupling we have computed. We could then include the exciton relaxation from higher energy to the lower valley and their thermalization and replace the *ad hoc* excitonic temperature by an *ab initio* one. While I was writing this thesis, a new pre-published work was released where the authors derived an equation for the phonon-mediated thermalization of excitons,[120] but it is at present limited to a simple model.

In the current state, the knowledge of the *ab initio* exciton-phonon matrix elements can be used to study exciton dynamics.[140] The exciton-phonon self-energy also allows to compute the exciton lifetimes which are helpful for the ultrafast spectroscopy, a field of relevance in Condensed Matter Physics.

Moreover, this *ab initio* method could be extended to the scattering with multiple phonons, also including renormalization of the exciton energies by dynamical interaction with phonons, thanks to the cumulant expansion as shown theoretically by Cudazzo in Ref. [55]. Our implementation in the `yambo` code can be readily extended to this more general case. It would then allow one to simulate the temperature dependence of the exciton energies and of the optical spectra on the same footing.

Finally, a rigorous treatment of the exciton-lattice interaction is the first step towards a description of the excited state geometry of periodic solids. It could used to the calculation of forces in a GW-BSE framework for instance, with applications to exciton self-trapping or charge separation, essential phenomena for optoelectronic devices and photovoltaics.

Bibliography

[1] Christine Elias, Pierre Valvin, Thomas Pelini, A Summerfield, CJ Mellor, TS Cheng, L Eaves, CT Foxon, PhH Beton, SV Novikov, et al. “Direct band-gap crossover in epitaxial monolayer boron nitride”. In: *Nature communications* 10.1 (2019), p. 2639 (cit. on pp. 16, 32, 88, 109, 110).

[2] Adrien Rousseau, Lei Ren, Alrik Durand, Pierre Valvin, Bernard Gil, Kenji Watanabe, Takashi Taniguchi, Bernhard Urbaszek, Xavier Marie, Cédric Robert, et al. “Monolayer boron nitride: hyperspectral imaging in the deep ultraviolet”. In: *Nano Letters* 21.23 (2021), pp. 10133–10138 (cit. on pp. 16, 32, 88, 109, 110).

[3] Ping Wang, Woncheol Lee, Joseph P Corbett, William H Koll, Nguyen M Vu, David Arto Laleyan, Qiannan Wen, Yuanpeng Wu, Ayush Pandey, Jiseok Gim, et al. “Scalable synthesis of monolayer hexagonal boron nitride on graphene with giant bandgap renormalization”. In: *Advanced Materials* 34.21 (2022), p. 2201387 (cit. on pp. 16, 32, 88, 109, 110).

[4] Yole Développement. *UVC LEDs : One Solution to Contain the COVID-19 Pandemic*. 2020. URL: `http://www.yole.fr/iso_upload/News/2020/PR_UV_LED_MarketUpdate_YOLEGROUP_Oct2020.pdf` (cit. on p. 28).

[5] Yoram Gerchman, Hadas Mamane, Nehemya Friedman, and Michal Mandelboim. “UV-LED disinfection of Coronavirus: Wavelength effect”. In: *Journal of Photochemistry and Photobiology B: Biology* 212 (2020), p. 112044. ISSN: 1011-1344. DOI: `https://doi.org/10.1016/j.jphotobiol.2020.112044`. URL: `https://www.sciencedirect.com/science/article/pii/S1011134420304942` (cit. on p. 28).

[6] Tsung-Chi Hsu, Yu-Tsai Teng, Yen-Wei Yeh, Xiaotong Fan, Kuo-Hsiung Chu, Su-Hui Lin, Kuo-Kuang Yeh, Po-Tsung Lee, Yue Lin, Zhong Chen, et al. “Perspectives on UVC LED: Its progress and application”. In: *Photonics*. Vol. 8. 6. MDPI. 2021, p. 196 (cit. on p. 28).

[7] *Batteries2030+ roadmap*. URL: `https://battery2030.eu/wp-content/uploads/2022/07/BATTERY-2030-Roadmap_Revision_FINAL.pdf` (cit. on p. 28).

[8] *Quantum Flagship 2023 report*. URL: `https://digital-strategy.ec.europa.eu/en/library/eus-quantum-technologies-flagship` (cit. on p. 28).

[9] *Graphene Flagship annual report 2022*. URL: `https://graphene-flagship.eu/media/blepvqzl/graphene-flagship_ar-2022_spreads_web.pdf` (cit. on p. 28).

[10] Kostya S Novoselov, Andre K Geim, Sergei V Morozov, De-eng Jiang, Yanshui Zhang, Sergey V Dubonos, Irina V Grigorieva, and Alexandr A Firsov. "Electric field effect in atomically thin carbon films". In: *science* 306.5696 (2004), pp. 666–669 (cit. on p. 28).

[11] Andre K Geim and Irina V Grigorieva. "Van der Waals heterostructures". In: *Nature* 499.7459 (2013), pp. 419–425 (cit. on p. 28).

[12] Lorenzo Sponza, Hakim Amara, Claudio Attaccalite, Sylvain Latil, Thomas Galvani, Fulvio Paleari, Ludger Wirtz, and François Ducastelle. "Direct and indirect excitons in boron nitride polymorphs: A story of atomic configuration and electronic correlation". In: *Physical Review B* 98.12 (2018), p. 125206 (cit. on pp. 28, 32, 88, 101, 143).

[13] Sylvain Latil, Hakim Amara, and Lorenzo Sponza. "Structural classification of boron nitride twisted bilayers and ab initio investigation of their stacking-dependent electronic structure". In: *SciPost Physics* 14.3 (2023), p. 053 (cit. on p. 29).

[14] Anthony Impellizzeri, Michele Amato, Chris P Ewels, and Alberto Zobelli. "Electronic structure of folded hexagonal boron nitride". In: *The Journal of Physical Chemistry C* 126.41 (2022), pp. 17746–17752 (cit. on p. 29).

[15] E Blundo, E Cappelluti, M Felici, G Pettinari, and A Polimeni. "Strain-tuning of the electronic, optical, and vibrational properties of two-dimensional crystals". In: *Applied Physics Reviews* 8.2 (2021) (cit. on p. 29).

[16] Martin Dressel and George Grüner. *Electrodynamics of solids: optical properties of electrons in matter*. 2002 (cit. on pp. 29, 62).

[17] Ivan Pelant and Jan Valenta. *Luminescence spectroscopy of semiconductors*. OUP Oxford, 2012 (cit. on pp. 29, 63).

[18] Kris T Delaney, Patrick Rinke, and Chris G Van de Walle. "Auger recombination rates in nitrides from first principles". In: *Applied Physics Letters* 94.19 (2009) (cit. on p. 29).

[19] WH Balmain. "XLVI. Observations on the formation of compounds of boron and silicon with nitrogen and certain metals". In: *The London, Edinburgh, and Dublin Philosophical Magazine and Journal of Science* 21.138 (1842), pp. 270–277 (cit. on p. 30).

[20] Kenji Watanabe, Takashi Taniguchi, and Hisao Kanda. "Direct-bandgap properties and evidence for ultraviolet lasing of hexagonal boron nitride single crystal". In: *Nature materials* 3.6 (2004), pp. 404–409 (cit. on p. 30).

[21] Andrey V Kretinin, Yuan Cao, Jhih-Sian Tu, GL Yu, Rashid Jalil, Konstantin S Novoselov, Sarah J Haigh, Ali Gholinia, Artem Mishchenko, Marcelo Lozada, et al. “Electronic properties of graphene encapsulated with different two-dimensional atomic crystals”. In: *Nano letters* 14.6 (2014), pp. 3270–3276 (cit. on p. 31).

[22] Viktor Ivády, Gergely Barcza, Gergő Thiering, Song Li, Hanen Hamdi, Jyh-Pin Chou, Örs Legeza, and Adam Gali. “Ab initio theory of the negatively charged boron vacancy qubit in hexagonal boron nitride”. In: *npj Computational Materials* 6.1 (2020), p. 41 (cit. on p. 31).

[23] Gabriele Grosso, Hyowon Moon, Benjamin Lienhard, Sajid Ali, Dmitri K Efetov, Marco M Furchi, Pablo Jarillo-Herrero, Michael J Ford, Igor Aharonovich, and Dirk Englund. “Tunable and high-purity room temperature single-photon emission from atomic defects in hexagonal boron nitride”. In: *Nature communications* 8.1 (2017), pp. 1–8 (cit. on p. 31).

[24] Daniel Wigger, Robert Schmidt, Osvaldo Del Pozo-Zamudio, Johann A Preuß, Philipp Tonndorf, Robert Schneider, Paul Steeger, Johannes Kern, Yashar Khodaei, Jaroslaw Sperling, et al. “Phonon-assisted emission and absorption of individual color centers in hexagonal boron nitride”. In: *2D Materials* 6.3 (2019), p. 035006 (cit. on p. 31).

[25] Léonard Schué, Lorenzo Sponza, Alexandre Plaud, Hakima Bensalah, Kenji Watanabe, Takashi Taniguchi, François Ducastelle, Annick Loiseau, and Julien Barjon. “Bright luminescence from indirect and strongly bound excitons in h-BN”. In: *Physical review letters* 122.6 (2019), p. 067401 (cit. on pp. 31, 85, 97, 106).

[26] Christine Elias, Giorgia Fugallo, Pierre Valvin, Christian L’Henoret, J Li, JH Edgar, F Sottile, M Lazzeri, A Ouerghi, Bernard Gil, et al. “Flat bands and giant light-matter interaction in hexagonal boron nitride”. In: *Physical Review Letters* 127.13 (2021), p. 137401 (cit. on pp. 31, 86).

[27] Guillaume Cassabois, Pierre Valvin, and Bernard Gil. “Hexagonal boron nitride is an indirect bandgap semiconductor”. In: *Nature photonics* 10.4 (2016), pp. 262–266 (cit. on pp. 31, 84, 98, 107).

[28] Elena Cannuccia, B Monserrat, and Claudio Attaccalite. “Theory of phonon-assisted luminescence in solids: application to hexagonal boron nitride”. In: *Physical Review B* 99.8 (2019), p. 081109 (cit. on pp. 31, 33, 80, 84, 91, 98, 140).

[29] Fulvio Paleari, Henrique PC Miranda, Alejandro Molina-Sánchez, and Ludger Wirtz. “Exciton-phonon coupling in the ultraviolet absorption and emission spectra of bulk hexagonal boron nitride”. In: *Physical review letters* 122.18 (2019), p. 187401 (cit. on pp. 31, 33, 64, 80, 81, 84, 91, 94, 107, 140).

[30] Luis Artús, Martin Feneberg, Claudio Attaccalite, James H Edgar, Jiahan Li, Rüdiger Goldhahn, and Ramon Cuscó. “Ellipsometry Study of Hexagonal Boron Nitride Using Synchrotron Radiation: Transparency Window in the Far-UVC”. In: *Advanced Photonics Research* 2.5 (2021), p. 2000101 (cit. on pp. 31, 63, 83, 85).

[31] Adrien Rousseau, Pierre Valvin, Wilfried Desrat, Lianjie Xue, Jiahan Li, James H Edgar, Guillaume Cassabois, and Bernard Gil. “Bernal Boron Nitride Crystals Identified by Deep-Ultraviolet Cryomicroscopy”. In: *ACS nano* 16.2 (2022), pp. 2756–2761 (cit. on pp. 32, 88).

[32] Adrien Rousseau, Pierre Valvin, L Xue, J Li, JH Edgar, Bernard Gil, and Guillaume Cassabois. “Phonon-assisted broadening in Bernal boron nitride: A comparison between indirect and direct excitons”. In: *Physical Review B* 106.3 (2022), p. 035203 (cit. on pp. 32, 88).

[33] Leonard Schue, Bruno Berini, Andreas C Betz, Bernard Placais, Francois Ducastelle, Julien Barjon, and Annick Loiseau. “Dimensionality effects on the luminescence properties of hBN”. In: *Nanoscale* 8.13 (2016), pp. 6986–6993 (cit. on pp. 32, 87, 101).

[34] K Shima, TS Cheng, CJ Mellor, PH Beton, C Elias, P Valvin, B Gil, G Cassabois, SV Novikov, and SF Chichibu. “Cathodoluminescence spectroscopy of monolayer hexagonal boron nitride”. In: *arXiv preprint arXiv:2305.09952* (2023) (cit. on pp. 32, 88, 110).

[35] Walter Kohn and LJ Sham. “Density functional theory”. In: *CONFERENCE PROCEEDINGS-ITALIAN PHYSICAL SOCIETY*. Vol. 49. EDITRICE COMPOSITORI. 1996, pp. 561–572 (cit. on p. 32).

[36] Lars Hedin. “New method for calculating the one-particle Green’s function with application to the electron-gas problem”. In: *Physical Review* 139.3A (1965), A796 (cit. on pp. 32, 46, 50).

[37] Ferdi Aryasetiawan and Olle Gunnarsson. “The GW method”. In: *Reports on Progress in Physics* 61.3 (1998), p. 237 (cit. on pp. 32, 43, 51, 136, 143).

[38] Richard M Martin, Lucia Reining, and David M Ceperley. *Interacting electrons*. Cambridge University Press, 2016 (cit. on pp. 33, 43, 56, 136).

[39] Stefano Baroni, Stefano De Gironcoli, Andrea Dal Corso, and Paolo Giannozzi. “Phonons and related crystal properties from density-functional perturbation theory”. In: *Reviews of modern Physics* 73.2 (2001), p. 515 (cit. on pp. 33, 66, 68, 69).

[40] Yutaka Toyozawa. *Optical processes in solids*. Cambridge University Press, 2003 (cit. on pp. 33, 97).

[41] Yutaka Toyozawa. “Interband effect of lattice vibrations in the exciton absorption spectra”. In: *Journal of Physics and Chemistry of Solids* 25.1 (1964), pp. 59–71 (cit. on pp. 33, 97).

[42] Koichi Shindo. “Effective electron-hole interaction in shallow excitons”. In: *Journal of the Physical Society of Japan* 29.2 (1970), pp. 287–296 (cit. on pp. 33, 57).

[43] A Thränhardt, S Kuckenburg, A Knorr, T Meier, and SW Koch. “Quantum theory of phonon-assisted exciton formation and luminescence in semiconductor quantum wells”. In: *Physical Review B* 62.4 (2000), p. 2706 (cit. on p. 33).

[44] LH Hall, J Bardeen, and FJ Blatt. “Infrared absorption spectrum of germanium”. In: *Physical Review* 95.2 (1954), p. 559 (cit. on p. 33).

[45] Jesse Noffsinger, Emmanouil Kioupakis, Chris G Van de Walle, Steven G Louie, and Marvin L Cohen. “Phonon-assisted optical absorption in silicon from first principles”. In: *Physical review letters* 108.16 (2012), p. 167402 (cit. on p. 33).

[46] Vasili Perebeinos, J Tersoff, and Phaedon Avouris. “Effect of exciton-phonon coupling in the calculated optical absorption of carbon nanotubes”. In: *Physical Review Letters* 94.2 (2005), p. 027402 (cit. on pp. 33, 89, 94).

[47] Ferd E Williams. “Theoretical low temperature spectra of the thallium activated potassium chloride phosphor”. In: *Physical Review* 82.2 (1951), p. 281 (cit. on p. 33).

[48] Melvin Lax. “The Franck-Condon principle and its application to crystals”. In: *The Journal of chemical physics* 20.11 (1952), pp. 1752–1760 (cit. on p. 33).

[49] Marios Zacharias and Feliciano Giustino. “One-shot calculation of temperature-dependent optical spectra and phonon-induced band-gap renormalization”. In: *Physical Review B* 94.7 (2016), p. 075125 (cit. on pp. 33, 80, 81).

[50] Tianlun Allan Huang, Marios Zacharias, D Kirk Lewis, Feliciano Giustino, and Sahar Sharifzadeh. “Exciton–phonon interactions in monolayer germanium selenide from first principles”. In: *The Journal of Physical Chemistry Letters* 12.15 (2021), pp. 3802–3808 (cit. on p. 33).

[51] T Feldtmann, M Kira, and Stephan W Koch. “Phonon sidebands in semiconductor luminescence”. In: *physica status solidi (b)* 246.2 (2009), pp. 332–336 (cit. on p. 34).

[52] Samuel Brem, August Ekman, Dominik Christiansen, Florian Katsch, Malte Selig, Cedric Robert, Xavier Marie, Bernhard Urbaszek, Andreas Knorr, and Ermin Malic. “Phonon-assisted photoluminescence from indirect excitons in monolayers of transition-metal dichalcogenides”. In: *Nano letters* 20.4 (2020), pp. 2849–2856 (cit. on p. 34).

[53] Gabriel Antonius and Steven G. Louie. “Theory of exciton-phonon coupling”. In: *Phys. Rev. B* 105 (8 Feb. 2022), p. 085111. DOI: `10.1103/PhysRevB.105.085111`. URL: `https://link.aps.org/doi/10.1103/PhysRevB.105.085111` (cit. on p. 34).

[54] Fulvio Paleari and Andrea Marini. “Exciton-phonon interaction calls for a revision of the “exciton” concept”. In: *Physical Review B* 106.12 (2022), p. 125403 (cit. on pp. 34, 90).

[55] Pierluigi Cudazzo. “First-principles description of the exciton-phonon interaction: A cumulant approach”. In: *Physical Review B* 102.4 (2020), p. 045136 (cit. on pp. 34, 89, 95, 96, 120).

[56] Paolo Giannozzi, Stefano Baroni, Nicola Bonini, Matteo Calandra, Roberto Car, Carlo Cavazzoni, Davide Ceresoli, Guido L Chiarotti, Matteo Cococcioni, Ismaila Dabo, et al. “QUANTUM ESPRESSO: a modular and open-source software project for quantum simulations of materials”. In: *Journal of physics: Condensed matter* 21.39 (2009), p. 395502 (cit. on pp. 34, 74, 140, 143).

[57] Paolo Giannozzi, Oliviero Andreussi, Thomas Brumme, Oana Bunau, M Buongiorno Nardelli, Matteo Calandra, Roberto Car, Carlo Cavazzoni, Davide Ceresoli, Matteo Cococcioni, et al. “Advanced capabilities for materials modelling with Quantum ESPRESSO”. In: *Journal of physics: Condensed matter* 29.46 (2017), p. 465901 (cit. on pp. 34, 74).

[58] D Sangalli, A Ferretti, H Miranda, C Attaccalite, I Marri, E Cannuccia, P Melo, M Marsili, F Paleari, A Marrazzo, G Prandini, P Bonfà, M O Atambo, F Affinito, M Palummo, A Molina-Sánchez, C Hogan, M Grüning, D Varsano, and A Marini. “Many-body perturbation theory calculations using the yambo code”. In: *Journal of Physics: Condensed Matter* 31.32 (2019). DOI: `10.1088/1361-648X/ab15d0`. URL: `https://dx.doi.org/10.1088/1361-648X/ab15d0` (cit. on pp. 34, 76, 82, 140, 143).

[59] Richard M Martin. *Electronic structure: basic theory and practical methods*. Cambridge university press, 2020 (cit. on pp. 37, 40, 42).

[60] P. Hohenberg and W. Kohn. “Inhomogeneous Electron Gas”. In: *Phys. Rev.* 136 (3B Nov. 1964), B864–B871. DOI: `10.1103/PhysRev.136.B864`. URL: `https://link.aps.org/doi/10.1103/PhysRev.136.B864` (cit. on p. 37).

[61] W. Kohn and L. J. Sham. “Self-Consistent Equations Including Exchange and Correlation Effects”. In: *Phys. Rev.* 140 (4A Nov. 1965), A1133–A1138. DOI: `10.1103/PhysRev.140.A1133`. URL: `https://link.aps.org/doi/10.1103/PhysRev.140.A1133` (cit. on pp. 38, 40).

[62] Carlos Fiolhais, Fernando Nogueira, and Miguel AL Marques. *A primer in density functional theory*. Vol. 620. Springer Science & Business Media, 2003 (cit. on p. 39).

[63] David M Ceperley and Berni J Alder. “Ground state of the electron gas by a stochastic method”. In: *Physical review letters* 45.7 (1980), p. 566 (cit. on p. 40).

[64] Gianluca Stefanucci and Robert Van Leeuwen. *Nonequilibrium many-body theory of quantum systems: a modern introduction*. Cambridge University Press, 2013 (cit. on pp. 43, 136).

[65] Giancarlo Strinati. “Application of the Green’s functions method to the study of the optical properties of semiconductors”. In: *La Rivista del Nuovo Cimento (1978-1999)* 11.12 (1988), pp. 1–86 (cit. on pp. 43, 45, 47, 136, 140, 143).

[66] Feliciano Giustino. “Electron-phonon interactions from first principles”. In: *Rev. Mod. Phys.* 89 (1 Feb. 2017), p. 015003. DOI: `10.1103/RevModPhys.89.015003`. URL: `https://link.aps.org/doi/10.1103/RevModPhys.89.015003` (cit. on pp. 43, 65, 70, 95).

[67] Julien Toulouse. *Introduction to many-body Green-function theory*. URL: `https://www.lct.jussieu.fr/pagesperso/toulouse/enseignement/introduction_green.pdf` (cit. on p. 43).

[68] Alexander L Fetter and John Dirk Walecka. *Quantum theory of many-particle systems*. Courier Corporation, 2012 (cit. on p. 44).

[69] LD Landau. “Oscillations in a Fermi liquid”. In: *Soviet Physics Jetp-Ussr* 5.1 (1957), pp. 101–108 (cit. on p. 53).

[70] Matteo Guzzo, Giovanna Lani, Francesco Sottile, Pina Romaniello, Matteo Gatti, Joshua J. Kas, John J. Rehr, Mathieu G. Silly, Fausto Sirotti, and Lucia Reining. “Valence Electron Photoemission Spectrum of Semiconductors: Ab Initio Description of Multiple Satellites”. In: *Phys. Rev. Lett.* 107 (16 Oct. 2011), p. 166401. DOI: `10.1103/PhysRevLett.107.166401`. URL: `https://link.aps.org/doi/10.1103/PhysRevLett.107.166401` (cit. on p. 53).

[71] Maxim Shishkin, Martijn Marsman, and Georg Kresse. “Accurate quasiparticle spectra from self-consistent GW calculations with vertex corrections”. In: *Physical review letters* 99.24 (2007), p. 246403 (cit. on p. 54).

[72] Lyudmyla Adamska and Paolo Umari. “Bethe-Salpeter equation approach with electron-phonon coupling for exciton binding energies”. In: *Physical Review B* 103.7 (2021), p. 075201 (cit. on p. 57).

[73] Matteo Gatti and Francesco Sottile. “Exciton dispersion from first principles”. In: *Physical Review B* 88.15 (2013), p. 155113 (cit. on p. 57).

[74] Myrta Gruning, Andrea Marini, and Xavier Gonze. “Exciton-plasmon states in nanoscale materials: breakdown of the Tamm- Dancoff approximation”. In: *Nano letters* 9.8 (2009), pp. 2820–2824 (cit. on p. 58).

[75] Giovanni Bussi. “Effects of the electron–hole interaction on the optical properties of materials: the bethe–salpeter equation”. In: *Physica Scripta* 2004.T109 (2004), p. 141 (cit. on pp. 60, 61).

[76] W Van Roosbroeck and William Shockley. “Photon-radiative recombination of electrons and holes in germanium”. In: *Physical Review* 94.6 (1954), p. 1558 (cit. on p. 64).

[77] Fulvio Paleari. “First-principles approaches to the description of indirect absorption and luminescence spectroscopy: exciton-phonon coupling in hexagonal boron nitride”. PhD thesis. University of Luxembourg, Luxembourg, 2019 (cit. on pp. 64, 66, 82, 89).

[78] Wilfried Schäfer and Martin Wegener. *Semiconductor optics and transport phenomena*. Springer Science & Business Media, 2002 (cit. on p. 64).

[79] Neil W Ashcroft and N David Mermin. *Solid state physics*. Cengage Learning, 2022 (cit. on p. 66).

[80] Henrique Pereira Coutada Miranda. “Ab initio Approaches to Resonant Raman Spectroscopy of Transition Metal Dichalcogenides”. PhD thesis. University of Luxembourg, Luxembourg, Luxembourg, 2017 (cit. on p. 66).

[81] Peter Brüesch. *Phonons: Theory and experiments I: Lattice dynamics and Models of interatomic forces*. Vol. 34. Springer Science & Business Media, 2012 (cit. on p. 67).

[82] Xavier Gonze and Changyol Lee. “Dynamical matrices, Born effective charges, dielectric permittivity tensors, and interatomic force constants from density-functional perturbation theory”. In: *Physical Review B* 55.16 (1997), p. 10355 (cit. on p. 68).

[83] RM Sternheimer. “Electronic polarizabilities of ions from the Hartree-Fock wave functions”. In: *Physical Review* 96.4 (1954), p. 951 (cit. on p. 68).

[84] Hiroki Kawai, Koichi Yamashita, Elena Cannuccia, and Andrea Marini. “Electron-electron and electron-phonon correlation effects on the finite-temperature electronic and optical properties of zinc-blende GaN”. In: *Physical Review B* 89.8 (2014), p. 085202 (cit. on p. 70).

[85] Elena Cannuccia and Andrea Marini. “Effect of the quantum zero-point atomic motion on the optical and electronic properties of diamond and trans-polyacetylene”. In: *Physical review letters* 107.25 (2011), p. 255501 (cit. on p. 70).

[86] Pierre Lechifflart, Fulvio Paleari, and Claudio Attaccalite. “Excitons under strain: Light absorption and emission in strained hexagonal boron nitride”. In: *SciPost Physics* 12.5 (2022), p. 145 (cit. on pp. 72, 91, 107, 110).

[87] Yutaka Hoshina, Kojiro Iwasaki, Akira Yamada, and Makoto Konagai. “First-principles analysis of indirect-to-direct band gap transition of Ge under tensile strain”. In: *Japanese Journal of Applied Physics* 48.4S (2009), p. 04C125 (cit. on p. 72).

[88] T-H Cheng, K-L Peng, C-Y Ko, C-Y Chen, H-S Lan, Y-R Wu, CW Liu, and H-H Tseng. “Strain-enhanced photoluminescence from Ge direct transition”. In: *Applied Physics Letters* 96.21 (2010) (cit. on p. 72).

[89] Sujay B Desai, Gyungseon Seol, Jeong Seuk Kang, Hui Fang, Corsin Battaglia, Rehan Kapadia, Joel W Ager, Jing Guo, and Ali Javey. “Strain-induced indirect to direct bandgap transition in multilayer WSe2”. In: *Nano letters* 14.8 (2014), pp. 4592–4597 (cit. on p. 72).

[90] Meenakshi Choudhary, Shilpi Shital, Assaf Ya’Akobovitz, and Avi Niv. “Shear strain bandgap tuning of monolayer MoS2”. In: *Applied Physics Letters* 117.22 (2020) (cit. on p. 72).

[91] Riccardo Frisenda, Matthias Drüppel, Robert Schmidt, Steffen Michaelis de Vasconcellos, David Perez de Lara, Rudolf Bratschitsch, Michael Rohlfing, and Andres Castellanos-Gomez. “Biaxial strain tuning of the optical properties of single-layer transition metal dichalcogenides”. In: *npj 2D Materials and Applications* 1.1 (2017), p. 10 (cit. on p. 72).

[92] Ch Androulidakis, EN Koukaras, M Poss, K Papagelis, C Galiotis, and S Tawfick. “Strained hexagonal boron nitride: Phonon shift and Grüneisen parameter”. In: *Physical Review B* 97.24 (2018), p. 241414 (cit. on pp. 72, 75).

[93] Wei Yang, Yu Yang, Fawei Zheng, and Ping Zhang. “The distorted K1 soft mode of hexagonal-BN sheet and effects of charge doping”. In: *Applied Physics Letters* 103.18 (2013) (cit. on p. 72).

[94] Yoshitaka Fujimoto and Susumu Saito. “Band engineering and relative stabilities of hexagonal boron nitride bilayers under biaxial strain”. In: *Physical Review B* 94.24 (2016), p. 245427 (cit. on p. 72).

[95] FT Tabesh, Q Hassanzada, M Hadian, A Hashemi, I Abdolhosseini Sarsari, and M Abdi. “Strain induced coupling and quantum information processing with hexagonal boron nitride quantum emitters”. In: *Quantum Science and Technology* 7.1 (2021), p. 015002 (cit. on p. 72).

[96] Léonard Schue. “Propriétés optiques et structurales du nitrure de bore en hybridation sp^2: des cristaux massifs aux feuillets atomiques”. PhD thesis. Université Paris Saclay (COmUE), 2017 (cit. on pp. 72, 84).

[97] Elena Blundo, Alessandro Surrente, Davide Spirito, Giorgio Pettinari, Tanju Yildirim, Carlos Alvarado Chavarin, Leonetta Baldassarre, Marco Felici, and Antonio Polimeni. “Vibrational properties in highly strained hexagonal boron nitride bubbles”. In: *Nano letters* 22.4 (2022), pp. 1525–1533 (cit. on pp. 75, 86).

[98] Joongoo Kang, Lijun Zhang, and Su-Huai Wei. “A Unified Understanding of the Thickness-Dependent Bandgap Transition in Hexagonal Two-Dimensional Semiconductors”. In: *The Journal of Physical Chemistry Letters* 7.4 (2016). PMID: 26800573, pp. 597–602. DOI: `10.1021/acs.jpclett.5b02687`. eprint: `https://doi.org/10.1021/acs.jpclett.5b02687`. URL: `https://doi.org/10.1021/acs.jpclett.5b02687` (cit. on pp. 77, 78).

[99] Fulvio Paleari, Thomas Galvani, Hakim Amara, François Ducastelle, Alejandro Molina-Sánchez, and Ludger Wirtz. “Excitons in few-layer hexagonal boron nitride: Davydov splitting and surface localization”. In: *2D Materials* 5.4 (2018), p. 045017 (cit. on pp. 78, 87, 107, 110, 141).

[100] Claudio Attaccalite, Myrta Grüning, Hakim Amara, Sylvain Latil, and François Ducastelle. “Two-photon absorption in two-dimensional materials: The case of hexagonal boron nitride”. In: *Physical Review B* 98.16 (2018), p. 165126 (cit. on pp. 78, 141).

[101] Felix Carrascoso, Hao Li, Riccardo Frisenda, and Andres Castellanos-Gomez. “Strain engineering in single-, bi-and tri-layer MoS 2, MoSe 2, WS 2 and WSe 2”. In: *Nano Research* 14 (2021), pp. 1698–1703 (cit. on p. 78).

[102] Marios Zacharias, Christopher E Patrick, and Feliciano Giustino. “Stochastic approach to phonon-assisted optical absorption”. In: *Physical review letters* 115.17 (2015), p. 177401 (cit. on p. 81).

[103] Jonathan H Lloyd-Williams and Bartomeu Monserrat. “Lattice dynamics and electron-phonon coupling calculations using nondiagonal supercells”. In: *Physical Review B* 92.18 (2015), p. 184301 (cit. on p. 82).

[104] Marios Zacharias and Feliciano Giustino. “Theory of the special displacement method for electronic structure calculations at finite temperature”. In: *Physical Review Research* 2.1 (2020), p. 013357 (cit. on p. 82).

[105] Andrea Marini. “Ab initio finite-temperature excitons”. In: *Physical Review Letters* 101.10 (2008), p. 106405 (cit. on p. 83).

[106] TQP Vuong, Guillaume Cassabois, Pierre Valvin, Song Liu, JH Edgar, and Bernard Gil. “Exciton-phonon interaction in the strong-coupling regime in hexagonal boron nitride”. In: *Physical Review B* 95.20 (2017), p. 201202 (cit. on pp. 84, 106).

[107] Carina Faber, Paul Boulanger, Claudio Attaccalite, Elena Cannuccia, Ivan Duchemin, Thierry Deutsch, and Xavier Blase. “Exploring approximations to the G W self-energy ionic gradients”. In: *Physical Review B* 91.15 (2015), p. 155109 (cit. on p. 84).

[108] Francesco Libbi, Pedro Miguel MC de Melo, Zeila Zanolli, Matthieu Jean Verstraete, and Nicola Marzari. “Phonon-assisted luminescence in defect centers from many-body perturbation theory”. In: *Physical Review Letters* 128.16 (2022), p. 167401 (cit. on pp. 86, 98).

[109] Pierre Lechifflart, Fulvio Paleari, Davide Sangalli, and Claudio Attaccalite. “First-principles study of luminescence in hexagonal boron nitride single layer: Exciton-phonon coupling and the role of substrate”. In: *Physical Review Materials* 7.2 (2023), p. 024006 (cit. on p. 87).

[110] Andrea Splendiani, Liang Sun, Yuanbo Zhang, Tianshu Li, Jonghwan Kim, Chi-Yung Chim, Giulia Galli, and Feng Wang. "Emerging photoluminescence in monolayer MoS2". In: *Nano Letters* 10.4 (2010), pp. 1271–1275 (cit. on p. 87).

[111] Kin Fai Mak, Changgu Lee, James Hone, Jie Shan, and Tony F. Heinz. "Atomically Thin MoS_2: A New Direct-Gap Semiconductor". In: *Phys. Rev. Lett.* 105 (13 Sept. 2010), p. 136805. DOI: `10.1103/PhysRevLett.105.136805`. URL: `https://link.aps.org/doi/10.1103/PhysRevLett.105.136805` (cit. on p. 87).

[112] Long Yuan and Libai Huang. "Exciton dynamics and annihilation in WS 2 2D semiconductors". In: *Nanoscale* 7.16 (2015), pp. 7402–7408 (cit. on p. 87).

[113] Alexandre Plaud, Léonard Schué, Kenji Watanabe, Takashi Taniguchi, F Fossard, F Ducastelle, A Loiseau, and J Barjon. "Exciton-exciton annihilation in hBN". In: *Applied Physics Letters* 114.23 (2019), p. 232103 (cit. on p. 87).

[114] Thomas Galvani, Fulvio Paleari, Henrique PC Miranda, Alejandro Molina-Sánchez, Ludger Wirtz, Sylvain Latil, Hakim Amara, and François Ducastelle. "Excitons in boron nitride single layer". In: *Physical Review B* 94.12 (2016), p. 125303 (cit. on pp. 88, 100, 141).

[115] Maria Stella Prete, Davide Grassano, Olivia Pulci, Ihor Kupchak, Valerio Olevano, and Friedhelm Bechstedt. "Giant excitonic absorption and emission in two-dimensional group-III nitrides". In: *Scientific reports* 10.1 (2020), pp. 1–9 (cit. on pp. 88, 100).

[116] KA Mengle and E Kioupakis. "Impact of the stacking sequence on the bandgap and luminescence properties of bulk, bilayer, and monolayer hexagonal boron nitride". In: *APL Materials* 7.2 (2019), p. 021106 (cit. on p. 88).

[117] Sylvain Latil, Hakim Amara, and Lorenzo Sponza. "Electronic properties of the five principal stackings of boron nitride moir\'e bilayers". In: *arXiv preprint arXiv:2206.05845* (June 2022). arXiv: `2206.05845 [cond-mat.mtrl-sci]` (cit. on p. 88).

[118] Hsiao-Yi Chen, Davide Sangalli, and Marco Bernardi. "Exciton-phonon interaction and relaxation times from first principles". In: *Physical Review Letters* 125.10 (2020), p. 107401 (cit. on pp. 88, 89, 106, 107).

[119] Vasili Perebeinos and Phaedon Avouris. "Phonon and electronic nonradiative decay mechanisms of excitons in carbon nanotubes". In: *Physical review letters* 101.5 (2008), p. 057401 (cit. on pp. 89, 95).

[120] Manuel Katzer, Malte Selig, Lukas Sigl, Mirco Troue, Johannes Figueiredo, Jonas Kiemle, Florian Sigger, Ursula Wurstbauer, Alexander W. Holleitner, and Andreas Knorr. *Exciton-phonon-scattering: A competition between bosonic and fermionic nature of bound electron-hole pairs*. 2023. arXiv: `2303.11787 [cond-mat.mes-hall]` (cit. on pp. 94, 120).

[121] Gerald D Mahan. *Many-particle physics*. Springer Science & Business Media, 2000 (cit. on pp. 95, 96).

[122] Andrea Marini and Rodolfo Del Sole. “Dynamical excitonic effects in metals and semiconductors”. In: *Physical review letters* 91.17 (2003), p. 176402 (cit. on p. 96).

[123] Pedro Miguel MC de Melo and Andrea Marini. “Unified theory of quantized electrons, phonons, and photons out of equilibrium: A simplified ab initio approach based on the generalized Baym-Kadanoff ansatz”. In: *Physical Review B* 93.15 (2016), p. 155102 (cit. on p. 98).

[124] Mark van Schilfgaarde, Takao Kotani, and Sergey Faleev. “Quasiparticle self-consistent g w theory”. In: *Physical review letters* 96.22 (2006), p. 226402 (cit. on p. 100).

[125] Carina Faber, Paul Boulanger, Claudio Attaccalite, Ivan Duchemin, and Xavier Blase. “Excited states properties of organic molecules: From density functional theory to the GW and Bethe–Salpeter Green’s function formalisms”. In: *Philosophical Transactions of the Royal Society A: Mathematical, Physical and Engineering Sciences* 372.2011 (2014), p. 20130271 (cit. on p. 100).

[126] X Blase, Angel Rubio, Steven G Louie, and Marvin L Cohen. “Stability and band gap constancy of boron nitride nanotubes”. In: *EPL (Europhysics Letters)* 28.5 (1994), p. 335 (cit. on p. 101).

[127] X. Blase, Angel Rubio, Steven G. Louie, and Marvin L. Cohen. “Quasiparticle band structure of bulk hexagonal boron nitride and related systems”. In: *Phys. Rev. B* 51 (11 Mar. 1995), pp. 6868–6875. DOI: `10.1103/PhysRevB.51.6868`. URL: `https://link.aps.org/doi/10.1103/PhysRevB.51.6868` (cit. on p. 101).

[128] Pierluigi Cudazzo, Lorenzo Sponza, Christine Giorgetti, Lucia Reining, Francesco Sottile, and Matteo Gatti. “Exciton band structure in two-dimensional materials”. In: *Physical review letters* 116.6 (2016), p. 066803 (cit. on p. 101).

[129] Jaakko Koskelo, Giorgia Fugallo, Mikko Hakala, Matteo Gatti, Francesco Sottile, and Pierluigi Cudazzo. “Excitons in van der Waals materials: from monolayer to bulk hexagonal boron nitride”. In: *Physical Review B* 95.3 (2017), p. 035125 (cit. on p. 101).

[130] Matteo Zanfrognini, Alexandre Plaud, Ingrid Stenger, Frédéric Fossard, Lorenzo Sponza, Léonard Schué, Fulvio Paleari, Elisa Molinari, Daniele Varsano, Ludger Wirtz, et al. “Distinguishing different stackings in layered materials via luminescence spectroscopy”. In: *arXiv preprint arXiv:2305.17554* (2023) (cit. on pp. 105, 107, 108, 119).

[131] Feliciano Giustino, Marvin L Cohen, and Steven G Louie. “Electron-phonon interaction using Wannier functions”. In: *Physical Review B* 76.16 (2007), p. 165108 (cit. on p. 107).

[132] JCG Henriques, GB Ventura, CDM Fernandes, and NMR Peres. “Optical absorption of single-layer hexagonal boron nitride in the ultraviolet”. In: *Journal of Physics: Condensed Matter* 32.2 (2019), p. 025304 (cit. on p. 109).

[133] Claudio Attaccalite, Michel Bockstedte, Andrea Marini, Angel Rubio, and Ludger Wirtz. “Coupling of excitons and defect states in boron-nitride nanostructures”. In: *Physical Review B* 83.14 (2011), p. 144115 (cit. on p. 110).

[134] Maja Feierabend, Gunnar Berghäuser, Andreas Knorr, and Ermin Malic. “Proposal for dark exciton based chemical sensors”. In: *Nature communications* 8.1 (2017), p. 14776 (cit. on p. 110).

[135] Alberto Guandalini, Pino D’Amico, Andrea Ferretti, and Daniele Varsano. “Efficient GW calculations in two dimensional materials through a stochastic integration of the screened potential”. In: *npj Computational Materials* 9.1 (2023), p. 44 (cit. on p. 112).

[136] Miguel M Ugeda, Aaron J Bradley, Su-Fei Shi, Felipe H Da Jornada, Yi Zhang, Diana Y Qiu, Wei Ruan, Sung-Kwan Mo, Zahid Hussain, Zhi-Xun Shen, et al. “Giant bandgap renormalization and excitonic effects in a monolayer transition metal dichalcogenide semiconductor”. In: *Nature materials* 13.12 (2014), pp. 1091–1095 (cit. on p. 112).

[137] Aaron J Bradley, Miguel M. Ugeda, Felipe H da Jornada, Diana Y Qiu, Wei Ruan, Yi Zhang, Sebastian Wickenburg, Alexander Riss, Jiong Lu, Sung-Kwan Mo, et al. “Probing the role of interlayer coupling and coulomb interactions on electronic structure in few-layer MoSe2 nanostructures”. In: *Nano letters* 15.4 (2015), pp. 2594–2599 (cit. on p. 112).

[138] Thibault Sohier, Marco Gibertini, and Matthieu J Verstraete. “Remote free-carrier screening to boost the mobility of Fröhlich-limited two-dimensional semiconductors”. In: *Physical Review Materials* 5.2 (2021), p. 024004 (cit. on p. 113).

[139] Pierluigi Cudazzo. “Dynamical effects on photoluminescence spectra from first principles: A many-body Green’s function approach”. In: *Physical Review B* 108.16 (2023), p. 165101 (cit. on p. 117).

[140] Galit Cohen, Jonah B Haber, Jeffrey B Neaton, Diana Y Qiu, and Sivan Refaely-Abramson. “Phonon-driven femtosecond dynamics of excitons in crystalline pentacene from first principles”. In: *arXiv preprint arXiv:2305.04223* (2023) (cit. on p. 120).

[141] Fabien Bruneval and Xavier Gonze. “Accurate G W self-energies in a plane-wave basis using only a few empty states: Towards large systems”. In: *Physical Review B* 78.8 (2008), p. 085125 (cit. on pp. 140, 143).

[142] M J van Setten, Matteo Giantomassi, Eric Bousquet, Matthieu J Verstraete, Don R Hamann, Xavier Gonze, and G-M Rignanese. “The PseudoDojo: Training and grading a 85 element optimized norm-conserving pseudopotential table”. In: *Computer Physics Communications* 226 (2018), pp. 39–54 (cit. on p. 143).

[143] N. Troullier and José Luis Martins. “Efficient pseudopotentials for plane-wave calculations”. In: *Phys. Rev. B* 43 (3 Jan. 1991), pp. 1993–2006. DOI: `10.1103/PhysRevB.43.1993`. URL: `https://link.aps.org/doi/10.1103/PhysRevB.43.1993` (cit. on p. 143).

[144] Thibault Sohier, Matteo Calandra, and Francesco Mauri. “Density functional perturbation theory for gated two-dimensional heterostructures: Theoretical developments and application to flexural phonons in graphene”. In: *Physical Review B* 96.7 (2017), p. 075448 (cit. on p. 143).

[145] Thibault Sohier, Matteo Calandra, and Francesco Mauri. “Two-dimensional Fröhlich interaction in transition-metal dichalcogenide monolayers: Theoretical modeling and first-principles calculations”. In: *Physical Review B* 94.8 (2016), p. 085415 (cit. on p. 143).

[146] Warren E Pickett, Henry Krakauer, and Philip B Allen. “Smooth fourier interpolation of periodic functions”. In: *Physical Review B* 38.4 (1988), p. 2721 (cit. on p. 144).

[147] David Kammerlander, Silvana Botti, Miguel AL Marques, Andrea Marini, and Claudio Attaccalite. “Speeding up the solution of the Bethe-Salpeter equation by a double-grid method and Wannier interpolation”. In: *Physical Review B* 86.12 (2012), p. 125203 (cit. on p. 144).

Appendices

A. Derivation of equations of motion for field operators

Here we derive the equations of motion for the field operators in Heisenberg picture, based on [38, 64, 65, 37]. In the main text however, the interaction picture is used. The following derivation is left unchanged if one considers the unperturbed Hamiltonian to be the time-independent $\hat{H}$ and any other time-dependent external perturbation, which is exactly what was done in the main text. We shall make explicit the time dependence of every term appearing in the Green's function in Eq. (2.27). We start with the time evolution of the field operators. We recall some useful properties of the field operators for fermions in the Schrödinger picture :

$$\begin{aligned}\{\hat{\psi}(x),\hat{\psi}^\dagger(x')\} &= \delta(x-x')\\ \{\hat{\psi}(x),\hat{\psi}(x')\} &= \{\hat{\psi}^\dagger(x),\hat{\psi}^\dagger(x')\} = 0\\ n(x) &= \hat{\psi}^\dagger(x)\hat{\psi}(x)\end{aligned} \tag{A.1}$$

The total Hamiltonian enters the Heisenberg equation of motion for an operator $\hat{O}$:

$$i\frac{d}{dt}\hat{O}_H(t) = \hat{U}_S^\dagger(t)\left[\hat{O}(t),\hat{H}\right]\hat{U}_S(t) + \hat{U}_S^\dagger(t)(i\frac{d}{dt}\hat{O}_S(t))\hat{U}_S(t) \tag{A.2}$$

where the subscript H and S denote respectively the Heisenberg and Schrödinger pictures, and the transformation from the latter to the former is given by :

$$\begin{aligned}\hat{\psi}_H(x,t) &= \hat{U}_S^\dagger(t)\hat{\psi}_S(x)\hat{U}_S(t)\\ \hat{\psi}_H^\dagger(x,t) &= \hat{U}_S^\dagger(t)\hat{\psi}_S^\dagger(x)\hat{U}_S(t)\end{aligned} \tag{A.3}$$

and $\hat{U}_S(t) = \exp\left(-i\hat{H}t\right)$ is the time evolution operator. In the following we drop the subscript H for the field operators, as their time dependence will be explicit. The Heisenberg equation of motion for the field operator is then :

$$i\frac{d}{dt}\hat{\psi}(x,t) = \hat{U}_S^\dagger(t)\left[\hat{\psi}(x),\hat{H}\right]\hat{U}_S(t) \tag{A.4}$$

and similarly for $\hat{\psi}^\dagger$. To compute the commutator, we split the two terms of the Hamiltonian and we use the identity

$$\left[\hat{\psi}(x),\hat{A}\hat{B}\right] = \{\hat{\psi}(x),\hat{A}\}\hat{B} - \hat{A}\{\hat{\psi}(x),\hat{B}\} \tag{A.5}$$

where we take

$$\begin{aligned} \hat{A} &= \hat{\psi}^{\dagger}(x_1) \\ \hat{B} &= h(x_1)\hat{\psi}(x_1) \end{aligned} \tag{A.6}$$

Since $\{\hat{\psi}(x), \hat{B}\} = 0$, then

$$\left[\hat{\psi}(x), \hat{H}_0\right] = h(x)\hat{\psi}(x) \tag{A.7}$$

Now we notice that the second term in the commutator contains

$$\begin{aligned} \left[\hat{\psi}(x), \hat{\psi}^{\dagger}(x_1)\hat{\psi}^{\dagger}(x_2)\hat{\psi}(x_2)\hat{\psi}(x_1)\right] &= \left[\hat{\psi}(x), \hat{\psi}^{\dagger}(x_1)\hat{\psi}^{\dagger}(x_2)\right]\hat{\psi}(x_2)\hat{\psi}(x_1) \\ &= \left(\hat{\psi}^{\dagger}(x_1)\delta(x_1 - x_2) + \hat{\psi}^{\dagger}(x_2)\delta(x - x_1)\right)\hat{\psi}(x_2)\hat{\psi}(x_1). \end{aligned} \tag{A.8}$$

Therefore,

$$\begin{aligned} \left[\hat{\psi}(x), \hat{H}_{int}\right] &= \frac{1}{2}\int dx_1 \hat{\psi}^{\dagger}(x_1)\hat{\psi}(x)\hat{\psi}(x_1)v(x, x_1) + \frac{1}{2}\int dx_2 \hat{\psi}^{\dagger}(x_2)\hat{\psi}(x_2)\hat{\psi}(x)v(x, x_2) \\ &= \int dx_2 v(x, x_2)\hat{\psi}^{\dagger}(x_1)\hat{\psi}(x_2)\hat{\psi}(x) \end{aligned} \tag{A.9}$$

where in the second line we used the symmetry property of the Coulomb interaction $v(x, x') = v(x', x)$. Finally, with the compact notation $1 \equiv (\mathbf{r}_1, \sigma, t_1)$, we get the equations of motion for the field operators :

$$\begin{aligned} \frac{\partial}{\partial t_1}\hat{\psi}(1) &= -i\left[h(1) + \int d3 v(1,3)\hat{\psi}^{\dagger}(3)\hat{\psi}(3)\right]\hat{\psi}(1) \\ \frac{\partial}{\partial t_2}\hat{\psi}^{\dagger}(2) &= i\left[h(2)\hat{\psi}^{\dagger}(2) + \hat{\psi}^{\dagger}(2)\int d3 v(2,3)\hat{\psi}^{\dagger}(3)\hat{\psi}(3)\right] \end{aligned} \tag{A.10}$$

B. From orthorombic strained cell to pseudo-hexagonal unit cell

In our case we a have a crystal with a two-atom basis. We simulate uni-axial strain by elongating or shortening the bond length in only one cartesian direction and letting the atoms relax along the other two orthogonal directions. It is straightforward to impose such a constraint to a lattice with orthogonal vectors, but more complicated if we had kept the equilibrium hexagonal unit cell. This is why we chose to do the relaxation of structures under strain with orthorombic cells containing 8 atoms (4 per plan). We want to build a unit cell that preserves the symmetry and periodicity of the strained crystal, with as few atoms as possible. The following is a geometrical generalization of the transformation from orthorombic to hexagonal lattice unit cell in cartesian coordinates.
Take an orthorombic unit cell whose matrix in cartesian coordinates is :

$$\begin{pmatrix} a & 0 & 0 \\ 0 & b & 0 \\ 0 & 0 & c \end{pmatrix} \tag{B.1}$$

with a, b, c being arbitrary lengths. Now we want to build a strained unit cell that resembles the equilibrium hexagonal cell the most, so that we can compare the different Brillouin zones and the paths on which we plot the electronic structure and the phonon dispersion. The rhombus representing the unit cell of the pseudo-hexagonal cell, viewed from the top, is drawn in Fig. B.1. Then we have :

$$a' = \sqrt{d^2 + p^2} \tag{B.2}$$

$$\beta = \pi - 2\tan^{-1}\left(\frac{p}{d}\right) \tag{B.3}$$

where d, p are the half diagonals of the rhombus, a' is the side length and β the angle as shown in Fig B.1. This is a regular rhombus in the sense that all sides have equal length and the diagonals are orthogonal. The length of the diagonals is obtained from the knowledge of the orthorombic cell, as shown in Fig. 3.2 in the main text. Then the

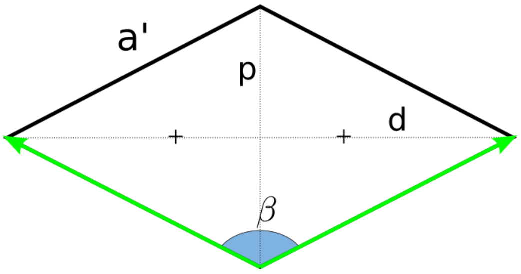

Figure B.1. – Rhombus used as the unit cell for the pseudo-hexagonal lattice with the atom positions indicated with crosses, viewed from top.

matrix of this rhombus unit cell, expressed in cartesian coordinates, is :

$$\begin{pmatrix} a' & 0 & 0 \\ a'\cos\beta & a'\sin\beta & 0 \\ 0 & 0 & c \end{pmatrix} \tag{B.4}$$

The first two lines are the vectors in green in Fig. B.1. The third vector c is the one perpendicular to the atomic planes and is the same than the orthorombic c. In the equilibrium case, we have $\beta = 120°$, then this matrix reduces to :

$$\begin{pmatrix} a' & 0 & 0 \\ -a'/2 & a'\sqrt{3}/2 & 0 \\ 0 & 0 & c \end{pmatrix} \tag{B.5}$$

which is the standard hexagonal-lattice unit cell. We now have built a 2-atom unit cell which we used to compute electronic, phononic and optical properties of our strained materials. We checked that both the orthorombic and the pseudo-hexagonal unit cells form the same strained crystal when periodically repeated in all directions.

C. Computational parameters for Chapter 2

We applied different strains along the x-direction, the one parallel to the B-N bond, ranging from -2.5% to $+2.5\%$ of the equilibrium cell vector. Then we allowed the cell vectors and atomic positions to relax only in the other two orthogonal directions, keeping the arbitrarily strained length fixed. The relaxation is done using Density Functional Theory and a damped molecular dynamics algorithm as implemented in the QuantumEspresso code,[56] with norm-conserving pseudo-potentials in the Local Density Approximation (LDA), a kinetic energy cutoff of 120 Ry and an equivalent Monkhorst-Pack grid of $18 \times 18 \times 6$ k-points. The forces acting on the cell and atoms were converged to be lower than 10^{-6} a.u.

Once the strained orthorhombic cells were relaxed, we have constructed strained pseudo-hexagonal cells in order to proceed with the electronic and optical calculations.

On these pseudo-hexagonal 2-atom cells we performed phonon calculations using DFPT,[56] with $\mathbf{q}$-points and $\mathbf{k}$-sampling respectively of $6 \times 6 \times 2$ and $18 \times 18 \times 6$, in order to verify the stability of our structure and the effect of strain on phonon modes.

The quasi-particle band structure was obtained within the $\mathrm{G_0W_0}$ approximation, using again a $18 \times 18 \times 6$ k-points sampling, with 210 bands plus a terminator[141] for G and W in order to speed up convergence. We used a cutoff of 7 Ha for the dielectric constant that was calculated within the plasmon-pole approximation. Excitons and optical absorption were studied solving the Bethe-Salpeter equation[65] using 4 valence and 4 conduction bands, as implemented in the `yambo`code,[58] using the same k-points grid as for the $\mathrm{G_0W_0}$ calculations.

Luminescence was calculated following the approach described in Ref. [29]. We searched for the minima of the indirect gap within the independent particle approximation and we used the corresponding $\mathbf{q}$-vectors to construct a supercell that map these points at Γ. We displaced atoms along all possible phonon modes having a periodicity commensurate with the different $\mathbf{q}$-points of the indirect gap minima, and calculated the derivatives of the excitonic optical matrix elements. [1] With these ingredients plus the phonon frequencies we reconstructed the spectra using the van Roosbroeck–Shockley relation.[29]

---

[1] In the luminescence calculations we used a smaller k-point sampling, $12 \times 12 \times 4$ and a scissor operator to speed up calculations in the supercells, similar to Refs. [28, 29]. These parameters are sufficient to describe the lowest exciton that is responsible for the luminescence.

D. Analysis of first excitons in bulk hBN

In bulk hBN due to the strong exciton localization the three fold symmetry cannot be disregarded and this makes the usual hydrogenic model inadequate to describe exciton series.[100] Therefore we analyze the nature of the first excitons in bulk hBN using the solution of the full Bethe-Salpeter equation. Our analysis is based on direct comparison of exciton wave-functions with the results of Refs. [99, 114, 100]. By means of this comparison we were able to recognize different excitonic states. However for a deeper analysis a tight-binding model and the plot of exciton phase is necessary [114] that is beyond the scope of this thesis. In Table D.1 we report the first 13 excitonic states. For each state we report its binding energy both in self-consistent evGW and G_0W_0 approximation, its symmetry, and the inter-layer (IL) or in-plane pair (IP) character, using the same notation than Ref. [114]. All these excitons are formed by $\pi \rightarrow \pi^*$ transition, that correspond to an hopping from nitrogen atom to the boron. For this reason the excitonic wave-function in Table D.1 are obtained by fixing the position of the hole slightly above a nitrogen atom. Similarly to the bi-layer case,[114] in bulk hBN excitons undergo a Davydov splitting in even and odd states with respect to the inversion symmetry. The parity with respect to the inversion symmetry is important for optical properties because transitions are allowed only with odd parity states.[100] This parity cannot be inferred from the plot of electron density at fixed hole position as in the figures of Table D.1 but requires an analysis of the exciton wave-function phase. Therefore we assigned parity by looking at the dipole matrix elements. The first excitonic states from 1 to 4 correspond to the 1s exciton split in two degenerate pairs. Then we found a series of excitons similar to the monolayer case[99]: two with A_1 and A_2 symmetry, followed by a pair with E symmetry. At higher energy we have interlayer excitons and then the degenerate states 12,13 that are the fist pair responsible for the second peak in the absorption spectra. At higher energy identification is more difficult but we expect to find all the Davydov pair of the lowest excitons presented here.

Exciton Number	Binding Energy [eV]	Exciton wavefunction	Symmetry	Bright	Description
1,2	-0.998 (-0.755)	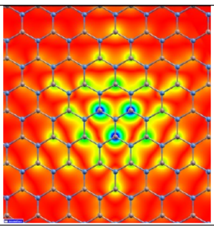	E_g	No	IP, 1s
3,4	-0.923 (-0.693)	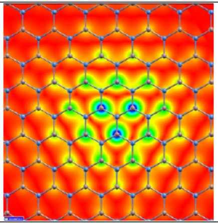	E_u	Yes	IP, 1s
5	-0.621 (-0.464)	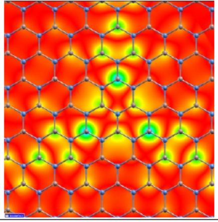	A_1	No	IP
6	-0.535 (-0.413)	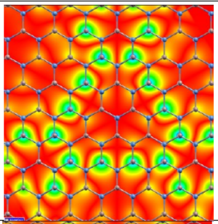	A_2	No	IP
7,8	-0.491 (-0.365)	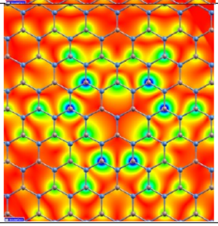	E_g	No	IP
9	-0.4417 (-0.330)			No	IL
10	-0.424 (-0.319)			No	IL
11	-0.403 (-0.303)			No	IP
12,13	-0.397 (-0.295)	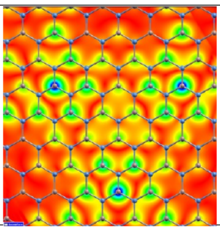	E_u	Yes	IP, 2p?

Figure D.1. – The first 13 excitons in bulk hBN. In this table we report both the binding energy in evGW and in G_0W_0 approximation.

E. Computational details for Chapter 3

In this section we present our computational workflow for the calculation of the exciton-phonon coupling and all the computational details needed to reproduce the results. A sketch of the workflow is reported in Fig. 1.3. We start from the crystal structure, which was optimized within DFT for the monolayer and taken from Ref. [12] for bulk hBN. The relevant lattice parameters are shown in Table E.1. We performed all DFT calculations using the QUANTUM ESPRESSO code[56], with norm-conserving pseudopotentials[142] in the LDA.[143] In the monolayer case, a supercell was used with a length of 21 Å along the z-direction – in such a way to avoid spurious interactions between periodic images – along with the 2D cutoff for the Coulomb interaction implemented in Quantum Espresso.[144] Energy cutoff and other parameters that enter the DFT calculations are reported in Tab. E.1. Phonons and electron-phonon couplings were calculated within DFPT starting from the DFT results. The transferred momenta grid for the phonons is reported in Tab. E.1. The correct long-range behavior of the electron-phonon coupling in 2D was obtained by applying a cutoff of the Coulomb interaction in the z-direction.[145] The electron-phonon matrix elements were calculated on the same $\mathbf{q}$-grid as the phonons and the excitons, for all the electronic bands entering in the BSE kernel.

Using the Kohn-Sham band structure as a starting point, we employed MBPT as implemented in the `yambo` code[58] to calculate quasiparticle band structures within the G_0W_0 approximation[37] and the excitonic optical response functions using the BSE.[65] All the many-body operators that enter in these calculations are expanded in a Kohn-Sham basis set. Therefore, in order to have converged results, we diagonalized the Kohn-Sham Hamiltonian for a large number of bands that were then used to build the electronic Green's function G and the dielectric matrix ϵ. In table E.1 we also report the cutoff used in the construction of the dielectric matrix. Finally, in order to speed up convergence with respect to the empty states, we used a terminator for both ϵ and G.[141] The BSE was constructed using a static kernel derived from the GW self-energy within the Tamm-Dancoff approximation.[65] We include only the lowest conduction and the highest valence bands in such a way to get converged absorption and emission spectra. The BSE was solved for a grid of transferred momenta $\mathbf{Q}$ identical to the phonons grid.

Luminescence spectra were calculated using Eq. (4.33). We first built the exciton-phonon matrix elements using the results obtained from BSE and DFPT, as indicated in the scheme in Fig. 1.3. We selected a number of "initial" excitons at finite $\mathbf{Q}$ (indices β in Eq. (4.33)), that scatter with phonons (indices μ, $\mathbf{q}$) and end up in the "final" excitonic states at $\mathbf{Q} = 0$ (indices λ). All phonon modes and transferred momenta were included in these calculations. Note that both the electronic and transferred momenta (k-grid and q-grid, respectively), were computed on the irreducible parts of the respective Brillouin zones (BZs). The exciton-phonon coupling matrix elements $\mathcal{G}$ from Eq. (4.24) were then expanded in the full BZs by symmetry transformations applied to the electron-phonon matrix elements g and the excitonic coefficients A. In this way, we are able to significantly speed up exciton-phonon calculations, which would otherwise require the switching off

Parameter/System	m-hBN	hBN (and bBN)
q/**k**-grid	$36 \times 36 \times 1$	$18 \times 18 \times 6$
a	2.48 Å	2.50 Å
c	-	3.25 Å
GW/ $\varepsilon(\omega)$ bands	200	210
$\varepsilon(\omega)$ cutoff	10 Ha	8 Ha
BSE bands	3-6	5-12
Excitons ($\beta \to \lambda$)	$8 \to 2$	$12 \to 4$
Double grid	$108 \times 108 \times 1$	$54 \times 54 \times 18$

Table E.1. – List of the relevant computational parameters entering the calculation of excitons, phonons and their coupling (a is the planar lattice parameter and c the interlayer distance).

of all crystal symmetries at the DFPT and MBPT levels.

Then, we interpolated both exciton dispersions – using a smooth Fourier interpolation[146] – and phonon energies – using the force constants method implemented in Quantum ESPRESSO – on a finer grid to speed up convergence of the luminescence spectra with respect to the transferred momenta grid. Then these finer grids are used to average out the denominators appearing in the luminescence formula as:

$$\frac{1}{W^{\pm}_{\lambda,\beta,\mathbf{q},\mu}} = \frac{1}{N_{\tilde{q}}} \sum_{\tilde{q} \in \mathbf{q}} \frac{1/2 \pm 1/2 + n_{\tilde{q},\mu}}{\omega - (E_{\tilde{q},\beta} \mp \Omega_{\tilde{q}\mu}) + i\eta} e^{-\frac{E_{\tilde{q},\beta} - \tilde{E}_{min}}{kT_{exc}}} \tag{E.1}$$

where $\tilde{E}_{min}$ is the minimum exciton energy on the double-grid, than will likely be different from the one on the coarse grid. Using the average denominators implemented as a sum over the fine-grid $\tilde{q}$-points in the neighborhood of each coarse-grid q-point, we can rewrite the luminescence intensity formula Eq. (4.33) as :

$$\begin{aligned} I(\omega) = \mathcal{D}\,\mathrm{Im} \sum_{\lambda} |T^{\lambda}|^2 \Bigg\{ & \omega^3 n_1(\omega) \frac{1 - Z_{\lambda}}{\omega - E_{\lambda} + i\eta}\, e^{-\frac{E_{\lambda} - E_{min}}{k_B T_{exc}}} \\ & + \frac{1}{N_q} \sum_{\mu\beta\mathbf{q}} \omega(\omega \mp \Omega_{\mathbf{q}\mu})^2 n_1(\omega) \frac{|\mathcal{G}^{\mu}_{\beta\lambda}(\mathbf{q})|^2}{(E_{\mathbf{q}\beta} - E_{\lambda} \pm \Omega_{\mathbf{q}\mu})^2} \frac{1}{W^{\pm}_{\lambda,\beta,\mathbf{q},\mu}} \Bigg\}. \end{aligned} \tag{E.2}$$

The calculations of mBN on top of one and two Graphene layers have been performed using a 36×36× 1 grid, plus a shifted double-grid of 90×90×1 for the screened interaction W as described in Ref. [147] and the slab cutoff in the out-of-plane direction, 7 Ha cutoff for the dielectric constant, and conduction bands up to 120 eV.